Photo-Induced Phenomena from the Quantum Chemist Point of View

Tangui Le Bahers

MEMOIRE

En vue de l'obtention du diplôme national de l'

Habilitation à diriger des recherches, délivré par l'Université Claude Bernard Lyon 1

Discipline : Chimie

Laboratoire de Chimie de l'ENS Lyon

Présenté publiquement le 14 Juin 2018

Par Monsieur **Tangui LE BAHERS**

Photo-Induced Phenomena from the Quantum Chemist Point of View

---

Devant le jury composé de :

Dr. Valérie Keller	CNRS / Université de Strasbourg
Pr. Mario Barbatti	Université d'Aix-Marseille
Dr. Pascal Raybaud	IFP Energies Nouvelles
Dr. Filippo De Angelis	CNR Perugia / Italy
Pr. Christophe Morell	Université Claude Bernard Lyon 1
Dr. Chantal Andraud	CNRS / ENS Lyon

Remerciements

Voilà maintenant 7 ans que j'ai soutenu ma thèse. Ce manuscrit vient retracer les travaux scientifiques que j'ai réalisés depuis. Mais avant de rentrer dans le vif du sujet, je souhaiterais présenter mes plus chaleureux remerciements aux personnes qui ont contribué à mon début de carrière.

Je saisis cette occasion pour exprimer une fois encore ma reconnaissance la plus sincère à Ilaria Ciofini et Thierry Pauporté qui, par leur encadrement de thèse, ont proprement lancé ma carrière et ont apporté les premières bases du scientifique que je suis aujourd'hui.

Vient ensuite mon année de post-doc entre l'équipe dirigée par Thierry Le Mercier au RICP de Solvay et celle de Philippe Barboux maintenant à l'IRCP. En un an, j'ai reçu une robuste formation en chimie du solide qui a clairement orienté mes axes de recherche actuels. Au delà de cet aspect scientifique, cette année de post-doc m'a ouvert les yeux sur la qualité de la recherche en entreprise (tout du moins chez Solvay).

Depuis Octobre 2012, je fais partie du laboratoire de chimie de l'ENS Lyon. Pour être tout à fait honnête, j'ai du mal à imaginer un meilleur endroit pour débuter une carrière de maître de conférences. Pour cela, je tiens en premier lieu à remercier Chantal Andraud, en tant que directrice, de m'avoir accepté dans cette unité. Mes remerciements vont aussi à Philippe Sautet, animateur d'axe du groupe de chimie théorique à mon arrivée pour avoir facilité le démarrage de mes travaux de recherche. J'ai une reconnaissance particulière pour Marie-Laure Bocquet qui s'est notablement investie pour m'accueillir dans les meilleures conditions techniques et scientifiques. Au delà de l'accueil qui m'a été fait, mes remerciements vont à mes collègues théoriciens pour les discussions scientifiques mais surtout pour la vie quotidienne au laboratoire : Carine, David, Elise, Ivan, Martin, Stephan, Tao – et mes collègues expérimentateurs (qui sont aussi nos amis) : Cyrille, Olivier, Anthony, Frédéric… (pour ne citer qu'eux car ils sont très nombreux).

Mais il n'y a pas que des permanents qui ont contribué à mes travaux, mes sentiments vont aussi aux post-doc, doctorants et stagiaires qui ont soutenu mes projets par leur dur labeur : Sigi, Antton, Angel, Pauline et Aria.

Et enfin, un remerciement plus personnel pour celles qui partagent ma vie (et mes lubies sur les minéraux « qui brillent »).

Sommaire

Chapter I: Extended Curriculum Vitae

Tangui Le Bahers

PhD

Nationality: French

Born the 20th of August 1985

http://perso.ens-lyon.fr/tangui.le_bahers/en/

Professional contacts:

Laboratoire de chimie de l'ENS Lyon

46 allée d'Italie

69346 Lyon cedex 07 France

tangui.le_bahers@ens-lyon.fr

tel: +334 72 72 88 46

Professional situation

Maître de Conférence at the **University Claude Bernard Lyon 1** (Section 31)

Attached to the **laboratory of chemistry of the ENS Lyon** (UMR 5182)

Training

2007-2008 Master Chimie-Paristech « Chimie et Physico-chimie pour le vivant et les matériaux »

2005-2008 **Three years of higher education at the Ecole Nationale Supérieure de Chimie de Paris (Chimie Paristech)** leading the engineering diploma (Master degree).

2003-2005 Two years of preparation to be accepted at Chimie Paristech, performed at the Ecole Nationale Supérieure de Chimie de Rennes.

Professional experience

2011-2012 **1 year postdoc** between the research center of Solvay in Aubervilliers (France) and the institute of research of Chimie Paristech (France).
Study of new materials for photovoltaic application.
Supervisors: Philippe Barboux and Thierry Le Mercier

2008-2011 **PhD student** in the laboratory of electrochemistry, chemisry of interfaces and modelling for energy (LECIME, Paris).
Optimization of ZnO based dye-sensitized solar cells by a combined experimental and theoretical approach.
Supervisors: Thierry Pauporté and Ilaria Ciofini

2008 **5 months internship** in the laboratory of electrochemistry and analytical chemistry (LECA, Paris) in the theoretical chemistry group.
Calculations of absorption spectra of molecules used in OLED and dye-sensitized solar cells.
Supervisors: Carlo Adamo and Ilaria Ciofini

2007 **4 months internship** in IFP Energies Nouvelles (Rueil-Malmaison)
Quantum molecular dynamics of ionic liquids.
Supervisor: Theodorus De Bruin

Awards

2013 Prize Eugène Schueller

2008 Prize of alumni association of Chimie Paristech

Bibliometric indexes

- Co-author of 43 articles published in international journals with peer review, including 28 articles after taking office in 2012.
- 3 patents applications based on my post-doc project on BiCuOS.
- 11 oral communications in conferences since taking office, including one oral invited talk.
- 2 invited seminars in chemical companies (L'Oréal and Solvay)
- 3 posters communications since 2012.
- h-index: 20 (30/01/2018, Google Scholar)
- 1782 citations (average of 41 citations/article): cf Figure 1

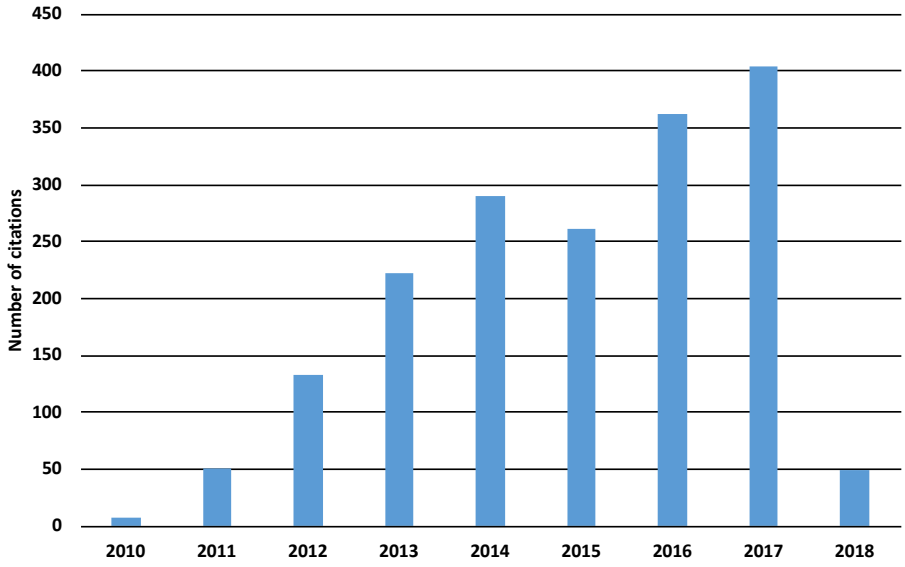

Figure 1: Evolution of the citations among the years (from Google Scholar, 30/01/2018)

Research areas

- **Development of new heterogeneous photocatalysts for water splitting application**. The objective is to design *in silico* new semiconductors, to model the semiconductor/co-catalyst interface and finally to develop a multi-scale modelling of the catalyst used in heterogeneous photocatalysis.
- **Spectroscopic properties of molecules developed for biological applications.** The aim is to understand the one-photon and two-photon absorption, fluorescence, singlet

oxygen production properties of series of molecules developed by Dr. Cyrille Monnereau for fluorescent microscopy and photodynamic therapy.

- **Modelling photochromic natural minerals from the sodalite family.** These minerals have been weakly investigated since recently whose possible high-tech applications have been proposed. This is the reason why I decided to bring an atomistic point of view to the photochromism mechanism.
- Beyond these three main topics, I have contributed to some single projects involving my knowledge in materials science and spectroscopy, on a wide range of research areas including adsorption of magnetic molecules on metallic surfaces, evaluation of the depth of Titan methane lakes…

List of scientific contributions (orals and posters)

Year	Type	Event	Title
2017	Oral	WATOC (München, Germany)	Modeling the photochromism of Sulfur Doped Sodalites using DFT, TD-DFT and SAC-CI methods.
2017	Oral	International Workshop of Nano and Bio Photonics (Vogüé, France)	Modeling the photochromism of Sulfur Doped Sodalites using DFT, TD-DFT and SAC-CI methods.
2017	Poster	Journées des carburants solaires (Autrans, France)	Research Activities of Solar Fuels in the Laboratory of Chemistry of ENS Lyon- Group of Theoretical Chemistry.
2016	Oral	Journées des carburant solaires (Strasbourg, France)	Etudes par DFT de semiconducteurs utilisés dans le domaine du photovoltaicque et de la photocatalyse.
2016	Oral	ACS meeting Physical Chemistry (San Diego, USA)	Semiconductor used in photovoltaic and photocatalytic devices: Insights from DFT calculations
2016	Oral	ACS meeting Energy Fuels (San Diego, USA)	Developments of new semiconductors for water splitting and photovoltaic devices based on DFT computed properties.
2016	Oral	KCC symposium (KAUST, Saudi Arabia)	How DFT can be used to understand semiconductors properties for photovoltaic and photocatalytic applications?
2016	Oral	Multi Responsive Photochromes (Nantes, France)	Investigation of electronic properties of photochromic sodalites by DFT/TD-DFT calculations.
2015	Oral	CECAM	Modeling Photo-Induced Water Splitting: A DFT

		Charge Transfert Modeling in Chemistry (Paris, France)	perspective.
2015	Oral	Journées des perovskites hybrids (Cachan, France)	Propriétés électroniques des composes $PbX_3CH_3NH_3$ utilisés en photovoltaïque.
2014	Oral	Photo4E (Solaize, France)	Ab Initio Optimization of Dye-Sensitized Solar Cells: From Individual Components to Interfaces.
2014	Oral	Rencontre des chimistes théoriciens francophones (Paris, France)	Efficacité des semiconducteurs utilisés en photovoltaïque et photocatalyse.
2014	Poster	Journées des surfaces et interfaces (Lyon, France)	Adsorption of iron and cobalt porphyrins in Ag(111): *Ab initio* prediction of unusual interaction with O_2 and CO.
2013	Poster	DFT13 (Durham, UK)	On density based indexes developed to understand charge transfer transitions.

List of publications

Publications in interational journals

2018

1. B. Mettra, Y. Y. Liao, T. Gallavardin, C. Armagnat, D. Pitrat, P. Baldeck, T. Le Bahers, C. Monnereau, C. Andraud, **A Combined Theoretical and Experimental Investigation of Influence of Bromine Substitution Pattern on the Photophysics of Conjugated Organic Chromophores**, *Phys. Chem. Chem. Phys.* **2018** (DOI: 10.1039/c7cp06535c)

2017

2. M. Iachella, T. Le Bahers, D. Loffreda, **Diffusion Kinetics of Gold and Copper Atoms on Pristine and Reduced Rutile TiO_2 (110) Surfaces**, *J. Phys. Chem. C* **2017**,
3. A. BaQuais, A. Curutuchet. A. Ziani, H. A. Ahsaine, P. Sautet, K. Takanabe, T. Le Bahers, **Bismuth Silver Oxysulfide for Photoconversion Applications : Structural and Optoelectronic Properties**, *Chem. Mater.* **2017**, *29*, 8679-8689.
4. A. Ziani, C. Le Paven, L. Le Gendre, F. Marlec, R. Benzerga, F. Tessier, F. Cheviré, M. N. Hedhili, A. T. Garcia-Esperza, S. T. A. G. Melissen, P. Sautet, T. Le Bahers. K. Takanabe, **Photophysical Properties of $SrTaO_2N$ thin films and Influence of Anion Ordering: A Joint Theoretical and Experimental Investigation**, *Chem. Mater.* **2017**, *19*, 3989-3998 (DOI: 10.1021/acs.chemmater.7b00414).
5. S. Lardhi, A. Curutchet, L. Cavallo, M. Harb. T. Le Bahers, **Ab Initio Assessment of $Bi1-_xRE_xCuOS$ (RE=La, Gd, Y, Lu) solid solution as semiconductor for photocatalytic water splitting**, *Phys. Chem. Chem. Phys.* **2017**, *19*, 12321-12330 (DOI: 10.1039/C7CP01684K)

6. S. N. Steinmann, S. T. A. G. Melissen, T. Le Bahers, P. Sautet, **Challenges in Calculating the bandgap of Triazine-Based Carbon Nitride Structures**, *J. Mater. Chem. A*, **2017** (DOI: 10.1039/C6TA08939A)
7. A. Curutchet, T. Le Bahers, **Modelling the S-Doped Sodalites Using DFT, TD-DFT and SAC-CI Methods**, *Inorg. Chem.* **2017**, *56*, 414-423. (DOI: 10.1021/acs.inorgchem.6b02323)

2016

8. S.T.A.G. Melissen, S.N. Steinmann, T. Le Bahers, P. Sautet, **DFT Perspective on the Thermochemistry of Carbon Nitride Synthesis**, *J. Phys. Chem. C*, **2016**, *120*, 24542-24550. (DOI: 10.1021/acs.jpcc.6b06335)
9. S. Petit, S.T.A.G. Melissen, L. Duclaux, M.T. Sougrati, T. Le Bahers, P. Sautet, D. Dambournet, O. Borkiewicz, C. Laberty-Robert, O. Durupthy, **How Should Iron and Titanium Be Combined in Oxides to Improve Photoelectrochemical Properties?**, *J. Phys. Chem. C*, **2016**, *120*, 24121-24532. (DOI: 10.1021/acs.jpcc.6b05794)
10. I. Gonzalez-Valls, A. Mirloup, T. Le Bahers, N. Keller, T. Cottineau, P. Sautet, V. Keller, **Characterization and charge transfer properties of organic BODIPY dyes integrated in TiO_2 nanotubes based Dye-sensitized Solar Cells**, *RSC Adv.*, **2016**, *6*, 91529-91540. (DOI: 10.1039/C6RA14152H)
11. M. Lepeltier, F. Appaix, Y. Y. Liao, F. Dumur, J. Marrot, T. Le Bahers, C. Andraud, C. Monnereau, **Carbazole-Substituted Iridium Complex as a Solid State Emitter for Two-Photon Intravital Imaging**, *Inorg. Chem.*, **2016**, 55, 9586-9595. (DOI: 10.1021/acs.inorgchem.6b01253)
12. B. Mettra, F. Appaix, J. Olesiak-Banska, T. Le Bahers, A. Leung, K. Matczyszyn, M. Samoc, B. van der Sanden, C. Monnereau, C. Andraud, **A fluorescent polymer probe with high selectivity towards vascular endothetial cells for and beyond non-invasive two-photon intravital imaging of brain vasculature**, *ACS Appl. Mater. Inter.*, **2016**, *8*, 17047-17059. (DOI: 10.1021/acsami.6b02936)
13. E. Nurlaela, H. Wang, T. Shinagawa, S. Flanagan, S. Ould-Chikh, M. Qureshi, Z. Mics, P. Sautet, T. Le Bahers, E. Cánovas, M. Bonn, K. Takanabe, **Enhanced kinetics of hole transfer and electrocatalysis during photocatalytic oxygen evolution by cocatalyst tunig**, *ACS Catalysis*, **2016**, *6*, 4117-4126. (DOI: 10.1021/acscatal.6b00508)
14. N. Bachellier, M. Ormaza, M. Faraggi, B. Verlhac, M. Vérot, T. Le Bahers, M.-L. Bocquet, and L. Limot, **Unveiling nickelocene bonding to a noble metal surface**, *Phys. Rev. B* **2016**, 195403. (DOI: 10.1103/PhysRevB.93.195403)
15. B. Demoulin, M. M. T. El-TahawyA. Nenov, M. Garavelli, T. Le Bahers, **Intramelcular Photoinduced Charge Transfert in Visual Retinal Chromophore Mimics: Electron Density Based Indices at the DFT and post-HF Levels**, *Theor. Chem. Acc.* **2016**, *135*, 96. (DOI: 10.1007/s00214-016-1815-y)
16. D. Cordier, T. Cornet, J.W. Barnes, S.M. MacKenzie, T. Le Bahers, D. Nna-Mvondo, P. Rannou, A.G. Feirrera, **Structure of Titan's Evaporties**, *Icarus,* **2016**, *270*, 41-56. (DOI : 10.1076/j.icarus.2015.12.034)

2015

17. M. K. Bhunia, S. Melissen, M. R. Parida, P. Sarawade, J.-M. Basset, D. H. Anjum, O. F. Mohammed, P. Sautet, T. Le Bahers, K. Takanabe, **Dendritic Tip-on Polytriazine Based**

Carbon Nitride Photocatalyst with High Hydrogen Evolution Activity, *Chem. Mater.* **2015**, *27*, 8237-8247 (DOI: 10.1021/acs.chemmater.5b02974)

18. S. Melissen, T. Le Bahers, S. Steinmann, P. Sautet, **The Relationship Between Carbon Nitride Structure and Exciton Binding Energies: A DFT Perspective**, *J. Phys. Chem. C* **2015**, *119*, 25188-25196 (DOI: 10.1021/acs.jpcc.5b07059)
19. T. Le Bahers, S. Haller, T. Le Mercier, P. Barboux, **Assessing the Use of BiCuOS for Photovoltaic Applications: From DFT to Macroscopic Simulation**, *J. Phys. Chem. C,* **2015***, 119,* 17585-17595 (DOI: 10.1021/acs.jpcc.5b05551)
20. T. Cornet, D. Cordier, T. Le Bahers, O. Bourgeois, C. Fleurant, S. Le Mouélic, N. Altobelli, **Karstification Processes on Titan and on Earth: Towars the Age of Titan's Lacustrine Depressions**, *J. Geophys. Res.-Planets*, **2015**, *120*, 1044-1074 (DOI: 10.1002/2014JE004738)
21. C. Adamo, T. Le Bahers, M. Savarese, L. Wilbraham, G. Garcia, R. Fukuda, M. Ehara, N. Rega, I. Ciofini, **Exploring excited states using time dependent density functional theory and density based indexes**, *Coord. Chem. Rev.* **2015** (DOI: 10.1016j/j.ccr.2015.03.027)
22. T.A. Kandiel, D.H. Anjum, P. Sautet. T. Le Bahers, K. Takanabe, **Electronic structure and photocatalytic activity of wurtzite Cu-Ga-S nanocrystals and their Zn substitution**, *J. Mater. Chem. A*, **2015** (DOI: 10.1039/C5TA01552A)
23. M. Ormaza, P.N. Abufager, N. Bachellier, R. Robles, M. Vérot, T. Le Bahers, M.-L. Bocquet, N. Lorente, L. Limot, **Assembly of Ferrocene Molecules on Metal Surfaces Revisited**, *J. Phys. Chem. Lett.* **2015** (DOI: 10.1021/jz5026118)
24. T. Houwaart, T. Le Bahers, P. Sautet, W. Auwärter, K. Seufert, J.V. Barth, M.-L. Bocquet, **Scrutinizing individual CoTPP molecule adsorbed on coinage metal surfaces from the interplay of STM experiment and theory**, *Surf. Sci.* **2015**, *635*, 108. (DOI: 10.1016/j.susc.2014.12.011)
25. S.T.A.G. Melissen, F. Labat, P. Sautet, T. Le Bahers, **Electronic properties of $PbX_3CH_3NH_3$ (X= Cl, Br, I) compounds for photovoltaic and photocatalytic applications**, *Phys. Chem. Chem. Phys.* **2015**, *17*, 2199 (DOI: 10.1039/C4CP04666H)

2014

26. E. Brémond, T. Le Bahers, G. Ricci, I. Ciofini, C. Adamo, **In silico assessment of the HPLC–UV response coefficients**, *Comput. Theor. Chem.* **2014**, *1040*, 1. (DOI: 10.1016/j.comptc.2014.03.028)
27. T. Le Bahers, M. Rérat, P. Sautet, **Semiconductors Used in Photovoltaic and Photocatalytic Devices: Assessing Fundamental Properties from DFT**, *J. Phys. Chem. C* **2014**, *118*, 5997. (DOI: 10.1021/jp409724c)
28. T. Le Bahers, E. Brémond, I. Ciofini, C. Adamo, **The nature of vertical excited states of dyes containing metals for DSSC applications: insights from TD-DFT and density based indexes**, *Phys. Chem. Chem. Phys.* **2014**, *16*, 14435. (DOI: 10.1039/C3CP55032J)

2013

29. T. Le Bahers, Th. Pauporté, P. P. Lainé, F. Labat, C. Adamo, I. Ciofini, **Modeling dye-sensitized solar cells: from theory to experiment**, *J. Phys. Chem. Lett.* **2013**, *4*, 1044. (DOI: 10.1021/jz400046p)

2012

30. I. Ciofini, T. Le Bahers, C. Adamo, D. Jacquemin, **Through-space charge transfer in rod-like molecules: lessons from theory**, *J. Phys. Chem. C* **2012**, *116*, 11946. (DOI: 10.1021/jp3030667)
31. T. Le Bahers, Th. Pauporté, F. Odobel, I. Ciofini, **Promising anchoring groups for ZnO-based hybrid materials: A periodic density functional theory investigation**, *Int. J. Quant. Chem.* **2012**, *112*, 2062. (DOI: 10.1002/qua.23134)
32. F. Labat, T. Le Bahers, I. Ciofini, C. Adamo, **First-principles modeling of dye-sensitized solar cells: challenges and perspectives**, *Acc. Chem. Res.* **2012**, *45*, 1268. (DOI: 10.1021/ar200327w)
33. D. Jacquemin, T. Le Bahers, C. Adamo, I. Ciofini, **What is the "best" atomic charge model to describe through-space charge-transfer excitations?**, *Phys. Chem. Chem. Phys.* **2012**, *14*, 5383. (DOI: 10.1039/C2CP40261K)

2011

34. O. Lupan, Th. Pauporté, T. Le Bahers, B. Viana, I. Ciofini, **Wavelength-emission tuning of ZnO nanowire-based light-emitting diodes by Cu doping: experimental and computational insights**, *Adv. Fonct. Mater.* **2011**, *21*, 3564. (DOI: 10.1002/adfm.201100258)
35. T. Le Bahers, C. Adamo, I. Ciofini, **A qualitative index of spatial extent in charge-transfer excitations**, *J. Chem. Theory Comput.* **2011**, *7*, 2498 (DOI: 10.1021/ct200308m)
36. O. Lupan, Th. Pauporté, T. Le Bahers, I. Ciofini, B. Viana, **High Aspect Ratio Ternary $Zn_{1-x}Cd_xO$ Nanowires by Electrodeposition for Light-Emitting Diode Applications**, *J. Phys. Chem. C* **2011**, *115*, 14548. (DOI: 10.1021/jp202608e)
37. T. Le Bahers, F. Labat, Th. Pauporté, P. P. Lainé, I. Ciofini, **Theoretical procedure for optimizing dye-sensitized solar cells: from electronic structure to photovoltaic efficiency**, *J. Am. Chem. Soc.* **2011**, *133*, 8005. (DOI: 10.1021/ja201944g)
38. T. Le Bahers, Th. Pauporté, F. Labat, G. Lefevre, I. Ciofini, **Acetylacetone, an Interesting Anchoring Group for ZnO-Based Organic− Inorganic Hybrid Materials: A Combined Experimental and Theoretical Study**, *Langmuir* **2011**, *27*, 3442. (DOI: 10.1021/la103634v)

2010

39. V.-M. Guérin, C. Magne, Th. Pauporté, T. Le Bahers, J. Rathousky, **Electrodeposited nanoporous versus nanoparticulate ZnO films of similar roughness for dye-sensitized solar cell applications**, *ACS Appl. Mater. Inter.* **2010**, *2*, 3677. (DOI: 10.1021/am1008248)
40. T. Le Bahers, S. Di Tommaso, C. Peltier, G. Fayet, R. Giacovazzi, V. Tognetti, A. Prestiani, F. Labat, **Acridine orange in a pumpkin-shaped macrocycle: Beyond solvent effects in the UV–visible spectra simulation of dyes**, *J. Mol. Mod.:THEOCHEM* **2010**, *954*, 45. (DOI: 10.1016/j.theochem.2010.01.031)
41. T. Le Bahers, C. Adamo, I. Ciofini, **Photophysical Properties of 8-Hydroxyquinoline-5-sulfonic Acid as a Function of the pH: A TD-DFT Investigation**, *J. Phys. Chem. A* **2010**, *114*, 5932. (DOI: 10.1021/jp1014498)
42. T. Le Bahers, F. Labat, Th. Pauporté, I. Ciofini, **Effect of solvent and additives on the open-circuit voltage of ZnO-based dye-sensitized solar cells: a combined theoretical and experimental study**, *Phys. Chem. Chem. Phys.* **2010**, *12*, 14710. (DOI: 10.1039/C004358c)

2009

43. T. Le Bahers, C. Adamo, I. Ciofini, **Theoretical determination of the pK_as of the 8-hydroxyquinoline-5-sulfonic acid: A DFT based approach**, *Chem. Phys. Lett.* **2009**, *472*, 30. (DOI: 10.1016/j.cplett.2009.02.072)
44. T. Le Bahers, Th. Pauporté, G. Scalmani, C. Adamo, I. Ciofini, **A TD-DFT investigation of ground and excited state properties in indoline dyes for dye-sensitized solar cells**, *Phys. Chem. Chem. Phys.* **2009**, *11*, 11276. (DOI: 10.1039/B914626)

Patents:

2015

- T. Le Mercier, P. Barboux, T. Le Bahers, **Mixed oxides and sulfides of bismuth and copper for photovoltaic use,** PCT WO2015/150591 A1, published the 8th October 2015
- T. Le Mercier, P. Barboux, T. Le Bahers, **Mixed oxides and sulfides of bismuth and silver for photovoltaic use,** PCT WO2015/150592 A1, published the 8th October 2015

2014

- T. Le Mercier, P. Barboux, T. Le Bahers, **Mixed bismuth and copper oxides and sulfides for photovoltaic use,** PCT WO2014/049172 A2, published the 3rd April 2014

Experience in supervising master students, PhD students and post-doctorates

Period	Name	Position	Title
2018-2019	**Nina Tyminska**	Post-doctorate 1 year	Modelling the semiconductor/co-catalyst interface for water splitting
2016-2019	**Antton Curutchet**	PhD student 3 years	DFT investigations of photocatalysts for photo-induced water-splitting.
2016-2018	**Angel Garcia**	Post-doctorate 20 months	Modelling the semiconductor/co-catalyst interface for water splitting: from the atomic scale to the macroscopic scale.
2017	**Aria Gheeraert**	M1 student 3 months	Photochromism modelling of sulfur doped sodalite by DFT and TD-DFT.
2017	**Pauline Colinet**	M2 student 6 months	Water oxidation on cobalt oxide: DFT mechanistic study with electrochemical potential control.
2016	**Antton Curutchet**	M2 student 6 months	Ab initio modelling of tenebrescent sodalites.
2014-2016	**Sigmund Melissen**	Post-doctorate 26 months	DFT modelling of semiconductors for designed for water splitting devices.

Administrative, animating and scientific responsibilities

- Member of the chemistry and biochemistry department council of the University Claude Bernard Lyon 1;
- Member of the administrative board of the GDR Solar Fuels;
- Co-organizer of the congress "Rencontres des chimistes théoriciens francophones" in July 2016 in Lyon (more than 150 participants);
- Organizer of the group seminars;
- Reviewer for: Chemistry of Materials, Physical Chemistry Chemical Physics, RSC Advances, Journal of Physical Chemistry, Journal of Catalysis, ACS Catalysis, Journal of Molecular Modelling, Theoretical Chemistry Account…

Collaborations

- Pr. Kazuhiro Takanabe, KAUST (Saudi Arabia), on the water splitting project.
- Pr. Mika Lastusaari, Turku University (Finland), on the tenebrescent minerals project.
- Dr. Cyrille Monneau, ENS Lyon (France), on the singlet oxygen production project.
- Dr. Marie-Laure Bocquet, ENS (France), on adsorbed magnetic molecules project.

Funding contracts

- **2014-2020: KAUST Water splitting –** Modelling of the water splitting photocatalysts – Local PI – 731 k€.
- **2017-2021: ANR JCJC TeneMod –** Modelling of photochromic natural minerals – PI – 154 k€

Teaching activities

The detail of my teachings is given in the Table 1, for all teachings larger than 10h/year. The Figure 2 summarizes this table.

Period	Name	Type	Level	Volume (in hour eq. TD)
2012-2013	Chimie-Physique	TP	L3	12
	Sciences de la matière	TD	L1	80
	Cinétique	TP	L2	20
	Modélisation Moléculaire	TD	M1	44
2013-2014	Chimie-Physique	TP	L3	16
	Sciences de la matière	TD	L1	67
	Cinétique	TP	L2,L3	40
	Modélisation Moléculaire	TD	M1	44
2014-2015	Chimie-Physique	TP	L3	16
	Sciences de la matière	TD	L1	65
	Cinétique	TP	L2,L3	40
	Constitution de la matière	TD	L1	32
	Modélisation Moléculaire	TD	M1	44
2015-2016	Chimie-Physique	TP	L3	28
	Sciences de la matière	TD	L1	63
	Cinétique	TP	L2	20
	Constitution de la matière	TD	L1	30
	Modélisation Moléculaire	TD	M1	44
	Spectroscopie	CM	M1	15
2016-2017	Chimie-Physique	TP	L3	32
	Sciences de la matière	TD	L1	44
	Cinétique	TP	L2	20
	Constitution de la matière	TD	L1	31
	Modélisation Moléculaire	CM,TD	M1	39
	Spectroscopie	CM	M1	15
	Chimie du solide	CM	M1	15
2017-2018	Chimie-Physique	TP,TD	L3	47
	Sciences de la matière	TD	L1	18
	Cinétique	TP	L2,M1	20
	Constitution de la matière	TD	L1	28
	Modélisation Moléculaire	CM,TD	M1	39
	Spectroscopie	CM	M1	15
	Chimie du solide	CM	M1	15

Table 1: Volume of each teaching for each scholar year. CM, TP and TD means “cours magistraux”, “travaux pratiques” and “travaux dirigés” respectively.

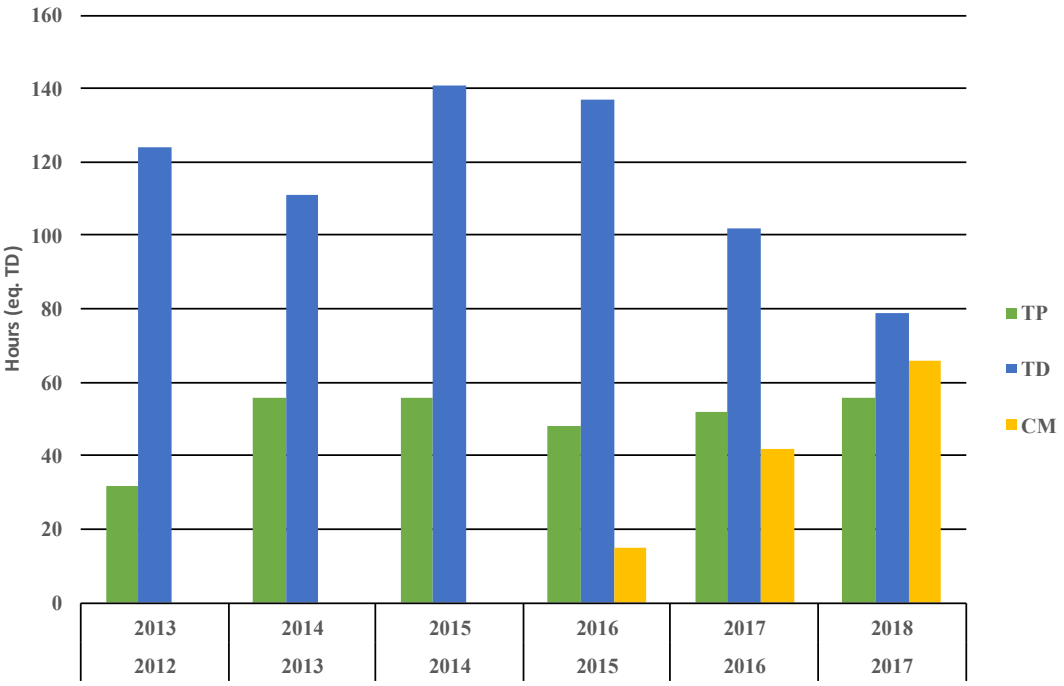

Figure 2: Evolution of my teachings among the years. CM, TP and TD means "cours magistraux", "travaux pratiques" and "travaux dirigés" respectively.

Popularization

- 2014, 2015, 2016, 2017: Conferences to the "Université Ouverte" on the topic of photovoltaic entitled "Les panneaux solaires dans l'habitat: le cas des celleules solaires à colorants".
- 2017: Supervisor of a "collège" internship during one week (Damian Menville, 14 years old).
- 2017: Presentation given during the event "Pint of Science" about the photochromism of sodalite.
- 2014 and 2017, consultant for students on "TIPE" projects on the topic of dye sensitized solar cells.

Chapter II: Summary of my PhD work

I. Context and project

In 1991, Grätzel and O'Regan published a pioneer work presenting the possibility to develop a solar cell technology based on a molecular dye adsorbed on a mesoporous wide-bandgap semiconductor oxide.[1] This was the starting of the Dye-Sensitized Solar Cells adventure. Beyond the principle of a new photovoltaic technology, the first solar cell presented in this article achieved a photoconversion efficiency as high as 7%! From that point, all groups capable to synthetize and deposit mesoporous oxides on conductive glass started to build their own DSSCs. Several combinations of dyes and oxides were tested, leading to dozens and dozens of solar cells characteristics sometimes difficult to rationalize considering the large number of parameters involved in the composition of the DSSC and in its working principle.[2,3] In that context, the computational chemistry has been a powerful tool to bring an atomistic point of view suitable to simulate some of the elementary steps of the working principle of DSSC opening the way of an understanding and a rational design of DSSCs.

The "Laboratoire d'électrochimie, de chimie des interfaces et de modélisation pour l'énergie" (LECIME), known today as "Institut de Recherche de ChimieParisTech" (IRCP), had developed a technology of electrodeposition of mesoporous zinc oxide (ZnO) on conductive glass (Fluor doped Tin Oxide, SnO_2:F, FTO) under the work of Dr. Thierry Pauporté.[4] In the same laboratory, the group of Pr. Carlo Adamo and Dr. Ilaria Ciofini investigated the capacities of DFT and TD-DFT to simulate electronic and spectroscopic properties of dyes in solution or adsorbed on surfaces.[5,6] My PhD project was built in this context, both under the direction of Thierry Pauporté and Ilaria Ciofini, entitled "Optimization of ZnO based DSSCs by a joined experimental and theoretical approach". Dr. Philippe Lainé quickly joined this project, bringing his knowledge in the synthesis of organic dyes characterized by a pyridium group.[7]

II. The methodology

II.1 Electrodeposition of ZnO

Dr. Thierry Pauporté developed, in collaboration with Dr. Daniel Lincot and Dr. Tsukasa Yoshida, a protocol to deposit mesoporous ZnO on top of any conductive electrodes[8–10] that was applied during my PhD on FTO electrodes. Briefly, the electrodeposition is performed by applying a -1.0 V (vs SCE) to a FTO electrode (usually around 3 cm^2 of area) immersed into a water solution containing $ZnCl_2$ (5 mM), Eosin Y (50 microM) and under constant oxygen bubbling at 70°C. At that potential, O_2 is reduced into OH^-, precipitating $Zn(OH)_2$ and quickly dehydrated to ZnO. The role of Eosin Y is to create pores in the growing ZnO. The Figure 3 presents SEM pictures of the final ZnO layer, showing a global thickness of few micrometers and containing pores of around 5nm in diameter. I used this methodology to make all the FTO/ZnO DSSCs electrodes.

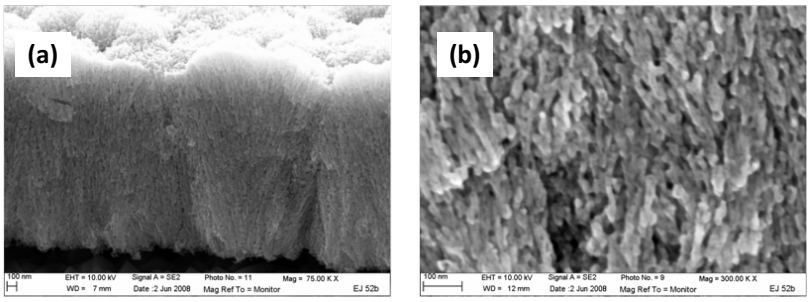

Figure 3: (a) SEM cross section of electrodeposited ZnO. (b) zoom on this cross section.

II.2 Solar cell building and characterization

The DSSCs were built and characterized in the group of the Thierry Pauporté, using a protocol I developed. The two main characterizations were J-V curves under AM1.5 simulator and Incident Photon Converted to electron Efficiency (IPCE).

II.3 Dyes investigated

During this PhD, I used commercial dyes from the indoline family called D131, D102 and D149 known to be very efficient with ZnO based electrodes. In collaboration with Philippe Lainé, I performed the synthesis of three dyes characterized by a pyridinium chemical group. They are made of an electron donor group, aniline or N-dimethylaniline, an electron acceptor, branched or fused pyridinium, and a carboxylate group for the adsorption of the dye on the ZnO (See Figure 4).

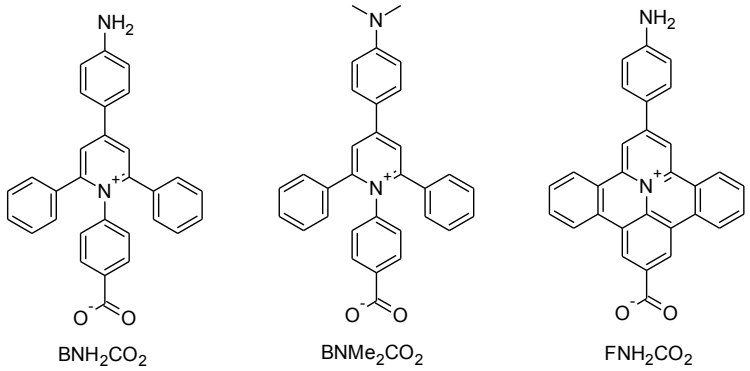

Figure 4: Structures of the three dyes investigated.

II.4 Modeling by DFT and TD-DFT

The simulations of the spectroscopic properties of the dyes were performed by TD-DFT with the development version of the Gaussian09 code.[11] Except otherwise specified, the functional chosen was the global hybrid PBE0 along with the Gaussian basis set 6-31+G(d).[12,13] The solvent, acetonitrile, was modeled by a continuum approach (conductor like polarizable continuum model, CPCM).[14,15] This approach, leads to accurate simulation of absorption spectra of organic molecules.[16,17]

The electronic structure of the dye adsorbed on the ZnO surface was modeled by DFT in Periodic Boundary Conditions (PBC) with the CRYSTAL09 code.[18] This code uses Gaussian type of basis set to build the Block functions used in PBC. The localized nature of the basis set allows to use efficiently hybrid functionals that are very accurate to simulate electronic structure of both organic molecules and d^0 and d^{10} based semiconductors like ZnO. The functional chosen was PBE0 and double ζ-basis+polarization set.

III. Main results

III.1 Influence of the electrolyte composition

The photovoltage of a DSSC, noted V_{oc}, is an important characteristic of the cell. It is directly related to the photoconversion efficiency (η), through the formula 1.

$$\eta = \frac{V_{OC} J_{SC} FF}{P_{inc}} \qquad (1)$$

In a DSSC, this photovoltage corresponds to the energy gap between the Fermi level of the electron in the oxide (generally assimilated to the conduction band level) and the electrochemical potential of the redox couple surrounding the dye. With this very simple point of view, one can assume that the photovoltage is only fixed by the choice of the oxide and the redox couple without any possibilities of improvement. But it has been observed and

published that the choice of the solvent containing the electrolyte and in contact with the oxide has a large influence on the V_{oc}. We performed a systematic investigation of ZnO solar cells sensitized by the D149 dye.[19,20] The influence of the choice of the solvent for the electrolyte between acetonitrile, nitromethane and dimethyl-formamide on the V_{oc} was measured and correlated to the position of the conduction band of the corresponding molecule adsorbed on ZnO(100) surface computed by DFT.

III.2 DSSC based on ZnO sensitized by pyridinium dyes

Under the supervision of Dr. Lainé, I performed the synthesis of the three pyridinium dyes presented in Figure 4. They were tested both on ZnO and TiO_2 based DSSCs.[21,22] The best photoconversion efficiency was obtained for the fused pyridinium dye (FNH_2CO_2) both for ZnO (η=0.6%) and TiO_2 (η=1.3%) but remained very low. The DFT calculations have shown that the dye did not inject efficiently the electron in the conduction band of the semiconductor because the pyridinium acceptor group is a "too strong" acceptor (i.e. a better electron acceptor than the oxide). The simulation of the injection was done by computing the reduced system and integrating the spin density of the reduced form. From these results, the IPCE measurement has been simulated and compared to the experimental one confirming that the electron injection was the bottleneck of the efficiency for these dyes. Using this computational protocol, we have optimized the composition of the electrolyte to tune the injection of the dye by adding Li^+ ion (increase of IPCE) or tertbutyl-pyridine (decrease of IPCE). The comparison between the simulated and measured IPCE are presented on Figure 5.

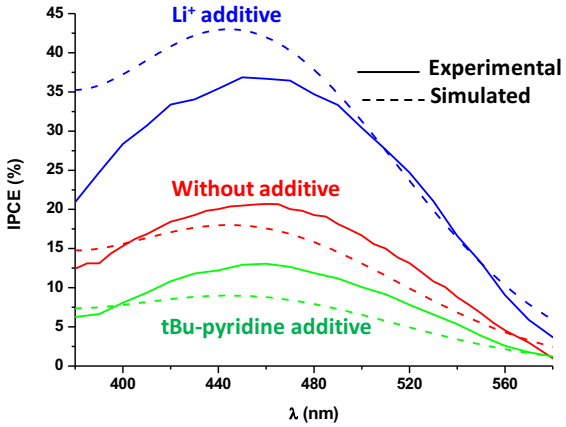

Figure 5. Simulated and experimental IPCE curves of F1 dye adsorbed on ZnO as a function of electrolyte composition.

III.3 Charge transfer indexes based on the variation of the electron density

During this PhD, I developed a series of charge transfer indexes based on the difference of the electron density between the ground and excited states.[23,24] Contrary to the Tozer's index

(Λ)[25] based on the overlap of the module of the orbitals involved in an electronic transition, and to its simplified version recently proposed by De Angelis et al. in the framework of DSSCs applications[26], the index D_{CT} is based on the variation of the electron density between a given excited state and the ground state ($\Delta\rho=\rho_{EX}-\rho_{GS}$). In particular, D_{CT} defines the spatial distance between the two barycenters of the density depletion and density enhancement distributions upon excitation. This approach has some advantages:

· The visualization of $\Delta\rho$ allows the qualitative assignment of the character of the transition. This can avoid a tedious assignment procedure when several monoelectronic excitations contribute to the same electronic transition.

· The distance of charge transfer, D_{CT}, gives a quantitative estimation of the charge transfer length that can help to compare different families of dyes.

· $\Delta\rho$ can be used also to compute other fundamental properties of the transition such as the fraction of electron transferred upon light absorption (q_{CT}), the centroids of the depletion and enhancement distributions…

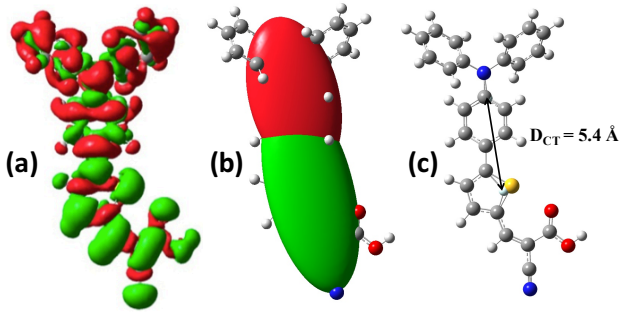

Figure 6: (a) $\Delta\rho$ computed by TD-DFT for a donnor-acceptor prototype molecule. (b) corresponding centroids. (c) distance between the barycenters of the two centroids.

Chapter III: The photo-induced water splitting

I. Context, mechanisms and photocatalysts

I.1 Storage of solar energy

I am not going to start this introduction on the importance to develop energy productions alternative to the fossil fuels. I assume that all the readers of this text are aware of the global warming, of the problems coming from fossil fuels and are well convinced that the light from the sun brings enough energy on Earth to meet the energy demand of humanity. We must wonder how to convert and store this energy. This introduction begins with the photovoltaic technologies. The first solar cell developed to produce electricity were proposed in the 50's by Bell's laboratories but this way of electricity production really started to be deeply and largely investigated during the 70's.[27] Nowadays, the success of the photovoltaic story can be viewed on the frequently updated NREL photovoltaic chart presenting the maximum efficiencies of several photovoltaic technologies (Figure 7).[28] At first sight, what is really surprising is the large number of photovoltaic technologies developed, with constant photoconversion improvements. And after a fine look, it appears that the institutions having the best efficiencies for each technology are not necessarily academic but can be industrial companies indicating the broad interest of all the scientific actors for these technologies. Beyond these records obtained in laboratories, the photovoltaic technologies are real life electricity production technologies. But contrary to what is visible on the NREL chart, there are much less photovoltaic technologies available in the market. Actually, only the crystalline silicon (89% of the market) and some thin film technologies (CdTe and CIGS, 11% of the market) are really installed to produce electricity.[29] This highlights the difficulty for a technology to go from the laboratory to real applications. This reality is crueler when looking at the real place of the photovoltaic on the total electricity produced in France, estimated at 1.9%.[30]

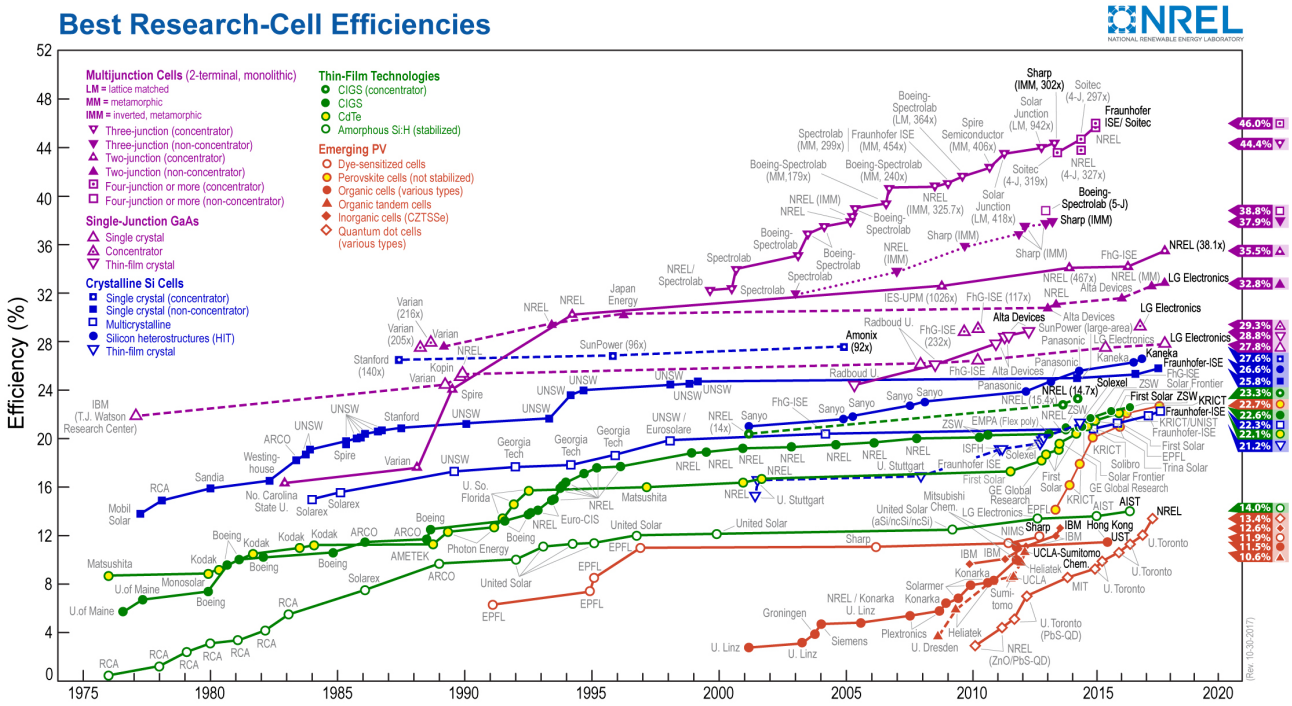

Figure 7: NREL photovoltaic chart presenting the evolution of photoconversion efficiencies for several photovoltaic technologies. This plot is courtesy of the National Renewable Energy Laboratory, Golden, CO.

We could write dozens of pages to explain why photovoltaic technologies, although very investigated and extremely well developed, are so weakly used for real production. From my personal point of view, this is mainly for political and economic strategy reasons but this is not the subject of this manuscript. We have to admit that photovoltaic technologies suffer from some drawbacks. The main one is probably the hatched production of electricity, stopped during the night and variable during the day depending on the weather. During a day, the best period for electricity production by photovoltaic (around noon) in general doesn't overlap very well with the peaks of electricity consumption (generally the morning and the evening). Thus, comes the necessity to store this photovoltaic electricity and re-inject it into the network when needed. Three approaches are developed to store this solar energy.

1- The first one, already used, is by "mechanical" potential like by pumping water into high depth tanks and using the water flow to create electricity back when necessary. Technologically speaking, this method is already known and applicable but the global efficiency of this storage is very low.

2- The second approach is through electrochemical energy by batteries (lithium, redox flow, lead-acid…). This is a very investigated field of research that has lead to the development of several technologies. The most well-known new battery technology is probably the one based on lithium. These batteries are now mature technologies, intensively produced

and used in applications going from the smart phones to the electrical cars and even electrical planes. The main drawback of these technologies is probably the difficulty to obtain both a good energy capacity (like in lithium batteries) and a good power capacity (like supercapacitors). The electrochemical energy storage technologies are frequently presented by Ragone plot (see Figure 8).

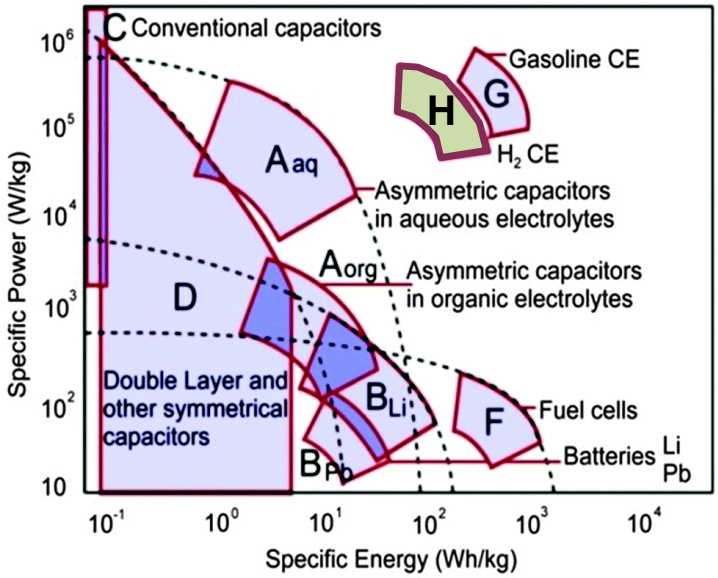

Figure 8. Ragone plot of several energy storage technologies. Hydrogen is in light green. From ref 31

3- The last form of energy storage is under chemical energy. The idea is to use the electricity generated by the solar panels to induce electrochemical reactions (reduction, oxidation or both) producing valuable molecules with the ability to generate energy on demand or valuable molecules for the chemical industry. The two main investigated reactions are namely the CO_2 reduction[32–34] and the water splitting[35,36] corresponding to the two half reactions of water oxidation (2) and proton reduction (3).

$$2H_2O \rightarrow O_2 + 4H^+ + 4e^- \quad E° = 1.23 \text{ V (vs SHE)} \quad (2)$$

$$2H^+ + 2e^- \rightarrow H_2 \quad E° = 0.0 \text{ V (vs SHE)} \quad (3)$$

Since my arrival at the laboratory of chemistry of ENS Lyon, I mainly worked on water splitting. Thus, the discussion will now focus on this reaction but some of the concepts presented now can be simply transferred or adapted for the CO_2 reduction.

The main objective of overall water splitting is to produce hydrogen. This small molecule can be used in fuel cells to generate back electricity. The place of hydrogen in Ragone plot indicates that this fuel has both a large energy density and a large power density (Figure 8). Add to that, the fact that the combustion of H_2 produces only H_2O, H_2 appears to be one of the most interesting fuel. But H_2 doesn't bring only advantages: it is highly explosive in O_2

containing atmosphere. It must be stored compressed or as hydrides, difficult to develop technologically. It diffuses easily in all common materials (like steel). Because of these very strong advantages and drawbacks, the H_2 cycle (production, storage, distribution and combustion) is the topic of many academic and industrial fields of research.

We are now going to focus on the water splitting technologies, putting aside all the research areas dedicated to H_2 storage, distribution or consumption. These last issues, while very interesting, are not the topic of my research activities presented in this document.

I.2 The photocatalytic water splitting technologies

As said previously, water splitting is the combination of two half-electrochemical reactions called oxygen evolution reaction (OER, reaction (2)) and hydrogen evolution reaction (HER, reaction (3)). The first photo-induced water splitting technology we can imagine is simply by connecting a solar panel to an electrolyser to split water and produce H_2. Another technology consists in directly using the electrons and holes generated by a the solar panels immersed in water to perform OER and HER, without any external circuit. For the last technology, the material responsible of the photoresponse activity can be dispersed in water as a powder to achieve the highest active surface area possible. This material is called the photocatalyst because it both absorbs the sunlight and performs the two half reactions.

The comparison of the economic viability of all these technologies of water splitting has been the subject of several articles.[37–39] Several water splitting solar cell architectures were investigated, assuming several working conditions. It is difficult to compare these articles because the assumptions on the materials properties or on the architectures considered are generally not the same. But, to try to extract some key conclusions, in principle, the technology consisting to a direct water splitting should be more profitable (production cost: 2 $/kg.$H_2$) compared to a solar panel connected to an electrolyser (production cost: 4 $/kg.$H_2$).[37] Unfortunately, to connect a solar panel to an electrolyser is already technologically possible while efficient photocatalysts to directly produced H_2, assumed in the economic simulation, are not available yet. Thus, up to now, this best way to produce H_2 with sunlight is still to connect a photovoltaic cell to an electrolyser.

This economical consideration opens our eyes on the necessity to develop very efficient water splitting photocatalysts if we want this technology to be considered for real H_2 production. This is the reason why I decided to work on the development of new water splitting photocatalysts.

I.3 Focus on the photocatalysts

Heterogeneous catalysts developed for water splitting have generally the architecture presented in Figure 9.[36,40] It is made of semiconductor particles covered by co-catalyst particles, adapted for OER or HER.

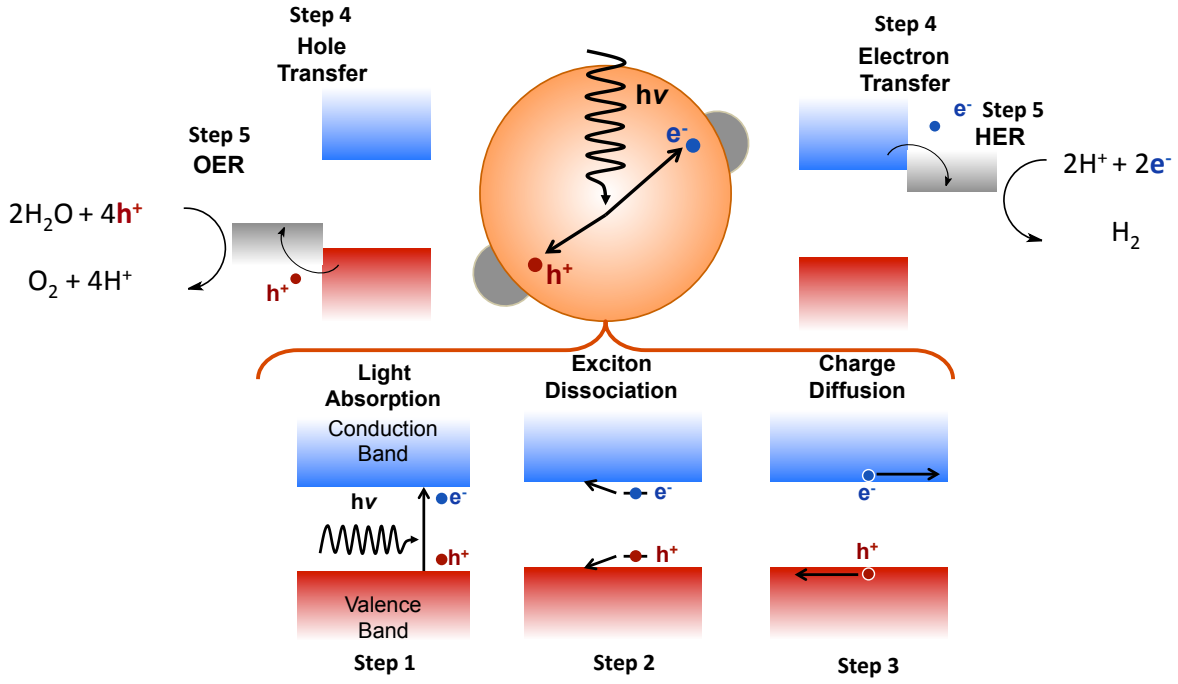

Figure 9. Structure of a photocatalyst with the semiconductor in orange and the co-catalysts in grey. Valence and conduction bands of the semiconductor are in red and blue respectively.

The working principle can be splitted in several steps, as depicted in Figure 9. The efficiency of these steps is mainly governed by several properties of the semiconductor, the co-catalyst or the interface between the two.

Step 1: It corresponds to the light absorption by the semiconductor creating an electron (e^-) and hole (h^+) pair called exciton. The light absorption is mainly governed by the bandgap ($\mathbf{E_g}$) in a semiconductor that can bee seen as the difference in energy between the top of valence band and the bottom of conduction band. In short, the bandgap must be low enough to absorb the maximum of photons and large enough to produce electrons and holes having enough energies to perform the two half reactions. For water splitting, the minimum bandgap to perform the overall water splitting is 1.23 eV. But it has been shown that, to take into account the energy loss due to all the electron transfers and due to entropic loss, the bandgap of the semiconductor must be above 1.8 eV and more ideally between 2.0 and 2.5 eV.[37,41] The Figure 10a presents the variation of the solar to hydrogen efficiency as a function of the bandgap of the semiconductor. This simulation includes some models of the energetic losses

cited previously. It is interesting to see the large difference between the maximum photoconversion efficiency between a standard p-n junction photovoltaic cell (around 35 %) and the maximum solar-to-hydrogen efficiency (STH, around 12%) for a one semiconductor based water splitting catalyst. Actually, some researches think that the community should focus on multijunction catalysts having at least two semiconductors to achieve higher efficiencies (as shown by the figure 10b). The multijunction technologies are clearly more difficult to develop and this is the reason why I preferred to focus, up to now, on single semiconductor catalysts.

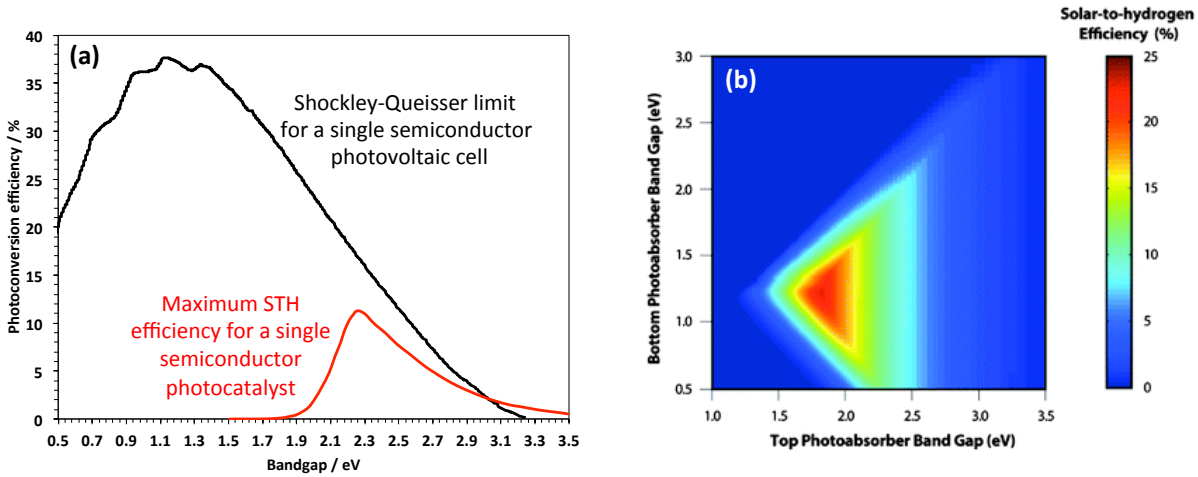

Figure 10. (a) Comparaison between the Schockley-Queisser limit of a photovoltaic cell and the Solar-to-Hydrogen (STH) efficiency of a photocatalysts as a function of the bandgap of the semiconductor. (b) STH efficiency of two-junction photocatalysts as a function of the bandgaps of the two semiconductors. From Ref 37

Beyond the value of the bandgap, its nature plays also an important role (direct or indirect) because it will affect the absorption coefficient of the semiconductor. This aspect will be discussed when necessary in the document.

Step 2: The exciton dissociation. After light absorption, the electron and the hole are bound creating a particle called exciton that can be seen as a kind of hydrogen atom inside the material. The electron and the hole must be separated to perform the OER and HER. The exciton ionization energy is called exciton binding energy, noted $\mathbf{E_b}$. This energy should be lower than room thermal energy (~25 meV at room temperature) to have free charge carriers. If the exciton is not dissociated, it will quickly recombine losing the energy of the photon. The exciton binding energy is mainly governed by the dielectric constant of the material, noted $\boldsymbol{\varepsilon_r}$. The dielectric constant represents the ability of the material to screen charges. The larger the dielectric constant, the easier it will be to dissociate the exciton. As a matter of fact, materials frequently used in photovoltaic (Si, CdTe, GaAs…) have a dielectric constant

higher than 10 and their $\mathbf{E_b}$ is always lower than 25 meV. This value of 10 for $\boldsymbol{\varepsilon_r}$ can be seen as a target to develop new semiconductors for water splitting.

Step 3: Charge carriers diffusion. Once the exciton dissociated, electrons and holes must diffuse toward the surface to perform the OER or the HER. The diffusion is characterized by the diffusion coefficient, **D**, of the charges related to the charge carrier mobilities, **μ**, by Einstein relationship (equation (4)). The mobility is linked to the effective masses, **m***, and the collision time, **τ** (equation (5)).

$$D = \frac{k_B T}{e} \mu \tag{4}$$

$$\mu = e \frac{\tau}{m^*} \tag{5}$$

There is no fundamental lower limit for the value of the charge carrier mobilities or effective masses. But empirically, by analysing all semiconductors efficient for photovoltaic applications, it appears that they all have a mobility higher than 10 $cm^{-2}.s^{-1}.V^{-1}$ and an effective mass lower than 0.5 electron mass at least in one crystallographic direction. Based on this empirically observation, all semiconductors having an effective mass lower than 0.5 m_e for holes and electrons can be considered to have good charge carrier mobilities.

Step 4: Charge transfer toward the co-catalyst. In general, a good semiconductor for generating free charge carriers is not good to perform the two half reactions OER and HER. In other words, the activation energy or the overpotential of the reaction is large on the surface of the semiconductor. This is the reason why the semiconductor surface is decorated by a material called co-catalyst having a better activity toward the chemical reactions investigated. The electron or hole transfer must be efficient to have a maximum of charges collected by the co-catalyst. This step depends on the quality of the interface between the co-catalyst and the semiconductor. The main thermodynamic criterion for an efficient transfer is a conduction band energy higher in energy than Fermi level of the co-catalyst for the HER and a valence band energy lower than the Fermi level of the co-catalyst for the OER.

Step 5: The electrochemical reactions. This step corresponds to the OER and HER strictly speaking. It is the electrochemical oxidation of water and reduction of protons. This step proves that photocatalytic water splitting is very similar to water electrolysis. The current used to split water in photocatalysis comes from the charge dynamics inside the semiconductor. While in an electrolyser, it comes from a potentiostat. In other words, photocatalytic water splitting can be seen as electrocatalytic water splitting, which applied potential is not chosen by the experimentalist but depends on the efficiency of the

semiconductor to absorb the light and to generate electrons and holes. For that reason, co-catalysts are mainly developed and investigated in "classical" electrocatalysis before being implemented in photocatalysis.

The efficiency of this step is mainly governed by the overpotential (noted η) associated to the co-catalyst. The overpotential corresponds to the extra energy (or the extra potential) needed to perform one half reaction beyond the thermodynamic limit, as presented schematically in Figure 11. The perfect co-catalyst has no overpotential. The discussion on overpotential will be developed in the section dedicated to the study of cobalt oxide as co-catalyst for OER.

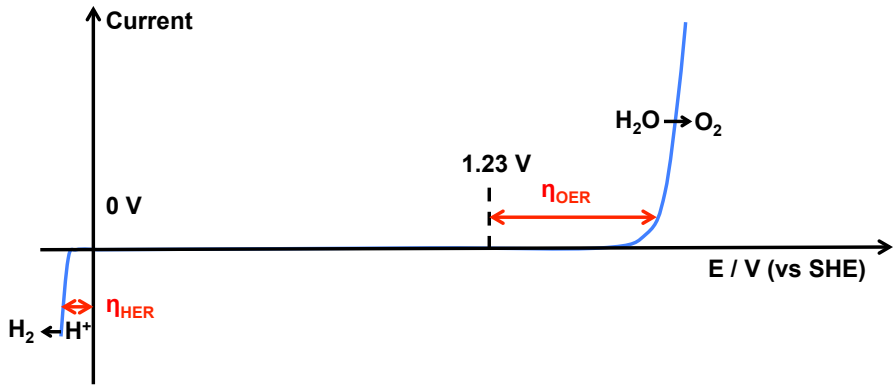

Figure 11. Schematic J-V curve expected for a material having both OER and HER co-catalyst.

Step 6: Fluid mechanics and diffusion. This step is not presented in Figure 9 but presents phenomena happening at the scale much larger than atomic scale, mainly inside the electrolyte where reactions take place. This is a really important aspect in the working principle of a water splitting device and probably important improvements of the photocatalytic efficiencies could be obtained by a smart design of the electrolyte. But the modelling of these phenomena goes beyond my knowledge and my capacities. I have not worked on it up to now and this topic won't be discussed specifically in this document.

II. Semiconductors: Computational methodology

Related Articles:

- T. Le Bahers, M. Rérat, P. Sautet, , *J. Phys. Chem. C* **2014**, *118*, 5997.
- T. Le Bahers, S. Haller, T. Le Mercier, P. Barboux, *J. Phys. Chem. C,* **2015**, *119,* 17585.

II.1 Computation of bulk semiconductor properties

During the period 2012-2016 I mainly worked on the dynamics of charge carriers generation and diffusion inside the semiconductor, corresponding to the steps 1-3 in Figure 9. The

Table 2 summarizes the target value of some bulk properties of the semiconductor to achieve good efficiencies in sunlight absorption, exciton dissociation and charge carriers diffusion.

Solar spectrum absorption	Exciton dissociation	Charge carrier diffusion
1.1 eV < $\mathbf{E_g}$ < 1.4 eV (PV)	$\mathbf{E_b}$ < 25 meV	$\boldsymbol{\mu}$ > 10 $cm^2.V^{-1}.s^{-1}$
1.8 eV < $\mathbf{E_g}$ < 2.5 eV (PEC)	$\boldsymbol{\varepsilon_r}$ > 10	$\mathbf{m^*}$ < 0.5 m_e

Table 2: Requirements on the semiconductors properties for photovoltaic application. PV and PEC mean photovoltaic and photoelectrochemical respectively.

All these properties were computed by DFT or by employing some models using DFT calculations. Here is the methodology I used to compute these properties:

Band Gap. The bandgap, $\mathbf{E_g}$, is computed as the difference between the minimum energy of the conduction band and the maximum energy of the valence band. These energies are obtained by solving self-consistently the monoelectronic Kohn-Sham equations. The bandgap here obtained is called the monoelectronic bandgap ($\mathbf{E_g}$(mono)). It is related to the optical bandgap ($\mathbf{E_g}$(opt)) by the formula (6) where EA and IP are the electron affinity and the ionization potential respectively and $\mathbf{E_b}$ the exciton binding energy:

$$\mathbf{E_g}(\text{opt}) = \text{EA} - \text{IP} - \mathbf{E_b} \approx \mathbf{E_g}(\text{mono}) - \mathbf{E_b} \qquad (6)$$

In other words, I have assumed that the ionization potential and the electron affinity can be approximated by the band positions obtained by DFT. This assumption is very rough for molecules but works relatively well (for the precision we are looking for) for solids.[42] Because $\mathbf{E_b}$ is very small (few dozens of meV) compared to the monoelectronic bandgap (few eV), in general, $\mathbf{E_g}$(mono) and $\mathbf{E_g}$(opt) are very close. In the text, I will use the general word bandgap to speak about $\mathbf{E_g}$(mono) and $\mathbf{E_g}$(opt) indiscernibly. Of note, a better simulation of optical bandgap can be done by using post-DFT calculations, such as GW along with the Bethe-Salpeter equations, taking into account the exciton formation during the light absorption process.[43,44]

Dielectric constant. When an electric field ($\vec{E}$) is applied on a dielectric material, an electric displacement field ($\vec{D}$) appears within it. Both electric fields are linked by the dielectric constant $\boldsymbol{\varepsilon_r}$.

$$\vec{\mathrm{D}} = \varepsilon_0 \varepsilon_\mathrm{r} \vec{\mathrm{E}} \qquad (7)$$

This dielectric constant represents the ability of a dielectric material to screen the external electric field by the apparition of a polarization. This polarization comes from the reorganization of the electron density or from the motion of the ions constituting the material.

The dielectric constant induced by the electron density is named $\boldsymbol{\varepsilon}_\infty$ and the contribution of the dielectric constant involving the ionic motions is noted $\boldsymbol{\varepsilon}_{\mathbf{vib}}$. Finally we have:

$$\varepsilon_r = \varepsilon_\infty + \varepsilon_{vib} \quad (8)$$

The electronic contribution to the static dielectric tensor can be evaluated through a coupled-perturbed Hartree-Fock/Kohn-Sham (CPKS) scheme adapted to periodic systems or by applying an electric field on the system during the SCF procedure. I have been using generally the second approach because, while more time consuming, it takes into account local field effects because of the SCF nature of the calculation.

The vibrational contribution is computed from the phonon spectrum, following the formula (6). ν_p is the phonon frequency of mode p, V is the unit cell volume, and Z_p is the mass-weighted mode effective Born vector. The intensity I_p of IR absorbance for a given mode p is proportional to $|Z_p|^2$.

$$\varepsilon_r = \varepsilon_\infty + \varepsilon_{vib} = \varepsilon_\infty + \frac{4\pi}{V}\sum_p \frac{Z_p^2}{\nu_p^2} \quad (9)$$

Effective masses. For transport properties, only the effective mass is computed. The mobilities depend on the collision time, τ (equation 5) that is extremely experimental dependent and cannot be evaluated easily theoretically. The effective mass is related to the curvature of the bands at the top of the valence band or at the bottom of the conduction band. It can be obtained by fitting these band extrema by the formula[34]:

$$E(\mathbf{k}) = E(\mathbf{k_0}) \pm \frac{\hbar^2}{m_\parallel^*}(\mathbf{k_0} - \mathbf{k}_\parallel)^2 \pm \frac{\hbar^2}{m_\perp^*}(\mathbf{k_0} - \mathbf{k}_\perp)^2 \quad (10)$$

The ± is + for the conduction band and – for the valence band. $\mathbf{k_0}$ is the vector of the reciprocal space where the band is at its extremum. The symbols ∥ and ⊥ refer to the longitudinal and perpendicular axes that depend on the crystals structure. The effective masses were obtained by fitting the bottom of the conduction band (for the electron effective mass) and the top of the valence band (for the hole effective mass) with a parabolic function.

It is some times difficult to find the "good" crystallographic direction for the effective mass calculation, or sometimes, there are several bands extrema close in energy. In these specific cases, the effective masses can be computed using Boltzmann transport theory[45] with the equation 11 where σ is the conductivity of the material, τ collision time. It corresponds to an effective mass averaged on the density of state of the conduction band and the valence band.

$$\mathbf{m}^* = \frac{\sigma}{e^2\tau} \quad (11)$$

Exciton binding energy. If the exciton is delocalized on several unit cells, it can be treated as a hydrogen atom (the hole being the proton). This model is called the Wannier exciton.[37] In that model, the energy of the 1S state of the exciton is the binding energy of the exciton, $\mathbf{E_b}$, and it can be computed with the formula[55]:

$$\mathbf{E_b} = -E_H \frac{\mu}{\varepsilon_r^2} \quad (12)$$

E_H is the energy of the 1s orbital of hydrogen (-13.6 eV) and μ is the reduced mass of the exciton.

$$\frac{1}{\mu} = \frac{1}{m_e^*} + \frac{1}{m_h^*} \quad (13)$$

If the exciton has a localized behavior, like in the Frenkel's exciton or in molecular crystals, the Wannier's model is no longer relevant. More accurate approaches must be used to evaluate exciton binding energy. Nevertheless, the Wannier model, as we will see, gives a good idea the order of magnitude of the exciton binding energy.

II.2 Computational details

Codes. I used CRYSTAL[46] and VASP[47–49] codes to perform these calculations. CRYSTAL uses localized Gaussian Type Orbitals, thus treating quickly the exchange integrals during the SCF procedures making the use of hybrid functionals relatively fast. VASP has the advantage to have implemented the spin-orbit coupling using the non-collinear formalism that is necessary when dealing with heavy elements, like bismuth.

Functionals. The most accurate functional to simulate semiconductor bandgap is the subject of some benchmarks frequently found in the literature.[50–52] While the behavior of GGA, under-estimating band-gaps, or global hybrid, over-estimating them, is well documented now, it is not the case for the other semiconductor properties discussed here. This is the reason why I tested some functionals on the computation of properties on a list of semiconductors selected because of their use in photovoltaic and photocatalysis. I didn't tested all the functionals available in the literature but only a few of them because they are frequently used in solid state chemistry to computed electronic structures: PBE[53] (GGA), B3LYP (global hybrid, 20% of exact exchange), PBE0 (global hybrid, 25% of exact exchange) and HSE06[54,55] (range separated hybrid). The results and the conclusion of this benchmark are presented in the next section.

Basis set. For calculations with CRSYTAL code, I used split-valence basis sets with, at least, a double-zeta size always with polarization functions. For heavy atoms, like Bi, I used

pseudo-potentials proposed on the CRYSTAL website. With VASP code, I worked in the Projected Augmented Plane Waves (PAW) approach, using standard pseudopotential. The basis set size (i.e. the cut-off energy) was chosen as the one suggested in the pseudo-potential.

Other Parameters. k-points mesh was always selected based on a convergence test of the total energy of the system. For calculations involving hybrid functionals with VASP, the NKRED keyword was used to compute the exact exchange on a smaller number of k-points. The exact exchange energy was then interpolated on the other k-points.

II.3. Benchmark result and discussion

The table 3 summarizes the semiconductor selected for the benchmark and their tabulated properties.[56]

Compound	Structure	E_g	ε_r	m_e^*	m_h^*	E_b
C	diamond	5.50 (i)	5.7	1.4 (⊥) 0.36 (∥)	0.75	80-190
Si	diamond	1.17 (i)	12.1	0.19 (⊥) 0.92 (∥)	0.54 (h) 0.15 (l)	15
Ge	diamond	0.74 (i)	16-16.5	0.08 (⊥) 1.57 (∥)	0.04 (⊥) 0.28 (∥)	4
CdO	rocksalt	1.10 (i)	18.9	0.21	--	--
CdS	wurtzite	2.48 (d)	8.3 (⊥) 8.7 (∥)	0.25	0.7 (⊥) 5 (∥)	27
CdSe	wurtzite	1.73 (d)	9.1 (⊥) 9.3 (∥)	0.11	0.45 (⊥) > 1 (∥)	15
CdTe	zincblende	1.47 (d)	10.4	0.09	0.12 (l) 0.81 (h)	10
GaAs	zincblende	1.52 (d)	12.9	0.07	0.55 (h) 0.08 (l)	5
TiO_2-A	anatase	3.2 (i)	45.1 (⊥) 22.7 (∥)	--	--	--
TiO_2-R	rutile	3.0 (d)	110 (⊥ 260 (∥)	--	--	10-20
ZnO	wurtzite	3.4 (d)	7.8 (⊥) 8.7 (∥)	0.28	0.59	60

Table 3. Properties of the selected semiconductors. E_g is the bandgap (in eV), (d) and (i) mean direct and indirect bandgap respectively. ε_r is the total dielectric constant. m_e^* and m_h^* are the electron and hole effective masses respectively (given in electron mass). The symbols ⊥ and ∥ mean transverse and longitudinal directions respectively while (h) and (l) for the hole mean heavy and light. E_b is the exciton binding energy (in meV). The -- symbol means that no data or reliable data were found. From ref 56

The accuracy of each functional for each property is presented in the Figure 12. Only the Mean Absolute Error (MAE) is given, the comparison for each semiconductor is given in the main article Ref 53. The experimental data for the effective masses suffers from an important uncertainty and the values can change from one data series to another. For example, for the light hole effective mass in CdTe, values can go from 0.12 to 0.35.[57,58] This discrepancy is

related to the difficulty to obtain experimentally the effective masses. For that reason, the mean absolute error (MAE) between theory and experiment are not calculated for this property. But the computed values for this specific property are always in the same order of magnitude with respect to experiment.

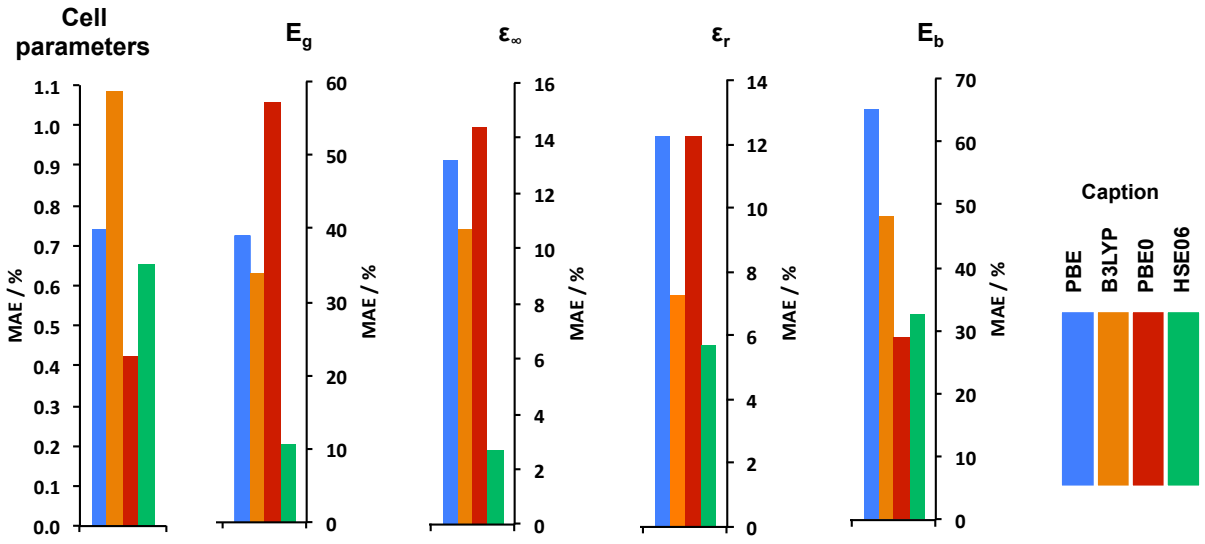

Figure 12. Mean Absolute Error of the four investigated functionals on the selected properties. Adapted with permission from "Le Bahers, T.; Rérat, M.; Sautet, P. *J. Phys. Chem. C* 2014, *118*, 5997" Copyright (2018) American Chemical Society.

It can be clearly extracted from these results that HSE06 out-performs all the investigated functionals for $\mathbf{E_g}$, $\boldsymbol{\varepsilon_\infty}$ and $\boldsymbol{\varepsilon_r}$ leading to errors below 10% for all these properties. This functional gives $\mathbf{E_b}$ values slightly worst than PBE0. It is surprinsing to see that PBE0, that gives the worst $\boldsymbol{\varepsilon_r}$**,** leads to the best estimation of $\mathbf{E_b}$ (whose calculation depends deeply on $\boldsymbol{\varepsilon_r}$). It is probably due to error cancellation when using the Wannier model to compute $\mathbf{E_b}$ compared to experimental exciton binding energy. Anyway, HSE06 is clearly the best compromise to compute electronic structures and related properties of these systems. For the cell parameters, PBE0 offers notably a better agreement with the experiment.

The very good performance of HSE06 is not a big surprise. This functional was designed for solid-state calculations. This is a range-separated hybrid, meaning that the exact – exchange (or Hartree-Fock exchange) depends on the interelectronic distance in the evaluation of the exchange integrals, in opposition to global hybrid, like PBE0 and B3LYP functionals, whose exact exchange is constant (Figure 13). But contrary to the well-known range-separated hybrids like cam-B3LYP[59] designed to increase the HF exchange when increasing the interelectronic distance, the HSE06 functional decreases this fraction (See Figure 13). The reason beyond this behavior is not physical but practical. Decreasing the HF exchange with

the distance allows to reduce the number of exchange integrals to compute on long-range that save a large amount of computational time in solid-state calculation.[54] The parameters governing the variation of HF exchange were fitted to reproduce the bandgap of several semiconductors.[54] We understand now why HSE06 works so well. It was designed for that purpose.

The development of new functionals for solid-state simulation and more precisely, for semiconductor properties calculations is still a topic of development. Some groups use global hybrid functionals, but changing the HF fraction for each semiconductor, assuming that a good HF fraction is equal to $1/\varepsilon_\infty$.[60–62] This approach works relatively well, but is not very elegant because we need to change the functional when changing the system that makes the comparisons difficult. New functionals are some times presented with better performance than HSE06.[63,64] But HSE06 gives errors on electronic properties below 10%. A better precision is, actually, not necessary for the investigations I perform daily. And, as we will see in the examples presented after, the HSE06 precision is good enough to interpret and understand experimental results.

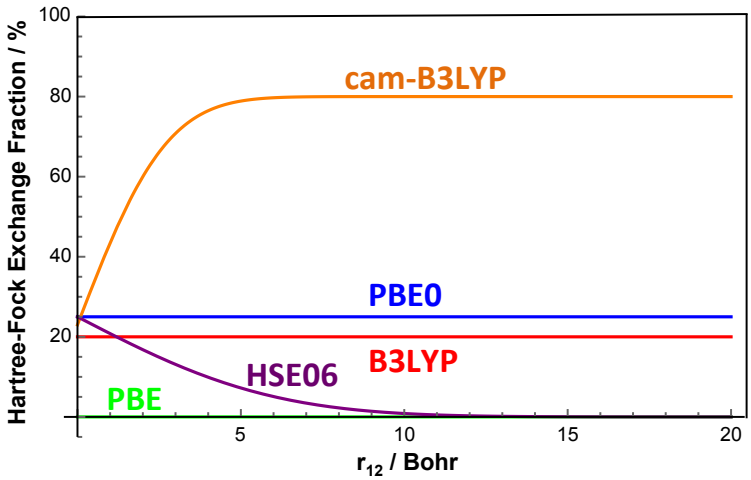

Figure 13. Fraction of exact exchange as a function of the interelectronic distance for several functionals.

From now on, all the calculations performed to simulate semiconductor properties are done by using PBE0 for geometry optimizations and HSE06 as single point calculations for electronic properties. As a matter of fact, to prove the reliability of this computational methodology, the electronic structure computed by this approach is presented for the $CuInS_2$ material and compared to experimental values in Figure 14.

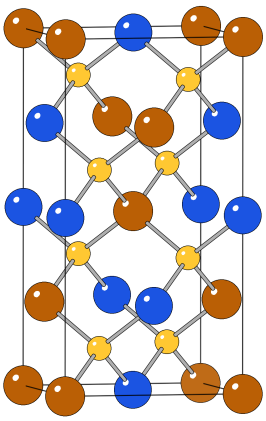

	Exp	DFT
E_g / eV	1.54(d) (T=300K) 1.62(d) (T=0K)	1.69(d)
ε_∞	6.2(⊥)6.0(∥)	6.6(⊥) 6.5(∥)
ε_r	8.6(⊥) 8.4(∥)	8.6(⊥) 9.1(∥)
m_e^* / m_e	0.16	0.21(⊥) 0.19(∥)
m_h^* / m_e	1.30	0.90(⊥) 0.25(∥)
E_b / meV	20	25

Figure 14: Experimental and computed properties of $CuInS_2$ with HSE06. Adapted with permission from "Le Bahers, T.; Haller, S.; Le Mercier, T.; Barboux, P. *J. Phys. Chem. C* 2015, *119*, 17585" Copyright (2018) American Chemical Society

The two next sections are dedicated to the investigation of BiCuOS based materials and carbonitrides (C_3N_4) for photocatalytic applications.

III. The example of the BiCuOS family

Related Articles:

- T. Le Bahers, S. Haller, T. Le Mercier, P. Barboux, *J. Phys. Chem. C,* **2015***, 119,* 17585.
- S. Lardhi, A. Curutchet, L. Cavallo, M. Harb. T. Le Bahers, *Phys. Chem. Chem. Phys.* **2017**, *19*, 12321.
- A. BaQuais, A. Curutuchet. A. Ziani, H. A. Ahsaine, P. Sautet, K. Takanabe, T. Le Bahers, *Chem. Mater.* **2017**, *29*, 8679.

I started to investigate BiCuOS during my post-doctoral position in the Solvay chemical company. The work on BiCuOS is done in collaboration with Solvay (Dr. Thierry Le Mercier) and ChimieParistech (Pr. Philippe Barboux). The work on Rare-Earth doped BiCuOS and BiAgOS is in collaboration with King Abdullah University of Science and Technology (KAUST, Saudi Arabia) with Pr. Kazuhiro Takanabe and Dr. Moussab Harb.

III.1 Presentation of the parent compound BiCuOS

The reason to work on the BiCuOS structure lies on its attractive bandgap, around 1.1 eV.[65] It was first synthesized in 1994 by Kusainova *et al.* using solid state reactions[66] and received a renewed interest when Sheets *et al.* proposed an alternative low temperature route through hydrothermal synthesis[67]. However, the first works made on the BiCuOCh family (Ch = S, Se and Te) were focused on their thermoelectric behavior.[68–70] For that application, BiCuOSe and BiCuOTe are more interesting than BiCuOS. Because no systematic electronic structure

calculations were performed on these minerals, we decided to investigate them to check if they fulfill the requirements presented in Table 2 for photovoltaic and photocatalytic devices. The structure of BiCuOS is presented in the Figure 15 along with the computed electronic properties. Its crystal structure belongs to the tetragonal system with the P*4/nmm* space group, made of a stacking of BiO and CuS layers. As we can see in Figure 15, few electronic properties are known about this material and DFT calculations completed its characterization. It clearly appears that BiCuOS is a very interesting candidate for photocatalysis with very high dielectric constant and very low effective masses. The high $\boldsymbol{\varepsilon_\infty}$ is mainly due to the very polarizable Bi atom while the large vibrational contribution is due to ionicity of the system brought by oxygen. The small hole effective mass (in the intralayer direction), is the consequence of a good valence band dispersion, made of the combination of S 3p orbitals and Cu 3d orbitals (Figure 16b). In other words, the good transport properties of this material is the consequence of the covalent bond between Cu(I) and S(-II) species.

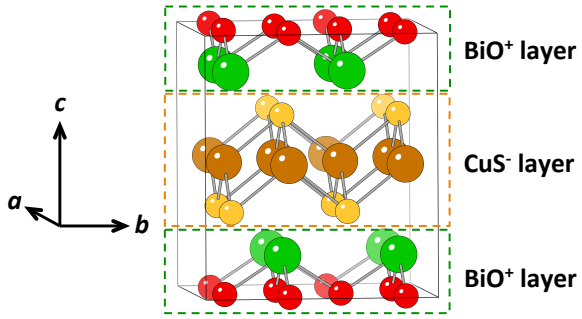

	Exp	DFT
$\mathbf{E_g}$ / eV	1.1	1.22(i) 1.46(d)
$\boldsymbol{\varepsilon_\infty}$	--	10.0(⊥) 7.5(∥)
$\boldsymbol{\varepsilon_r}$	--	56.7(⊥) 23.5(∥)
m_e^* / m_e	--	0.42(⊥) 0.68(∥)
m_h^* / m_e	--	0.33(⊥) 1.36(∥)
$\mathbf{E_b}$ / meV	--	2

Figure 15. Unit cell of BiCuOS and its electronic properties both experimental and computed. Green, yellow, red and brown atoms correspond to Bi, S, O and Cu atoms respectively. Adapted with permission from "Le Bahers, T.; Haller, S.; Le Mercier, T.; Barboux, P. *J. Phys. Chem. C* 2015, *119*, 17585" Copyright (2018) American Chemical Society

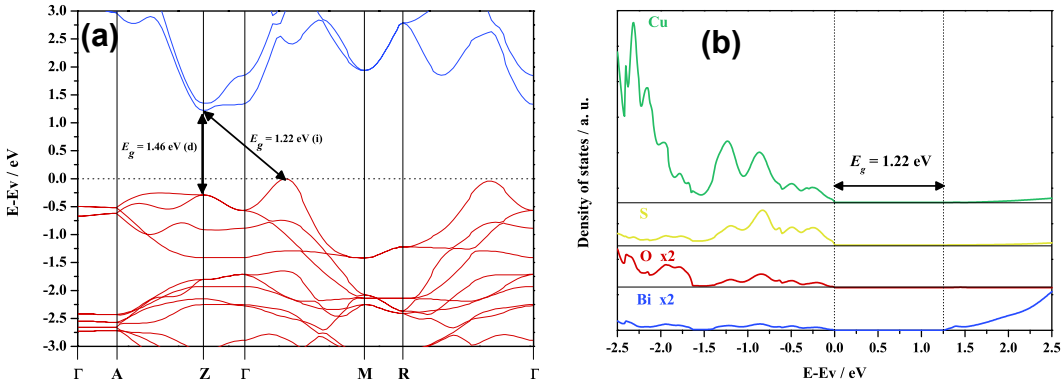

Figure 16. (a) band structure of BiCuOS. (b) Density of states of BiCuOS. Adapted with permission from "Le Bahers, T.; Haller, S.; Le Mercier, T.; Barboux, P. *J. Phys. Chem. C* 2015, *119*, 17585" Copyright (2018) American Chemical Society

Unfortunately, BiCuOS has not only good electronic properties. Among the drawbacks, we can cite the bandgap that is too small for water splitting (but acceptable for photovoltaic application), the indirect nature of the bandgap (Figure 16a) that reduces the absorption coefficient and finally the intrinsic p-type doping. All experimental characterizations of BiCuOS reported Cu(I) vacancies created in a large amount, leading to the global formula $BiCu_{0.94}OS$.[71–73] The low formation energy of Cu(I) vacancies is well-documented in the literature for several Cu(I)-based semiconductors. But what is surprising for BiCuOS, is that whatever the synthesis route used, the final formula is always very close to $BiCu_{0.94}OS$. Thus 6% of Cu(I) vacancies seems a thermodynamic condition to the stability of BiCuOS. These vacancies lead to a p-type doping to the material and with 6% of vacancies the semiconductor has metallic behaviour, as highlighted by the resistivity vs temperature curves.[72] The tuning of the p-doping fraction is the main experimental challenge of BiCuOS.

To prove that our results can be useful in the design of photo-responsive devices, we simulated a p-n junction of BiCuOS as p-type semiconductor and tried several wide bandgap n-type semiconductors. The objective was to simulate the J-V photovoltaic characteristics of such devices to find the most adapted n-type semiconductor to build the junction. The model was a simple 1D junction, simulated by the semi-classical semiconductors equations with the code SCAPS.[74] These equations, to be solved, need as input the semiconductor properties presented in Table 2 confirming the necessity to know these characteristics. The cell architecture and photovoltaic characteristics are given in Figure 17. It clearly appears that ZnO and TiO_2 are the best candidates to create a p-n junction with BiCuOS for photovoltaic application.

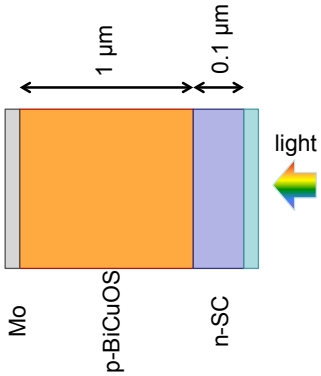

	ZnO	TiO_2 Anatase	TiO_2 Rutile	CdO	SnO_2	ZnS	CdS
V_{oc} / V	0.74	0.74	0.75	0.79	0.75	0.74	0.74
J_{sc} / mA.cm^{-2}	29.6	30.5	29.6	11.7	30.0	30.9	26.8
FF / %	82.3	82.6	66.3	20.8	57.0	69.3	83.2
η / %	18.3	18.8	14.7	1.9	12.8	15.9	16.6

Figure 17. Structure of the p-n junction simulated and computed photovoltaic characteristics for various n-type semiconductors. Adapted with permission from "Le Bahers, T.; Haller, S.; Le Mercier, T.; Barboux, P. *J. Phys. Chem. C* 2015, *119*, 17585" Copyright (2018) American Chemical Society

But photovoltaic application is not my objective. The world is already full of very interesting semiconductors for photovoltaic technologies. We need to move to water splitting. For that application, we need to increase the bandgap of BiCuOS. Two strategies were tested: The first one by substituting Bi with rare earth elements to increase the energy of the bottom of conduction band and the second by replacing Cu with Ag, to decrease the top of valence band.

III.2 Rare earth (RE) doped BiCuOS

RECuOS (RE=La, Ce, Pr, Nd) materials are already synthetized and presented in the literature.[75,76] They crystallize in the same structure as BiCuOS (Figure 15) where RE(+III) replaces Bi(+III), but they have much larger bandgaps, around 3 eV or higher. For that reason, they were first investigated in the literature for p-type Transparent Conductive Oxide. But in our case, we simulated the solid solution $Bi_{1-x}RE_xCuOS$. We assumed that, because they have the same crystal structure, the same oxidation state and the same ionic radius, Bi and RE could form a solid solution. We tried only some RE elements whose f-orbitals doesn't contribute to the frontier orbitals avoiding the creation of localized states in the gap that can play as recombination centers. At +III oxidation state, La and Lu have empty and full occupied f-orbitals respectively, so these orbitals don't contribute to the frontier orbitals. Y was also selected, although it is not a lanthanide, but it belongs to the family of RE elements and has no f-orbitals. Finally, Gd was also chosen since the first f–f transition of the Gd(+III) ion is higher than 3.8 eV, and so is notably higher than the targeted bandgap.

The doping fractions, x, investigated were 0.0, 12.5, 25.0, 37.5, 50.0, 62.5, 75.0, 87.5 and 100% in a 2x2x1 supercell. For each doping fraction, all possible doping conformations were simulated. We computed the stability of the solid solution with respect to the stable BiCuOS and RECuOS pure compounds. Then all the relevant electronic properties were computed.

The main conclusions are:

1- Only solid solutions between Bi and La are particularly stable, probably because they have very close ionic radius while Gd(+III), Y(+III) and Lu(+III) are notably smaller.

2- The solid solution $Bi_{1-x}La_xCuOS$ has a bandgap evolving smoothly between pure BiCuOS and LaCuOS leading to $\mathbf{E_g}$ values of 2.0-2.5 eV for x values between around 37.5% and 62.5 % (Figure 18a). For the other dopant, the $\mathbf{E_g}$ variation is more abrupt with a BiCuOS bandgap for x<50% and a bandgap going quickly to the one of pure RECuOS for higher x (Figure 18b)

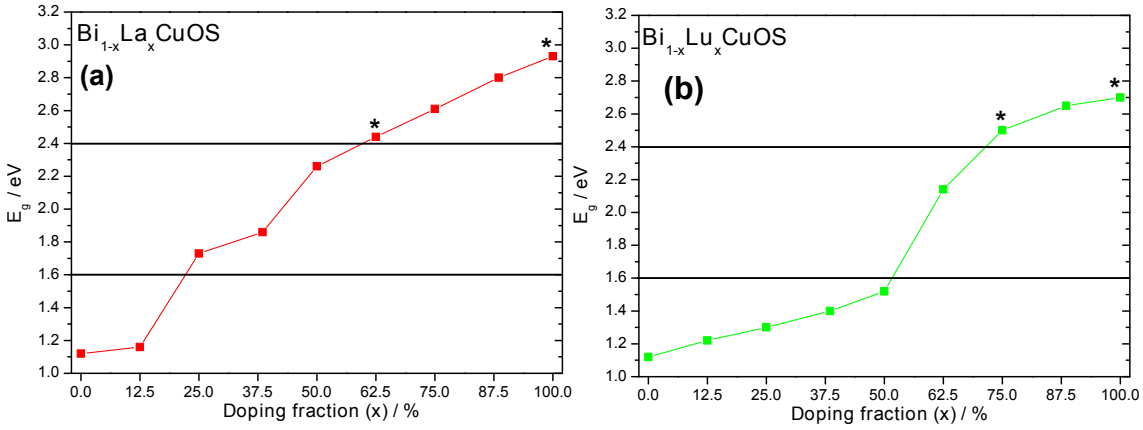

Figure 18. Variation of the bandgap as a function of the rare earth content for La (a) and Lu (b) dopants. All bandgaps are indirect except the ones marked by an asterisk.

3- For the other properties (ε_∞, **m***), they are interesting only for the highest Bi content system (i.e. low x value). Interestingly, for very small doping (x=12.5%), whatever the RE element, the effective masses reduce that is explained by some geometrical modifications. This surprising phenomenon is confirmed experimentally by La doped BiCuOSe for small doping fraction.[77,78]

In conclusion, while doping of BiCuOS with lanthanum seems thermodynamically possible, a compromise must be found for the doping fraction: close to 50% to have a good bandgap or as low as possible to have high dielectric constant, small effective masses and exciton binding energies.

III.3 Properties of BiAgOS

The other strategy to tune the bandgap of BiCuOS, is to change the valence band position. We investigated this possibility by completely replacing Cu(I) by Ag(I) since 4d levels of Ag(I) are lower in energy than 3d Cu(I). Contrary to the previous work on rare earth element, this work is a combined theoretical and experimental investigation in collaboration with the group of Pr. Takanabe in KAUST.

The synthesis of both BiAgOS and BiCuOS was performed with a hydrothermal route. The analysis of X-ray pattern of BiAgOS confirmed that BiCuOS and BiAgOS have the same crystal structure. UV-Vis reflectance spectra recorded for both compounds shows that the bandgap of BiAgOS (1.5 eV) is larger than the one of BiCuOS (1.1 eV). The XPS analysis of these compounds revealed that BiCuOS is under-stoichiometric with respect to copper, as expected. Interestingly, the same analysis on BiAgOS didn't reveal any Ag vacancies formation. A very recent article has been published by another group on BiAgOS.[79] They

performed a very fine analysis of BiAgOS structure based on synchrotron radiation. They revealed that Ag vacancies are present in the material but at a much lower concentration compared to BiCuOS leading to a clear semiconductor behaviour in term of electronic conductivity. Finally, we determined the band positions (valence and conduction) by Mott-Shottky and photoelectron spectroscopy measurements.

DFT calculations completed these experimental characterizations. Theoretical calculations confirmed the experimental bandgaps. Furthermore, it appeared that the substitution of Cu by Ag improved the electronic properties (dielectric constant and effective masses). The density of state analysis indicated that the Ag 4d and S 3p contributions to the valence band are clearly separated while the valence band BiCuOS is a mixing of Cu 3d and S 3p orbitals. Fortunately, this change in the valence band composition didn't affect the hole effective mass, remaining relatively low. All these considerations are presented in the Figure 19.

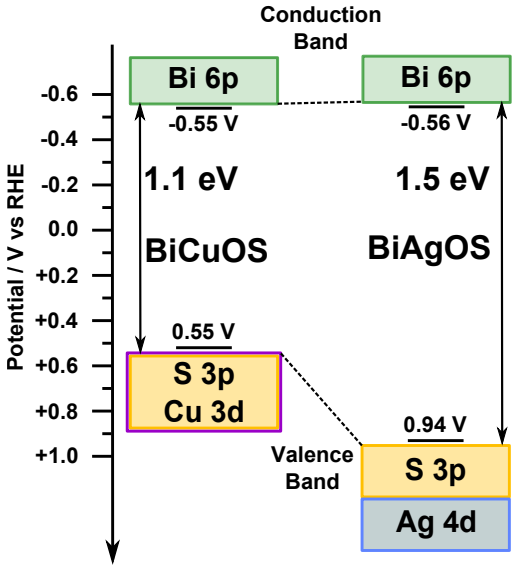

	BiCuOS		BiAgOS	
	Exp	DFT	Exp	DFT
E_g / eV	1.15	1.22	1.50	1.42
ε_∞	--	10.0 ∥ 7.5 ⊥	--	9.8 ∥ 8.7 ⊥
ε_r	--	56.7 ∥ 23.5 ⊥	--	119.7 ∥ 23.7 ⊥
m_e^* / m_e	--	0.42 ∥ 0.68 ⊥	--	0.23 ∥ 0.30 ⊥
m_h^* / m_e	--	0.33 ∥ 1.36 ⊥	--	0.45 ∥ 0.78 ⊥
E_b / meV	--	2.0	--	0.4
VB / eV vs vac.	−4.97 (MS) −4.88 (P)	--	−5.30 (MS) −5.34 (P)	--
CB / eV vs vac.	−3.82 (MS) −3.73 (P)	--	−3.80 (MS) −3.84 (P)	--

Figure 19. Electronic structure of BiAgOS and BiCuOS along with computed and measured properties for these two materials. Adapted with permission from "BaQuais, A. *et al. Chem. Mater.* 2017, *29*, 8679" Copyright (2018) American Chemical Society

Combining all these information together, we can conclude that:

1- We succeeded to increase the bandgap of BiCuOS by replacing Cu with Ag. This E_g increase is due to a valence band energy decrease.

2- The good electronic properties of BiCuOS are also recovered in BiAgOS, even slightly improved.

3- Unfortunately, the bandgap of BiAgOS (1.5 eV) is still too small to consider this material for overall water splitting. Looking at the band positions with respected to the

reversible hydrogen electrode (Figure 19), we can see that the HER is possible since the bottom of conduction band is lower in potential than 0.0 V (vs RHE) but the OER is not possible since the top of valence band is lower than 1.23 V (vs RHE). The conclusion is confirmed by experiments since we succeeded to evolve H_2 (using a sacrificial reagent) with BiAgOS while we didn't succeed to observe any O_2 evolution.

To conclude on the BiCuOS family, our investigations clearly highlighted that these materials have some potentialities in photocatalysis. They can be easily doped and we can easily perform solid solutions to tune their electronic properties. From an experimental point of view, the possibility to use several synthesis routes to obtain the BiCuOS structure offers to the experimentalists many ways to adapt the BiCuOS composition and morphology. Nevertheless, beyond these positive points, we have to admit that for the water splitting issue, the bandgap of this family of material is still relatively low and this family is not the best candidate for single-semiconductor overall water splitting catalyst. But for double-junction semiconductor catalyst, a 1.4-1.5 eV of bandgap (like for BiAgOS) is particularly interesting (see Figure 10b). Consequently, this semiconductor family could be an interesting candidate for this type of photocatalytic devices.

IV. The carbonitrides

Related Articles:

- M. K. Bhunia, S. Melissen, M. R. Parida, P. Sarawade, J.-M. Basset, D. H. Anjum, O. F. Mohammed, P. Sautet, T. Le Bahers, K. Takanabe, *Chem. Mater.* **2015**, *27*, 8237.
- S. Melissen, T. Le Bahers, S. Steinmann, P. Sautet, *J. Phys. Chem. C* **2015**, *119*, 25188.
- S.T.A.G. Melissen, S.N. Steinmann, T. Le Bahers, P. Sautet, *J. Phys. Chem. C*, **2016**, *120*, 24542.
- S. N. Steinmann, S. T. A. G. Melissen, T. Le Bahers, P. Sautet, *J. Mater. Chem. A*, **2017**, 5115.

This work was initiated by the collaboration with Pr. Kazuhiro Takanabe (KAUST).

Contrary to the BiCuOS family that is poorly investigated in the literature, carbonitrides are much more studied.[80] These materials are based on the polymerization of triazine and heptazine tectons presented on Figure 20. The global formula of these materials is g-$C_xN_yH_z$ (g- stands for graphitic) with the *g*-C_3N_4 formula for a fully, perfectly polymerized carbonitride. Cabonitrides have a graphitic structure made of covalent layers of *g*-$C_xN_yH_z$

stacked by Van der Waals interactions. The development of these compounds surfs on the success of graphene based materials or more generally on 2D based materials. The are considered for classical catalysis[81,82], supercapacitor[83,84] (due to the high specific area of the layered structure), bio-imaging[85] and for what interests us, photocatalysis[86–88]. What makes these materials interesting for water splitting are:

1- A Bandgap measured around 2.7 eV, that can be tuned toward lower values by carbon doping;
2- Band positions adapted for overall water splitting (OER and HER);
3- Large specific area;
4- Easy of synthesis.

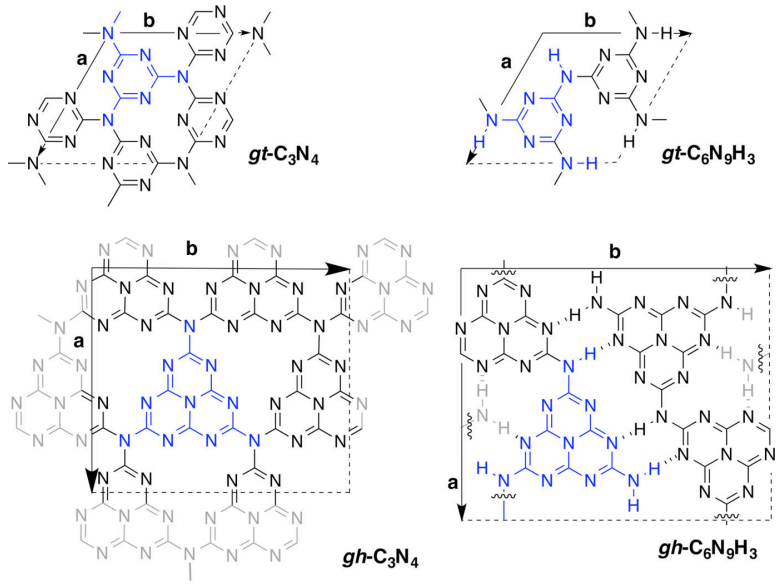

Figure 20. Structures of fully polymerized *g*-C_3N_4 (*gt*- for triazine based and *gh*- for heptazine based systems) along with examples of partially polymerized ones. Adapted with permission from "Melissen, S.T.A.G.; Le Bahers, T.; Steinmann, S.N.; Sautet, P. *J. Phys. Chem. C* 2015, *119*, 25188" Copyright (2018) American Chemical Society

Beyond this list of positive points, the electronic structure of these materials (in term of dielectric constant, effective masses…) is not very known. Actually, the crystal structure is also not perfectly solved. One main reason of the poor resolution of the crystal structure comes from the difficulty (and even the impossibility) to obtain, pure perfectly polymerized carbonitrides, with formula g-C_3N_4. The polymerization stops at a partial condensation, with global formula *g*-$C_xN_yH_z$, as the *g*-$C_6N_9H_3$ structure presented in Figure 20. This partial polymerization makes the experimental observations very dependent on the experimental conditions used for synthesis.

From that point, in collaboration with Pr. Takanabe, we investigated the properties of C_3N_4 to understand the consequence of the incomplete polymerization on the properties of this mineral and to find which one is the most important to improve to increase the efficiencies.

IV.1 Properties of C_3N_4 materials

Crystal structure of *g*-$C_xN_yH_z$. We first investigated the difference in geometry between the fully and partially polymerized carbonitrides, both based on triazine and heptazine tectons. From a technical point of view, we used the dispersion correction of Grimme and co-workers to simulated dispersive interaction (+D2 model).[89] The geometry optimizations of the fully polymerized structures lead to important corrugation while the covalent layers of the partially polymerized ones are almost flat (Figure 21). The reason of this corrugation is the large steric repulsion between the nitrogen lone pairs that is partially suppressed when monomer vacancies are present. We confirmed this larger stability of partial polymerization by thermodynamic calculations showing that the full polymerization is not stable both from the entropy and the enthalpy points of view.[90]

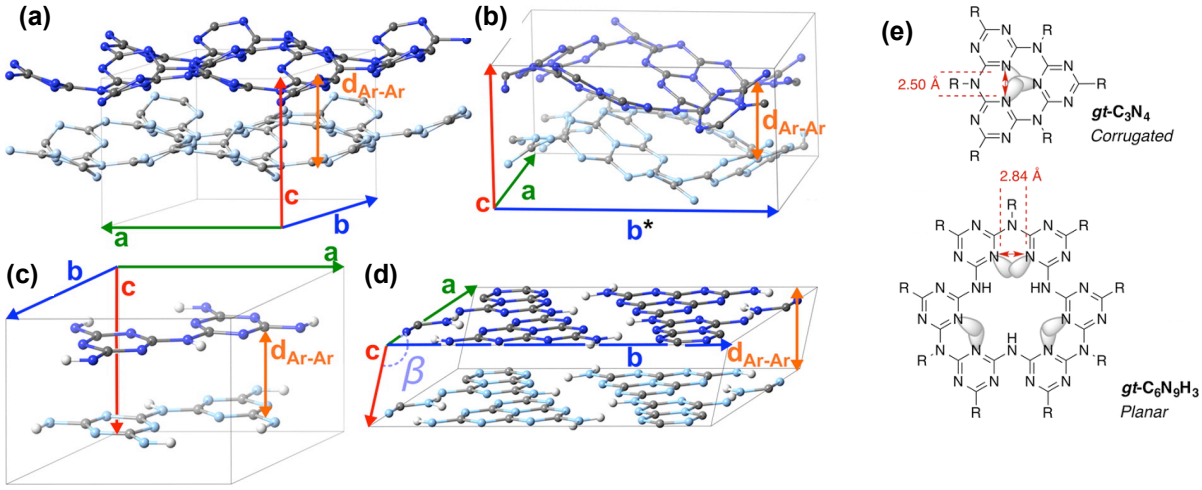

Figure 21. Optimized geometries of the fully polymerized gt-C_3N_4 (a) and gh-C_3N_4 (c), partially polymerized gt-$C_9N_6H_3$ (b) and gh-$C_9N_6H_3$ (d) and (e) scheme of the N lone pair repulsion. Adapted with permission from "Melissen, S.T.A.G.; Le Bahers, T.; Steinmann, S.N.; Sautet, P. *J. Phys. Chem. C* 2015, *119*, 25188" Copyright (2018) American Chemical Society

Electronic properties of these minerals. The list of electronic properties presented in the introduction of this chapter was computed for all these compounds. Because results on triazine and heptazine based carbonitrides are very similar, I am going to focus only on triazine based ones. For the C-doped carbonitrides, we replaced one N atom by a isovalent CH function. The results are presented in the Table 4. For exciton properties, we used the Wannier model and because the exciton binding energies were notably large, we used the

fomula (6) to estimate the optical bandgap from the mono-electronic one extracted from Kohn-Sham bands.

With carbonitrides, we are far from the electronic structure of the ideal semiconductor developed for water splitting. Even the ideal fully polymerized *gt*-C_3N_4 has very loose electronic properties such as a low dielectric constant, a large hole effective mass and a very important $\mathbf{E_b}$ (much larger than 25 meV). For the partially polymerized one (closer to the experimental system) it is worst and it is also worst on carbon-doped system investigated to reduce the bandgap. The only good point of this material family comes from the electron effective mass that is relatively low and an optical bandgap that is close to 2.5 eV. It is interesting to note that the very raw way to compute the optical bandgap leads to very reasonable values. Moreover, we reproduced the reduction of bandgap upon carbon doping.

	Fully polymerized *gt*-C_3N_4	Partially polymerized *gt*-C_3N_4 (*gt*-$C_6N_9H_3$)	C-doped *gt*-$C_6N_9H_3$
$\mathbf{E_g}$(mono) / eV	3.3	4.3	3.7
$\boldsymbol{\varepsilon_\infty}$ / --	5.0	3.4	(3.4)
$\boldsymbol{\varepsilon_r}$ / --	6.8	4.6	(4.6)
$\mathbf{m_e^*}$ ($\mathbf{m_h^*}$) / m_e	0.41 (1.40)	0.70 (1.90)	0.5 (2.5)
$\mathbf{E_b}$ / eV	367	1350	1180
$\mathbf{E_g}$(opt) / eV	3.0	3.0	2.6

Table 4. Computed electronic properties of several carbonitride based on triazine.

Looking at this table, we can understand that the main drawback of this family of material is the very large exciton binding energy. Carbonitrides behave like molecules more than a classical covalent solid with delocalized electrons. Once the photon absorbed, the exciton is almost never dissociated, and the energy is lost by recombination whether luminescent or not. Actually, this problem was encountered many years ago, by chemists and physics developing polymer based photovoltaic devices. And this problem was solved. The idea is to use not the bulk material to dissociate the exciton (because it cannot) but an interface between two materials. This lead to a new solar cell architecture favouring as much as possible the interfaces between two materials called bulk-heterojunction.[91] Such bulk-heterojunction architecture could be used to dissociate the exciton in carbonitrides. The interface for dissociating the exciton is between the carbonitride and the co-catalyst used for HER and/or OER. With this aim, the group of Pr. Takanabe performed the synthesis of carbon-doped *gt*-C_3N_4 (named PTI-0.15) on top of silica particles (KCC-1) or not. The HER experiment and TEM image of PTI-0.15/KCC-1 are presented in Figure 22. The main conclusions of these experiments are that HER efficiency is improved by carbon doping, mainly because of the

bandgap reduction, and that the morphology of the carbonitride as a large importance on the final efficiency (comparison of red and blue points on Figure 22a). This last observation is expected assuming that the interface is the place where stands the exciton dissociation.

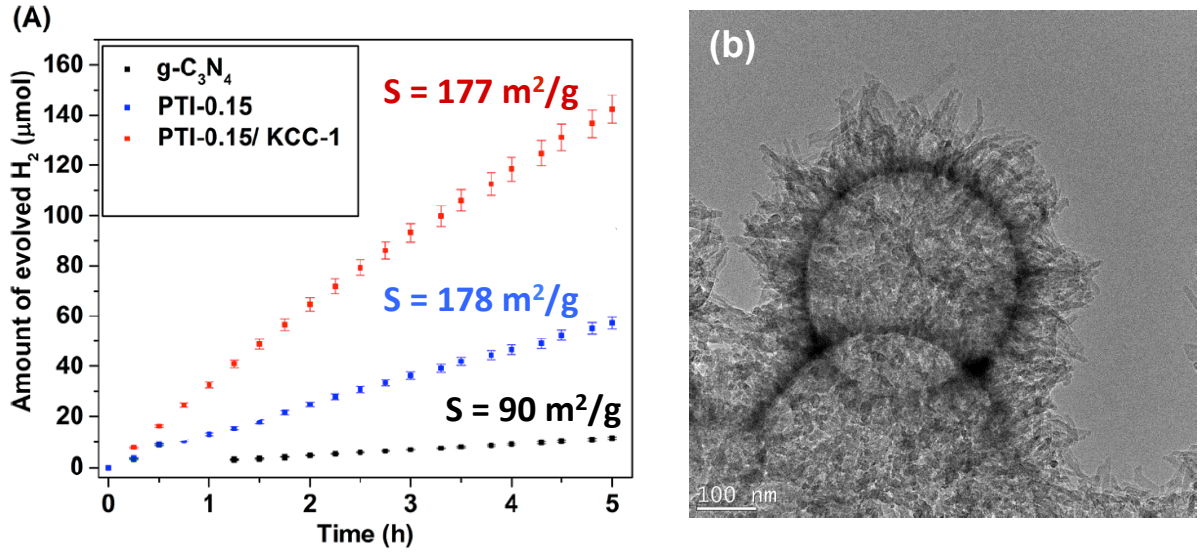

Figure 22. (a) HER experiment of several type of carbonitride. Pt as co-catalyst, 10% of triethanolamine as sacrificial reagent, Xe as light source with 385-740 nm filter. (b) TEM image of PTI-0.15/KCC-1. Adapted with permission from "Bhunia, M.K. *et al Chem. Mater.* 2015, 27, 8237" Copyright (2018) American Chemical Society

Beyond this joined theoretical and experimental work, we can wonder if the use of the Wannier is adapted. The exciton radius, computed with Wannier model, gives values in the range 1.8-3.6 Å depending on the carbonitride. The exciton is thus very localized and we are far from the approximation of an exciton so delocalized that it feels only an average dielectric constant. A better simulation of the exciton binding energy is the topic of the last paragraph.

IV.2 Beyond the Wannier model of the exciton

To understand the limit of the Wannier model, we performed the simulation of the exciton binding energy using a post-DFT approach based on the many body perturbation theory. The quasi-particle levels were obtained using the Green's function (noted G) and the screen Coulomb interaction (noted W) while the excitations were computed by solving the Bethe-Salpeter equation (BSE) within the Tamm-Dancoff approximation.[43,44] One cycle of GW calculation, using Kohn-Sham orbitals obtained by HSE06 functional is called G_0W_0 while partially self-consistent calculations and fully self-consistent calculations are named GW_0 and scGW respectively. BSE allows to compute the exciton binding energy in a more rigorous way, compared to the Wannier model, while it does not take into account any vibrational

contribution to the dielectric constant. For that reason, the comparison of the Wannier model and the BSE results was based on Wannier model involving the total dielectric constant (as in the other work) and only the electronic contribution, $\boldsymbol{\varepsilon}_{\infty}$. The results are presented in Figure 23.

In this study, we investigated two structures corresponding to the pure gt-C_3N_4 (corrugated), the partially polymerized gt-$C_6N_9H_3$ (flat) both in a bulk structure (i.e. with periodic stacking) or only 2 or 1 layers. The monoelectronic bandgaps were computed by DFT (PBE and HSE06 functional) and with various levels of post-DFT calculations. For the HSE06 and scGW calculations, the optical bandgap is also presented by subtracting $\mathbf{E_b}$ from the bandgap.

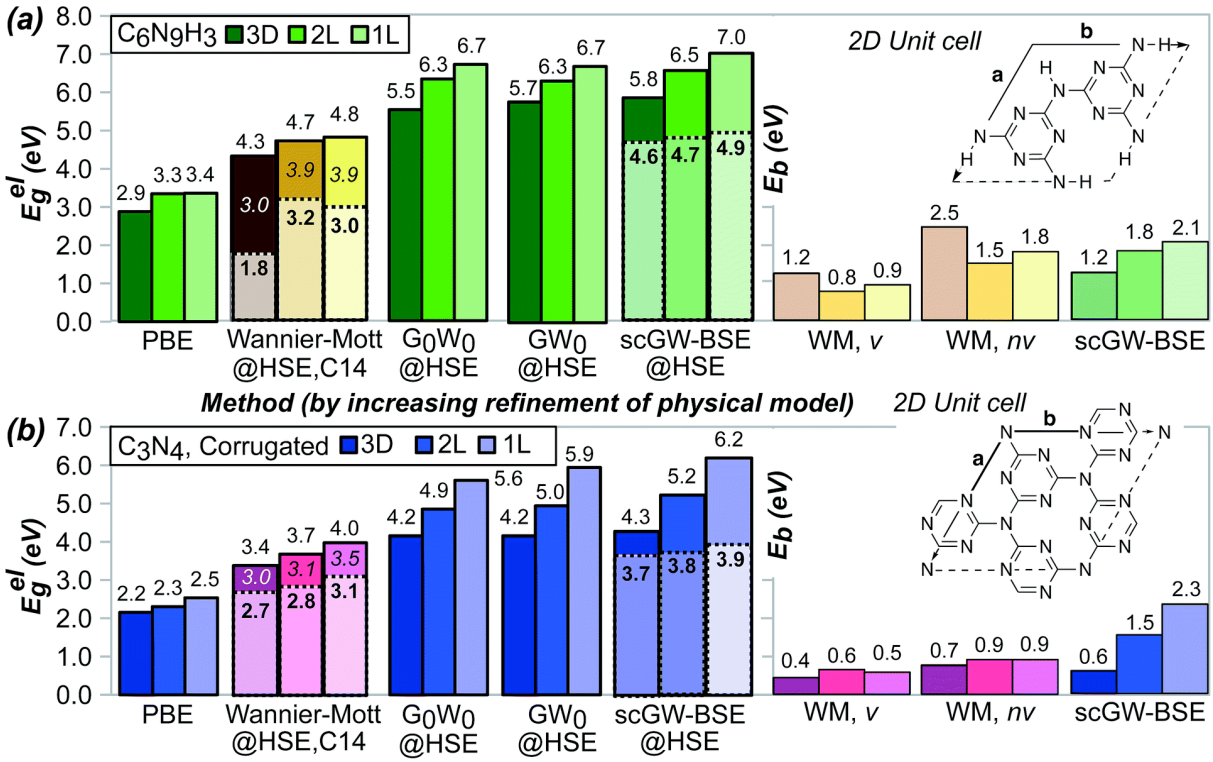

Figure 23 Summary of the results presented in this section. Electronic band gaps for (a) gt-$C_6N_9H_3$, (b) corrugated gt-C_3N_4 are reported. The Wannier–Mott analysis using the CRYSTAL14 code is depicted in an alternative color scheme. The optical band gaps $E^{opt,nv}_g$ are depicted semi-transparently. The E^{v}_b-corrected band gaps are provided in italics for completion. The WM and scGW-BSE exciton binding energies E_b are provided to the right of the band gaps, with v and nv denoting vibrationally and not vibrationally corrected, respectively. The 2D unit cells for the studied structures are given with lattice vectors a and b.

The main conclusions are the following ones:

1- The DFT, even with HSE06, under-estimate strongly the quasi-particle bandgap compared to scGW.

2- Going from G_0W_0 to scGW doesn't change so much the final bandgaps.

3- The exfoliation of g-C_3N_4 (i.e. going from bulk to monolayer) increases the bandgap.

4- The most accurate approach, scGW/BSE, overestimates the optical bandgap (3.7 eV computed vs 2.7 eV measured).
5- The $\mathbf{E_b}$ computed by the Wannier model are of the same order of magnitude as the BSE ones.

It is surprising to note that scGW/BSE and the Wannier model lead to the same order of magnitude of the exciton binding energy (with around a factor 2 of difference). Of course, for very accurate calculations, the Wannier model is not adapted. But, as we are more interested by the order of magnitude than the exact value, the Wannier model offers a fast way to evaluate $\mathbf{E_b}$.

Beyond the comparison between BSE and the Wannier model, this work asks some questions. It is surprising that the optical bandgap is overestimated by 1 eV compared to experiment, and maybe more because experimentally the composition is closer to $C_6N_9H_3$ than C_3N_4. We don't have clear explanation of this difference yet. This could be due to defects in the experimental compound, reducing the bandgap. But the nature of these defects is still unknown.

It is now time to give a conclusion on this section dedicated to carbonitrides. As we have seen, this family is very different from the BiCuOS one. Carbonitrides behave like polymer semiconductors, more than classical inorganic semiconductors. Their efficiencies in photocatalytic devices are completely governed by the exciton dissociation that demands a special care in the design of the architecture of the photocatalyst. Beyond this applied aspect, these materials were a very good test case for our approach developed to investigate more classical semiconductors. Finally, while not perfect, the key properties of the materials can still be computed at the DFT level, at least to have the order of magnitude of the properties.

V. Other semiconductors and concluding remarks

Related Articles:

- A. Ziani, C. Le Paven, L. Le Gendre, F. Marlec, R. Benzerga, F. Tessier, F. Cheviré, M. N. Hedhili, A. T. Garcia-Esperza, S. T. A. G. Melissen, P. Sautet, T. Le Bahers. K. Takanabe, *Chem. Mater.* **2017**, *19*, 3989.
- S. Petit, S.T.A.G. Melissen, L. Duclaux, M.T. Sougrati, T. Le Bahers, P. Sautet, D. Dambournet, O. Borkiewicz, C. Laberty-Robert, O. Durupthy, *J. Phys. Chem. C*, **2016**, *120*, 24121.
- T.A. Kandiel, D.H. Anjum, P. Sautet. T. Le Bahers, K. Takanabe, *J. Mater. Chem. A*, **2015**, 3, 8896.
- S.T.A.G. Melissen, F. Labat, P. Sautet, T. Le Bahers, *Phys. Chem. Chem. Phys.* **2015**, *17*, 2199.

This *ab initio* characterization of semiconductors was also performed occasionally on some other family of semiconductors. I can cite the work on $SrTaO_2N$, with the challenge to model the anion ordering, still in collaboration with Pr. Kazuhiro Takanabe (KAUST, Saudi Arabia).[92] This work confirmed, again, the reliability of the computational protocol developed to compute semiconductor properties.

But, to be more honest, some systems put us in troubles. For instance, in collaboration with Dr. Durupthy on Fe_2TiO_5, we faced the problem to simulate the bandgap of systems containing d-electrons. Unfortunately, even HSE06 doesn't reproduce well the energetic levels of these very correlated electrons leading to overestimation of the bandgaps.[93] Moreover, during the investigation of the family of material $PbX_3CH_3NH_3$ (X=Cl, Br and I) we also faced the problem of bandgaps reproduction. But, in that case, the bandgap (computed at the HSE06+Spin Orbit coupling level) was underestimated. $\mathbf{E_g}$ was successfully reproduced by scGW/BSE calculations, published by other groups, which highlighted the need to go to the many body perturbation theory to accurately describe this system.[94]

I demonstrated on several examples the necessity to characterize completely the bulk properties of semiconductors for photovoltaic and photocatalytic applications. Unless some specific cases, the protocol used works pretty well to reproduce the key properties. The development and the assessment of this protocol has been one my main works since 2012. But now, I consider this assessment period over. I am using this computational procedure routinely to characterize semiconductors on demand (via my collaborations) or to design semiconductors *in silico*.

VI. Beyond the semiconductors: The Oxygen Evolution Mechanism

Related Article:

- E. Nurlaela, H. Wang, T. Shinagawa, S. Flanagan, S. Ould-Chikh, M. Qureshi, Z. Mics, P. Sautet, T. Le Bahers, E. Cánovas, M. Bonn, K. Takanabe, *ACS Catalysis*, **2016**, *6*, 4117

The results discussed up to now correspond to the investigation of step 1 to step 3 in the Figure 9. My research objectives are to move to the study of other steps, in parallel, starting by the OER and HER mechanisms.

The development of OER co-catalyst is an important topic of research. The reason of this attractiveness is the lack of efficient OER co-catalyst. As we have discussed in Page 30, to perform an electrochemical reaction, we must apply at least the standard potential of the reaction (that is the thermodynamic condition) but in general an extra potential is added and this extra potential is called over-potential (noted η). The lower the overpotential, the better is the co-catalyst. For HER, it already exists co-catalyst working with almost no overpotential such as Pt, Rh or enzymes like hydrogenase. Of course these co-catalysts are expensive, but, at least, they exist. For OER, the best co-catalysts are RuO_2 or IrO_2 but they both have a not negligible overpotential (more than 0.3 V at 10 $mA.cm^{-2}$).[95] The difficulty to develop co-catalyst for this reaction comes from the larger complexity of the OER mechanism ($4e^-$ transferred) compared to HER ($2e^-$ transferred).

In collaboration with Pr. Kazuhiro Takanabe, we studied cobalt oxide based co-catalyst (with the general notation CoO_x) doped by Rh and Ru.[96] Nickel and cobalt oxides are known to be efficient OER co-catalysts. Very recent works, experimental and theoretical, have proved that the active phase for these catalysts are NiOOH and CoOOH (called nickel and cobalt oxide-hydroxide) both having Ni(+III) and Co(+III) oxidation state.[97,98]

For this work, we used the so-called Nørskov approach to simulate the overpotential of the reaction.[98] The overpotential has mainly two origins, kinetic barriers (related to transition state energies) and thermodynamic barriers (related to the stability of the intermediates). For OER on CoO_x, the intermediate species are believed to be adsorbed O, OH and OOH groups on a surface vacancy (noted *). The following equation resume the elementary steps of the OER:

$$H_2O + * \rightarrow {}^*OH + H^+ + e^- \quad (14)$$
$${}^*OH \rightarrow {}^*O + H^+ + e^- \quad (15)$$
$${}^*O + H_2O \rightarrow {}^*OOH + H^+ + e^- \quad (16)$$
$${}^*OOH \rightarrow * + O_2 + H^+ + e^- \quad (17)$$

The free energy associate to these steps is defined as:

$$\Delta G_1 = \Delta G_{OH} - eU - k_B T \ln(10) pH \quad (18)$$
$$\Delta G_2 = \Delta G_O - \Delta G_{OH} - eU - k_B T \ln(10) pH \quad (19)$$
$$\Delta G_3 = \Delta G_{OOH} - \Delta G_O - eU - k_B T \ln(10) pH \quad (20)$$
$$\Delta G_4 = 4.92 - \Delta G_{OOH} - eU - k_B T \ln(10) pH \quad (21)$$

where U is the potential of the NHE. The sum of the four reaction free energies is equal to 4.92 eV that corresponds to the four-electron transfer at 1.23 V. The free energies of the reactions (18)-(21) allows to estimate the thermodynamics overpotential:

$$\eta(V) = \frac{\max\{\Delta G_i\}}{e} - 1.23 \quad (22)$$

The system was modelled by the hydrated (10-14) surface of CoOOH (that is the most stable one).[98] The Ru and Rh doping was modelled by substituting one Co by one dopant, and one H atom was removed to adapt to the oxidation state of the dopant. For doped system, the OER mechanism was computed both on top of the Ru/Rh atom and on top of the closest Co atom from the dopant.

In term of computational methodology, these calculations were performed with the VASP code. The GGA exchange-correlation functional PBE was used. Cobalt oxides are known to be strongly correlated materials. Even hybrid functionals that are popular for semiconductors fail to reproduce the electronic structure of this family of compounds.[99] For that reason, the Hubbard hamiltonian (noted +U) was added in the calculations. This approach has proven its reliability for several metal oxides including cobalt oxides.[98–101] More precisely, the formalism proposed by Duradev *et al*. was used along with the following U-J values: 3.5 eV for Co, 3.0 eV for Ru and 3.3 eV for Rh.

Experimentally, these co-catalysts were tested both in photocatalysis and electrocatalysis. The I-V curve associated to electrocatalysis is presented in Figure 24 along with the computed intermediates for the DFT part.

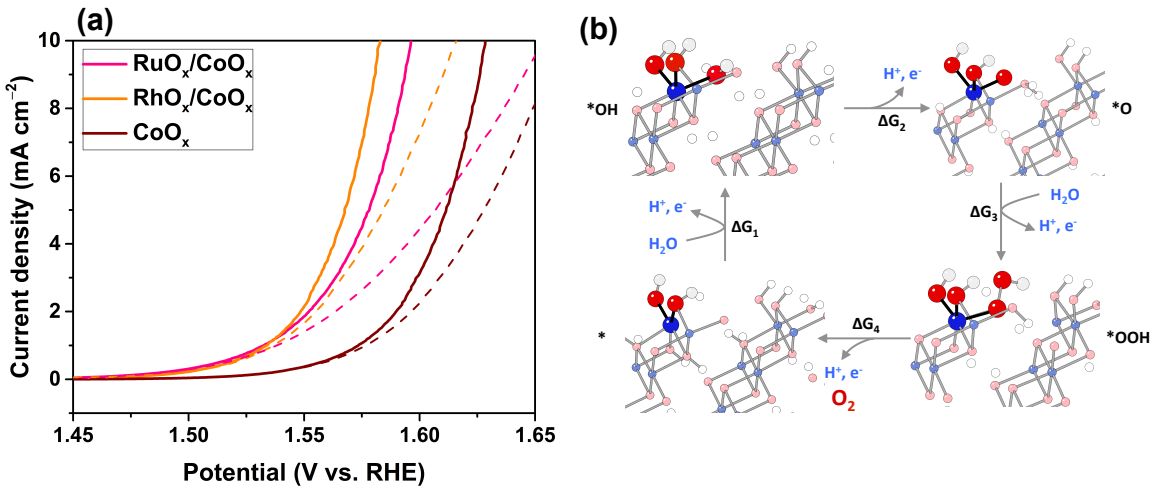

Figure 24. (a) Linear-sweep voltammograms over various electrodes: RhO_x/CoO_x, RuO_x/CoO_x, CoO_x. Measurements were carried −1 mV s^{-1} scan rate. Solid line: with *iR* correction. Dotted line: without *iR* correction. (b) Scheme of surface intermediates along the four elementary steps for oxygen evolution reaction; Adapted with permission from "Nurlaela, E. *et al ACS Catal.* 2016, 6, 4117" Copyright (2018) American Chemical Society.

	Non-doped	Rh(III)	Rh(IV)	Ru(IV)
On Co	0.61	0.64	0.40	0.42
On dopant	--	0.95	0.67	1.16

Table 5. Computed overpotentials (in V). Adapted with permission from "Nurlaela, E. *et al ACS Catal.* 2016, 6, 4117" Copyright (2018) American Chemical Society.

The table 5 presents the computed overpotential (obtained by the formula 22). Experimentally, we can see that doping of CoOOH with Ru and Rh reduces notable the overpotential (by around 50 mV). This is confirmed by the DFT calculations, even it overestimates the gain in overpotential. The surprising finding is that, upon Rh and Ru doping, the lowest overpotential is not obtained when the reaction happens on the Ru/Rh atoms but on the closest Co atom. The dopant affects the reactivity of the surface Co but seems to not be involved directly in the mechanism.

In term of modelling methodology this result is very surprising. The Nørskov approach is very raw because it doesn't take into account any kinetic aspects (i.e. transition states), because the mechanism proposed takes into account only some elementary steps without any complete investigation of reaction path, because it neglects all electrochemistry aspect (electrochemical potential) and because it neglects all environmental aspects (solvent, electrolyte, pH) that are known to play a very important role in electrochemistry. Nevertheless, we have to admit that this approach works qualitatively well not only in out work but also in several other systems published.[100–102] To go beyond the Nørskov approach is one my research plane for the future. It will be presented at the end of this manuscript.

Chapter IV. Spectroscopy of molecules and solids

Since my arrival at the ENS Lyon in 2012, I have also used my skills in computational spectroscopy. But to me more specific, I have performed only electronic UV-Vis spectroscopic calculations (i.e. absorption, fluorescence, phosphorescence…). If some times I performed vibrational computations, it is only to couple vibrations to electronic excitations. On this topic, my work was mainly oriented toward the understanding of spectroscopic properties of molecules developed for biological applications and toward the understanding of natural photochromic minerals of the sodalite family.

I. Molecules for biological applications

Related Articles:

- B. Mettra, Y. Y. Liao, T. Gallavardin, C. Armagnat, D. Pitrat, P. Baldeck, T. Le Bahers, C. Monnereau, C. Andraud, *Phys. Chem. Chem. Phys.* **2018**
- M. Lepeltier, F. Appaix, Y. Y. Liao, F. Dumur, J. Marrot, T. Le Bahers, C. Andraud, C. Monnereau, *Inorg. Chem.*, **2016**, 55, 9586.
- B. Mettra, F. Appaix, J. Olesiak-Banska, T. Le Bahers, A. Leung, K. Matczyszyn, M. Samoc, B. van der Sanden, C. Monnereau, C. Andraud, *ACS Appl. Mater. Inter.*, **2016**, *8*, 17047.

I.1 General introduction

This work is done in collaboration with Dr. Cyrille Monnereau from the laboratory of chemistry of ENS Lyon. The axis "Functional Materials and Photonics" has been developing molecules for several biological applications for a long time. Two important applications investigated are the fluorescence microscopy and photodynamic therapy.

Fluorescence spectroscopy applied to biological system is an important topic of research, as proven by the recent Nobel prizes in that field (2008 and 2014).[103] Up to now, the fluorescence microscopy was mainly applied to the *in vitro* or *ex vivo* biological systems. But there is a real need of molecular probe developments with the ability to work *in vivo* to investigate biological system in real environment.[104–106] In this field of research, two-photon absorption microscopy (TPA) is probably one of the most promise techniques because the TPA phenomenon is efficient only on the focal point of a focalized light beam, which

facilitates the 3D reconstruction of the image of biological system.[107] To be interesting for this specific application, a molecule must satisfy some requirements:[108–110]

1- It must absorb and emit in the biological transparency window (BTW, between 650-1300 nm). It corresponds to a wavelength window where the absorption of biological tissue is strongly reduced.
2- It must be water-soluble.
3- It must not display any kind of short- and long-term toxicity.
4- It should be synthetically accessible in large scale with a reasonable cost and number of synthesis steps.
5- It should be as specific as possible toward organs or cells.

I.2 Computational details

The computational protocol to compute spectroscopic properties of molecules are notable different from the one used previously to investigate semiconductors.

Codes: Generally, all DFT and TD-DFT calculations were performed with Gaussian09 code.[11] The spin-orbit coupling energy between exited states was computed with the Dalton code[111] while the vibronically resolved UV-Vis spectra were simulated with FCClasses program[112] using the adiabatic transition energies obtained by TD-DFT with Gaussian09 and harmonic vibrational frequencies also calculated with Gaussian09.

Basis set: All calculations were performed with the 6-31+G(d) basis set[12,13] except for Ir atom that used the LANL2DZ pseudo-potential[113] and the associated basis set.

Functional: For the organic molecules, the cam-B3LYP functional was used.[59] This is a range-separated hybrid functional like HSE06 but contrary to this previous functional, cam-B3LYP increases the Hartree-Fock exchange energy with the interelectronic distance (See Figure 13). This functional has proven to be accurate to simulate charge transfer transitions in quadrupolar dyes.[114,115] The PBE0 global hybrid functional was used to simulate spectroscopic properties of Ir complexes presented later, based on previous benchmark I did for inorganic complex dyes.[116]

Environment: Bulk solvent effects were included using the Polarizable Continuum Model (PCM) of Tomasi and co-workers. More specifically, the Conductor-like PCM model as implemented in Gaussian (CPCM) was applied.

I.3 Fluorescent probes for confocal fluorescent microscopy

The anthracene based probes. To fulfil these requirements, Dr. Cyrille Monnereau developed organic molecules having the architecture Donor-Acceptor-Donor presented in the Figure 25. The donor and acceptor chemical groups are aniline and anthracenes respectively, linked by alkyne of dialkyne bridges (Figure 25). This type of architecture, called quadrupolar, is known to lead to strong TPA absorption cross-section.[117] The alkyl groups of aniline were functionalized by polymeric chain to make to molecule water-soluble.

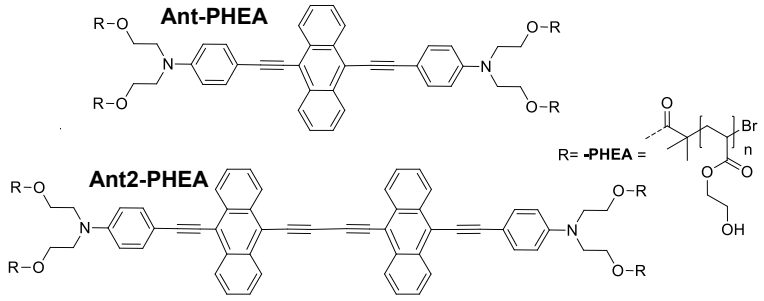

Figure 25. Scheme of the molecules developed for TPA fluorescent probe.

The absorption (one photon, and two-photon) and fluorescence spectra of the molecules are presented in Figure 26. For centro-symmetric molecules, like Ant-PHEA and Ant2-PHEA seem to be, the $S_1 \leftarrow S_0$ electronic transition, intense in one-photon absorption, must be forbidden in TPA leaving only the $S_2 \leftarrow S_0$ transition in TPA. In these spectra, we can see that, there is the intense $S_2 \leftarrow S_0$ transition, but also a small contribution of the $S_1 \leftarrow S_0$ transition violating the selection rule of centro-symmetric molecules. Thus the two molecules presented here are not exactly centro-symmetric at the ground state. In parallel, the large Stocks-shift (difference between the absorption and emission energies) of Ant-PHEA and Ant2-PHEA highlights an important geometric modification between the ground and the excited states.

DFT and TD-DFT calculations were performed to bring an atomistic point of view for these observations. The good qualitative agreement between theory and experiment on both the wavelength position of the maxima and the band shapes proves the accuracy of the computational protocol (Figure 26c). The rigidity of the triple bound used as spacer between the chemical groups was investigated by computing the energy of the system under a rotation around this bond for S_0 and S_1 states. It appears that the rotation is almost free at the ground state (activation barrier of less than 2 $kJ.mol^{-1}$), even leading to a local minimum at 90° of torsion angle between the two anthracenes. But at the excited state, the rotation is more difficult (activation energy around 30 $kJ.mol^{-1}$). Thus the rotations around the 3 triple bond spacers are activated at the ground state, breaking the centro-symmetry of the molecule. But

the molecule becomes very rigid at the excited state, returning to a flat, centro-symmetric geometry confirming the experimental observations.

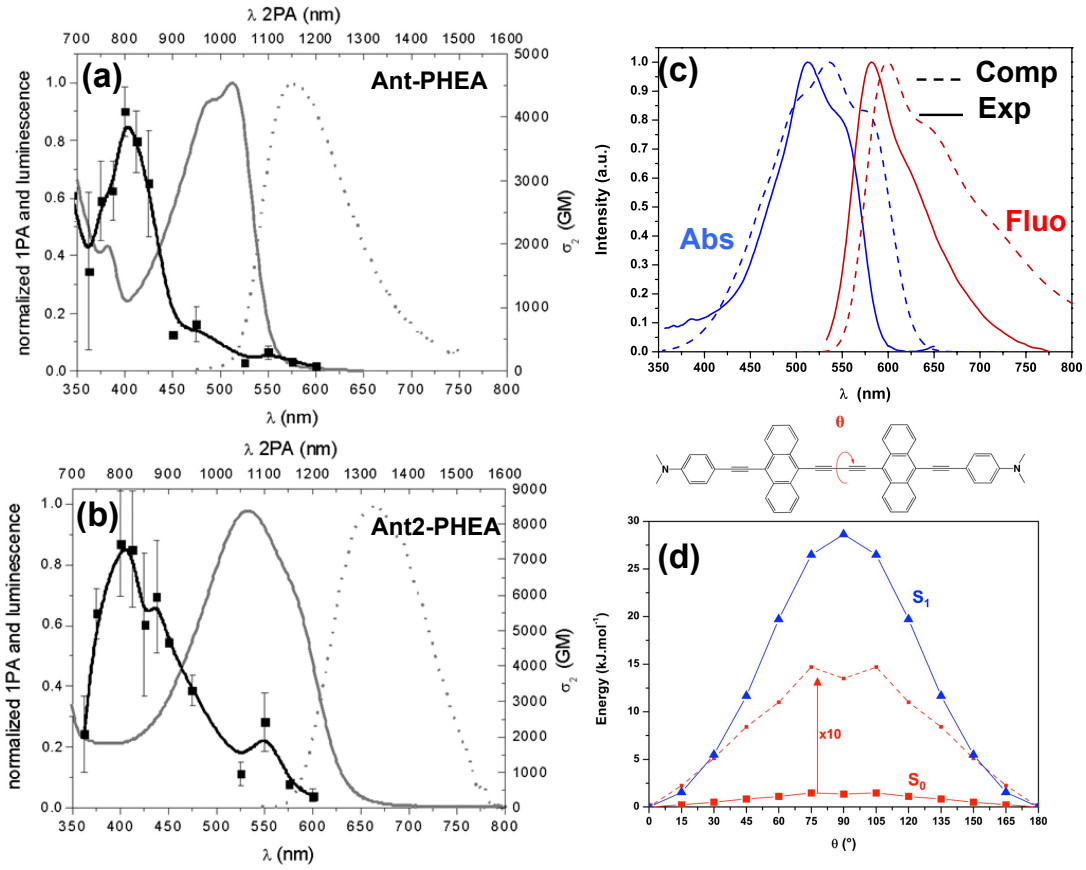

Figure 26. Experimental one- (thin line) and two-photon (large line) absorption and fluorescence (dotted line) spectra of Ant-PHEA (a) and Ant2-PHEA (b). (c) Computed TD-DFT spectra including vibronic coupling (dashed line) and experimental (full line) absorption (blue) and fluorescence (red) spectra. (d) (top) scheme of Ant2, a simplified molecule used to compute the properties of the Ant2 family. (bottom) Computed relative energies of the ground state (in red) and the excited state (in blue) as a function of the dihedral angle. The red dot curve corresponds to the red full line curve multiplied by ten to improve its visibility. Adapted with permission from "Mettra, B. *et al ACS Appl. Mater.* 2016, 8, 17047" Copyright (2018) American Chemical Society.

Iridium based probes. The use of metal-based molecules as fluorescence probe is scarce but Pt and Ir based molecules start to be developed for that purpose.[118–120] The advantages of employing such systems are manifold. First, the Stocks shift and the excited state lifetime are larger for cyclometalated molecules compared to organic ones. Secondly, the phosphorescence efficiency is less prone to photobleaching, a major problem of organic molecules. Finally, the MLCT character of the transitions can help to improve non-linear optical responses.

The iridium complex developed by Dr. Cyrille Monnereau and Dr. Marc Lepeltier is presented in Figure 27a while the absorption and phosphorescence spectra are on Figure 27b. The role of the theoretical calculations was to determine the nature of the transitions involved

and the origin of the shoulders appearing in the first absorption band and in the phosphorescence bands. To summarize these calculations, it appeared that the transitions are a mixture of MLCT and ILCT transitions (Figure 27d and e). In the absorption spectra, the shoulder observed is mainly due to the existence of several small electronic transitions contrary to phosphoresce spectrum that has a vibrational evolution (Figure 27b).

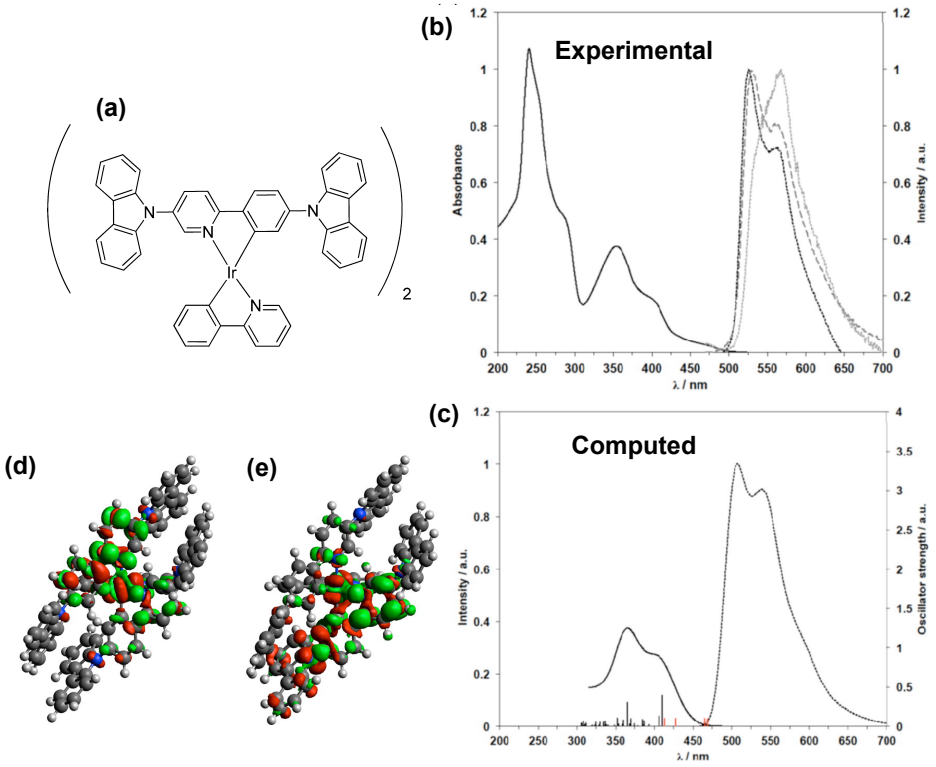

Figure 27. (a) Structure of Ir complex synthetized and computed. (b) Absorption (black full line) and emission of complex 1 in chloroform (black dotted line), at the solid state (gray dotted line) and in pluronic micelles (gray dashed line). (b) TD-DFT computed 50 first singlet-singlet excitations (vertical black lines), the first four singlet-triplet excitations (vertical red lines). The absorption spectrum was simulated up to 310 nm (black line) and was obtained by convoluting the TD-DFT excitations with gaussians (FWHM of 0.35 eV). For singlet-triplet transitions, arbitrary low oscillator strengths were used for the drawing, and those were not included in the simulated absorption spectrum. The simulated phosphorescence spectrum including vibronic coupling is in dashed black line. (d) and (e) Computed electron variation density between the ground and excited states of the most intense transitions of the 400 nm and 350 nm bands respectively. The red and green zones correspond to the regions where the electron density is decreasing and increasing respectively upon excitation (isovalue 0.0006 a.u.). Adapted with permission from "Lepeltier, M. *et al Inorg. Chem.* 2016, *55*, 9586" Copyright (2018) American Chemical Society.

I.4 Singlet oxygen generation for dynamic phototherapy

Another very developed field of research in spectroscopy applied to biological system is the understanding of photo-induced singlet oxygen generation both for its involvement in cancer and skin aging and for its use as cancer therapy. The use of singlet oxygen as a cure is based on its large cytotoxicity, known for more than a century now.[121–123] The photo-induced triplet to singlet transition in oxygen is forbidden both by spin and symmetry selection rules making the direct photo-synthesis of singlet oxygen almost inefficient. The principle of the phototherapy is to use a molecule to absorb the light (with a large absorption coefficient) and transfer the energy to oxygen to put it in a singlet spin state. The use of a TPA mechanism to excite the photosensitizer is a very promising strategy, because the TPA is intense only at the focal point of a focus beam light thus allowing to activate a specific volume to treat. The idea is then to design a photosensitizer that can relax quickly toward the first triplet excited state T_1. Due to the forbidden nature of the S_0-T_1 transition, the T_1 state has a long lifetime allowing to transfer quantitatively the energy to $^3O_2$. The kinetic constant associated to the S_1 to T_1 Inter-System Crossing is labelled k_{ISC}. The mechanism of this singlet oxygen generation is presented in Figure 28.

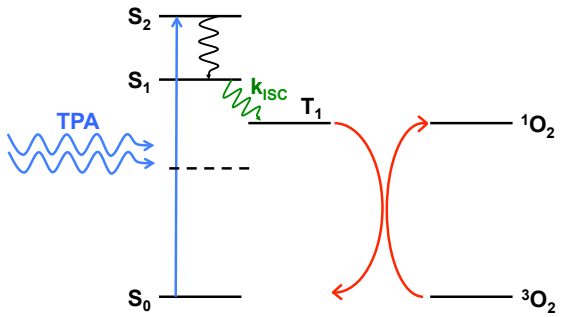

Figure 28. Mechanism of singlet oxygen generation by a TPA.

In term of molecular design, heavy atoms must be placed on the molecule to overcome the spin forbidden S_1-T_1 crossing, through the spin-orbit coupling interaction. For an efficient TPA, as suggested in the discussion on anthracene based fluorescence probe, a quadrupolar architecture is a good starting point. Based on these arguments, Dr. Cyrille Monnereau proposed a series of quadrupolar molecules characterized by aniline donor groups, phenyls as acceptor group separated by triple bound spacers. The accepting groups were functionalized by bromine atoms. The objective of this work was to understand the influence of the conjugation length, the influence of the number of bromine atoms and their position on the

molecule and finally the influence of the spacer (no spacer, triple bound, two triple bounds) on k_{ISC}. This lead to the series of molecules presented in Figure 29.

The photophysical properties of these molecules are presented in Figure 30. They include the fluorescence life-time (noted φ_f), singlet oxygen generation efficiency (noted φ_Δ) and the effective quantum efficiency (noted φ_{eff} and corresponding to the sum $\varphi_f+\varphi_\Delta$). Experimentally, the fluorescence efficiency is obtained by integrating the total emitted light of the sample, after an excitation, and compared to a reference molecule (the coumarin 153 in MeOH, having $\varphi_f=0.45$). The singlet oxygen degeneration efficiency is obtained by measuring and integrating the oxygen phosphorescence ($^1\Delta_g \rightarrow {}^3\Sigma_g$ around 1200 nm) and compared to a reference (phanalanone in $CHCl_3$, $\varphi_\Delta=0.98$). In previous work, *Monnereau at al.* proved that the efficiency of the ISC can be reasonably approximated to the singlet oxygen efficiency in a series of molecules if the effective quantum efficiency remains constant.[124]

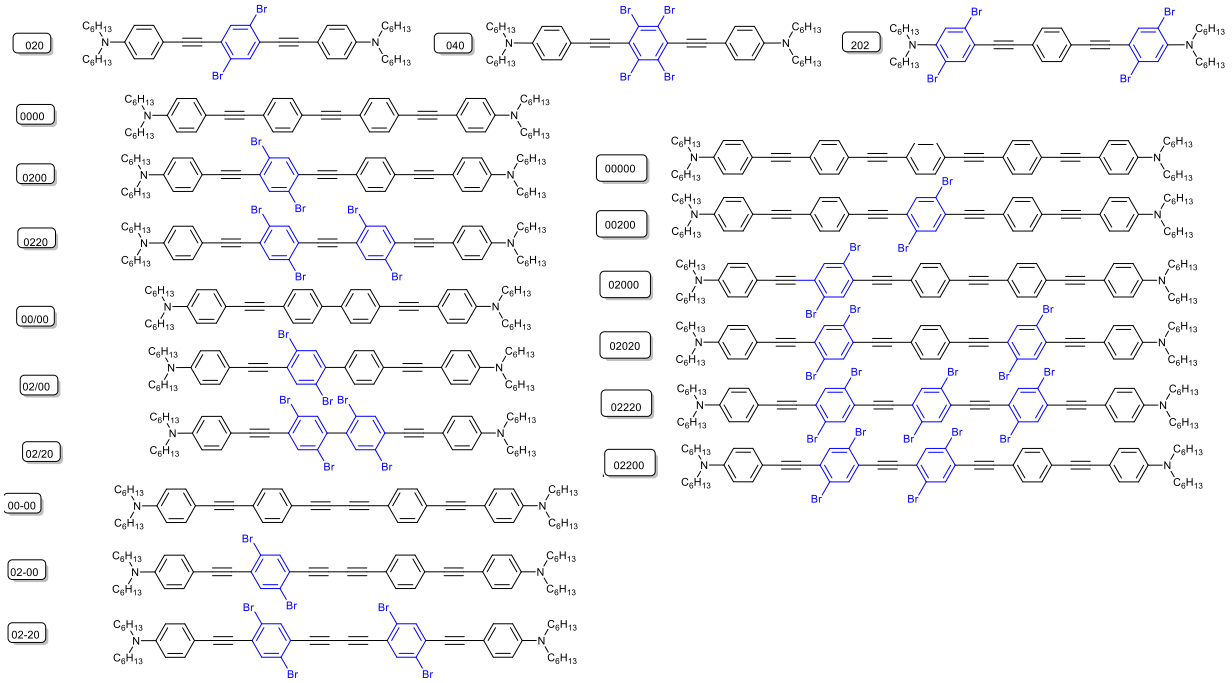

Figure 29. Structures of the molecules investigated for the singlet oxygen generation.

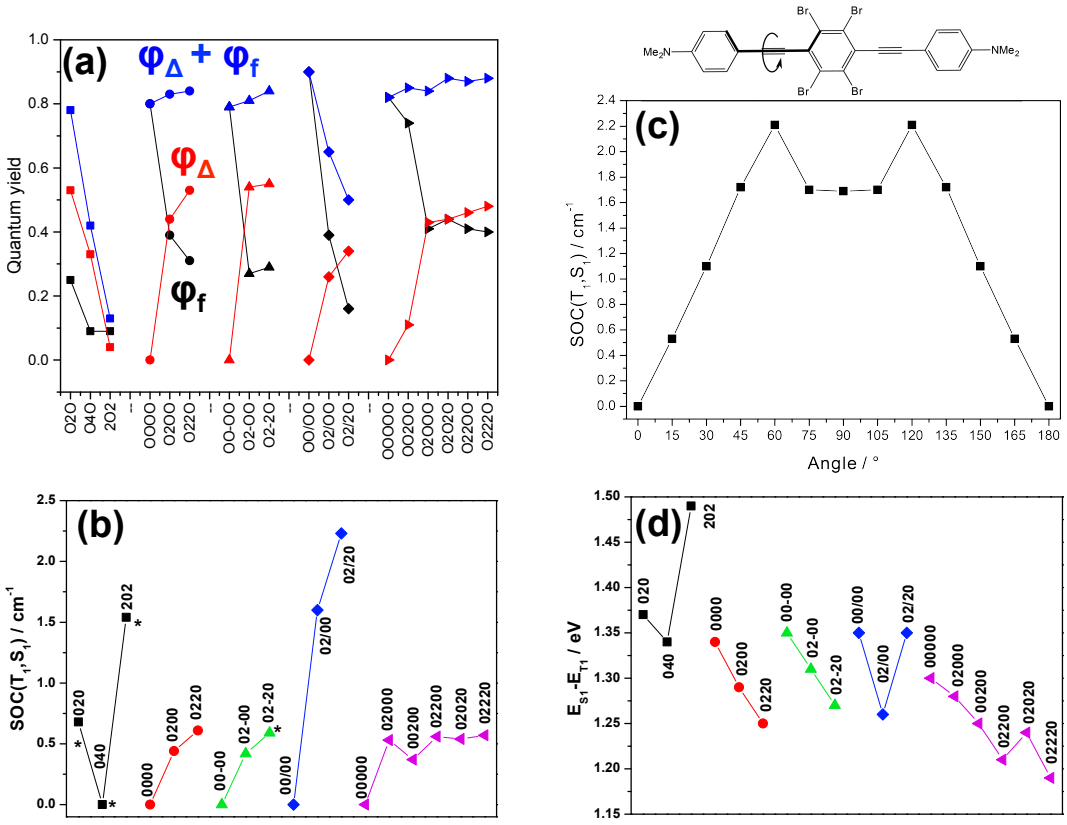

Figure 30. (a) φ_Δ (red curve), φ_f (black curve) and φ_{eff} (blue curve) (b) Computed SOC between the T_1 and S_1 states (c) Computed SOC between the T_1 and S_1 states for 040 as a function of a dihedral angle corresponding to the rotation between two phenyls. (d) Computed energy (in eV) difference between T_1 and S_1 at the S_1 stable geometry.

To summarize the experimental characterization, it appears that the number of bromine atoms has a limited effect on φ_Δ (0200 vs 0220 or 02-20 vs 02-20 or 02000 vs 02200 vs 02220). But the position of bromine substitution can have an important effect (02000 vs 00200). It is difficult to compare 020, 040 and 202 because the effective quantum efficiency (φ_{eff}) is not constant, but qualitatively, the increase of the Br number or the substitution of aniline group deteriorates the photophysical properties of these molecules.

From electronic levels point of view, an efficient ISC between T_1 and S_1 is governed by two parameters (a) the spin-orbit coupling between these two states and (b) the energetic proximity of the two states. As a matter of fact, the equation (23) gives the Fermi Golden rule for a first order transition between S_1 and T_1 states with the spin-orbit coupling Hamiltonian, presented in equation (24). This Hamiltonian, used by the Dalton code and based on Breit-Pauli hamiltonian, treats the spin-orbit interaction with a hydrogen like approach where all bielectronic interactions are simplified by an effective nuclear charge.[125,126]

$$\Gamma_{S1-T1} = \frac{2\pi}{\hbar}\left|\langle T_1|\hat{H}_{SO}|S_1\rangle\right|^2 \delta(E_{S1} - E_{T1}) \qquad (23)$$

$$\widehat{H}_{SO} = \frac{\alpha^2}{2} \sum_{A}^{nucleus} \sum_{i}^{electrons} \frac{Z_{eff}(A)}{R_{iA}^3} (r_i \times p_i).s_i \quad (24)$$

In the equation (23), the former parameter is obtained by spin-orbit coupling (SOC) between S_1 and T_1 noted SOC(T_1,S_1) while the later corresponds to the energy gap between the T_1 and S_1 states, noted $\Delta E(T_1,S_1)$. They were computed at the TD-DFT level and they are presented in Figure 30b and 30d.

We can observe that for each family, the number of Br substituents has a limited effect on the SOC(T_1,S_1) energy with a slight increase with the number of Br atoms, in agreement with the trend observed experimentally. But this conclusion must be weighted by the observation that the geometry of the system as a very large influence on the SOC(T_1,S_1). As a matter of fact, this energy is computed to be 0 for the 040 molecule while experimentally, an evolution of singlet oxygen is observed. Using the selection rule extracted from the Fermi Golden Rule, equation (23), and presented by McClure *et al.*,[127] we understand that the $B_{3u} \leftarrow B_{3u}$ transition in the D_{2h} group, corresponding to the $T_1 \leftarrow S_1$ transition of 040, is forbidden and is the only one forbidden by symmetry in all the investigated compounds. As a matter of fact, for this compound, a calculation of the SOC as a function of the dihedral angle between two phenyls, so reducing the group symmetry from D_{2h} to C_2, indicates that the selection rule on the coupling is removed (Figure 30c). This proves that a small deviation of the 040 from the planar structure allows SOC to reach significant values, comparable or even superior to its dibrominated analogues. In this molecule, the energy necessary to undergo a 30° rotation around the dihedral angle between two adjacent phenyls is as low as 6 kJ/mol at the S_1 state. It explains why this molecule exhibits also a large SOC thus an efficient singlet oxygen generation. The position of the bromine substitution has an effected on SOC(T_1,S_1) as it is larger for 02000 than 00200, in agreement with the larger singlet oxygen efficiency for 02000 than for 00200. About the T_1-S_1 gap, except for 202 and 02/20, the larger the number of bromine atoms, the smaller the energy gap. For the 02/20 molecule, the S_1 geometry is notably different from the S_1 geometries of 00/00 and 02/00 justifying the lake of clear trend in this family. For 202, a substitution of the aniline group is clearly detrimental that could explain why this molecule doesn't evolve any singlet oxygen. In parallel, we have shown (not presented here) that to place Br atoms on the aniline groups kills the charge transfer character of the $S_1 \leftarrow S_0$ transition.

Unfortunately, while TD-DFT could give some insight on experimental photo-physical properties, all the trends cannot be reproduced. Non-radiative phenomenon and a dynamical

point of view are clearly lacking, probably because of the flexibility of the triple bound spacers. Nevertheless, this is a very promising starting point allowing to understand the spectroscopic properties of these families of molecules and orienting the main research axis to improve these investigations.

II. Tenebrescent natural minerals

Related Article:

- A. Curutchet, T. Le Bahers, *Inorg. Chem.* **2017**, *56*, 414.

II.1 Context

This topic gathers my knowledge in solid-state chemistry and in molecular spectroscopy. It originated from my personal curiosity of unusual spectroscopic properties of natural minerals. Tenebrescence is the geological word for photochromism that is the reversible light-induced color change of minerals. Even if nowadays, organic photochromism is much more studied, inorganic photochromic systems show interesting properties such as easy manufacturing and high stability. The main inorganic photochromic materials developed are tungsten oxide (WO_3)[128], molybdenum oxide (MoO_3)[129] and doped titanium oxide (TiO_2)[130]. Surprisingly, the community working on inorganic photochromic materials almost never investigated natural photochromic minerals while known by geologists for a long time. Among them, sodalite group minerals show tenebrescent properties in their natural form. Colorless minerals from sodalite group can be colored in blue or purple under UV exposure.[131,132] The sodalite mineral have the $Na_4(SiAlO_4)_6Cl_2$ composition. The unit cell of the system is presented in Figure 31a. The sodalite structure can be viewed as an alumino-silicate β-cage surrounding a sodium tetrahedron in the middle of which stands a chloride ion. The photochromism mechanism is based on the formation of a F-center (i.e. an electron trapped into a crystal vacancy) by a photo-induced charge transfer from an impurity to an anion vacancy. The quantum energy levels of this trapped electron give the color to the material, while discoloration can be induced by light or thermally, involving the reverse charge-transfer. The first works performed in that field assume that a S_2^{2-} ion substitute a chlorine atom in the sodalite (Figure 31b), creating a vacancy because of charge neutrality and this S_2^{2-} ion is also responsible of

the photo-induced electron transfer (Figure 31c). Images of tenebrescent minerals are presented on Figure 31c.

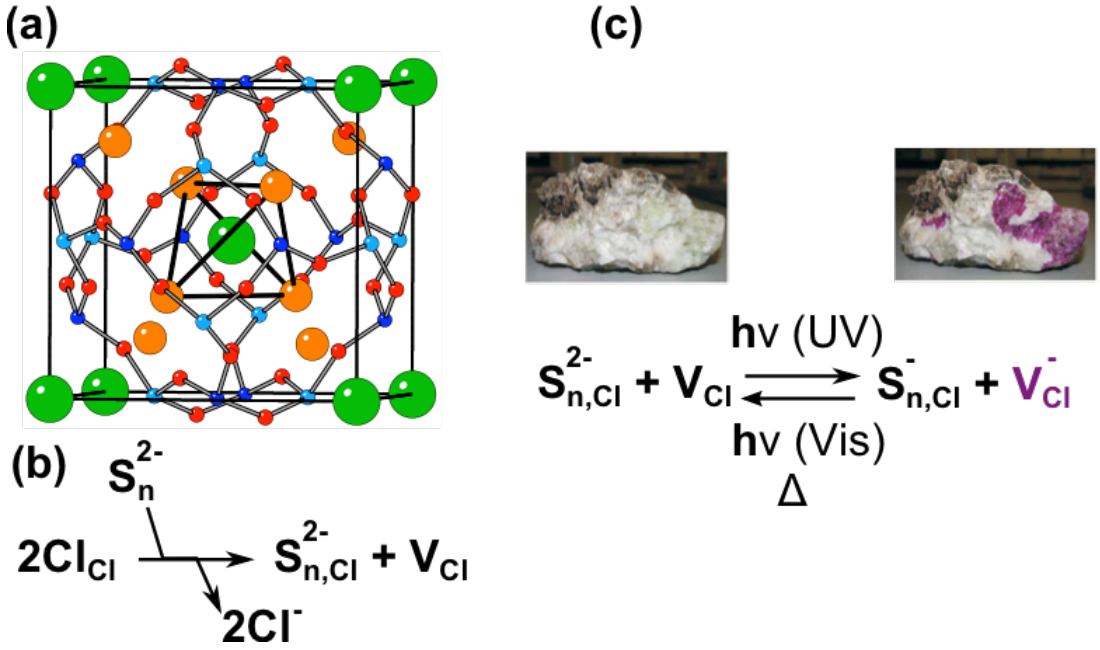

Figure 31: (a) Structure of the sodalite. Blue, cyan, orange, red and green atoms correspond to Si, Al, Na, O and Cl atoms respectively. The tetrahedron of Na atoms is highlighted with black edges. (b) Equation of S_n^{2-} doping. (c) Photochromism mechanism along with photos of naturel sodalite from ref 131.

Recently, we started the modelling of the $Na_4(SiAlO_4)_6(Cl,S)_2$ that is the simplest tenebrescent sodalite. We wanted to model both the spectroscopic properties of the F-center and the mechanism of F-center formation/destruction.[133]

II.2 Computational protocol

The principle of this work is to combine geometries computed in periodic boundary conditions (PBC) and spectroscopic calculations performed as single points on clusters extracted from the PBC geometries.

Codes: All periodic calculations were performed with CRYSTAL14 and spectroscopic calculations with Gaussian09.

Functionals: Geometries were optimized with the global hybrid functional PBE0 as the TD-DFT calculations of the F-center. Simulations of the electron transfer between S_2^{2-} and the vacancy were performed by a post-Hartree-Fock method called SAC-CI because TD-DFT fails to reproduce through space charge transfer transitions.[134,135]

Basis set: All calculations were performed with a double-ζ basis set with polarization functions except for S atoms for which we used a triple-ζ+polarization basis set. For the chlorine vacancy, we optimized a basis set having the structure 11G(d).

Environments: The smallest cluster possible to simulate spectroscopic properties consists of the closest Na atoms around the point defect (the Cl vacancy and the S_2^{2-} ion). To simulate the environment around this small cluster, several types of embedding were tested. A first approach consisted to add clusters of point charges while another approach was to use a larger cluster for the QM calculation, saturated by OH groups.

II.3 F-center spectroscopy

On the spectroscopy of the F-center, a cluster approach appears to be a reliable way to simulate absorption spectrum. Two natures of environment were tested, an electrostatic one simulated by adding increasing size of spherical point charge clusters around sodium tetrahedron (Figure 32a) and a covalent one simulated by adding the full β-cage saturated by OH atoms, without any point charge, in the quantum calculation. We clearly show that the point charge approach has only a weak effect on the F-center absorption wavelength while the inclusion of the full β-cage in the quantum calculation has a larger influence. Using the β-cage, the transition energy was computed at 2.2 eV, very close to the experimental value (~2.2-2.4 eV).

The most relevant and encouraging result comes from the coupling with vibrations. We simulated a vibronic resolved absorption spectrum using the vibrations of sodium tetrahedron (obtained from PBC calculations). The spectrum, presented in Figure 32c, confirms the strong coupling between electronic excitations and vibrations guessed from experimental results. The transition energy is found to be closer to experimental value (computed 2.3 eV, experimental 2.2-2.4 eV).

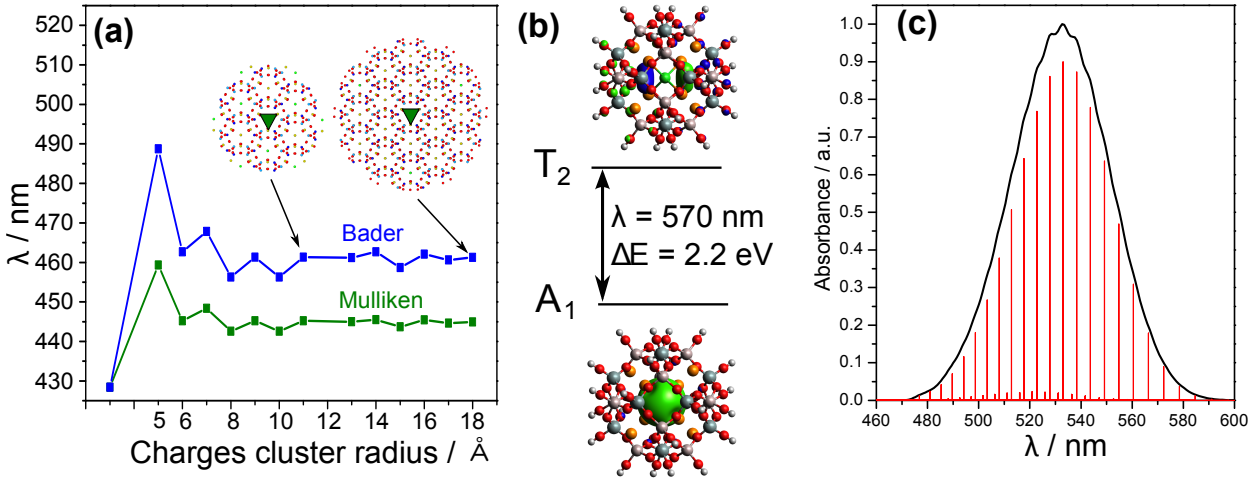

Figure 32: (a) TD-DFT absorption wavelength of the $[Na_4V_{Cl}]^{3+}$ system surrounded by a cluster of point charge (Mulliken or Bader charges) of increasing size. In inset, the green triangle is the quantum part and the points are the charge positions. (b) TD-DFT computed absorption wavelength of a cluster including β-cage, without point charges. (c) Simulated vibronic coupling of the absorption, including only the vibration of the Na_4 tetrahedron.

This approach developed to simulate the F-center absorption was tested on a series of artificial sodalite having the general formula $Na_8(ABO_4)_6(X,S)_2$ (with A=Si,Ge; B=Al,Ga; X=Cl, Br, I). This composition was proposed by Williams *et al.* to tune F-center colour.[136] The Figure 33 presents the first results I obtained on these systems. It corresponds to the absorption wavelength computed for the F-center surrounded only by the sodium tetrahedron or surrounded by the sodium tetrahedron + the β-cage (as in Figure 32b). First, we can see that, taking only the sodium tetrahedron leads to a very poor description of the electronic structure while the inclusion of the β-cage leads to a systematic improvement of the simulation. I am now working on the inclusion of the vibronic coupling on all of these simulations.

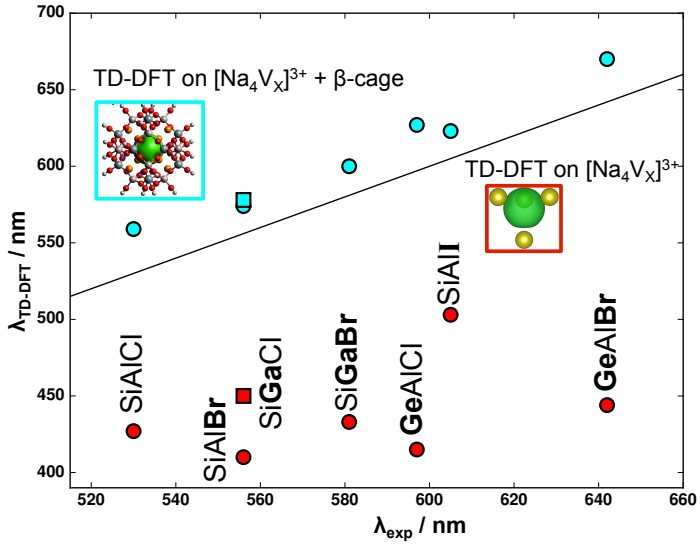

Figure 33. TD-DFT computed absorption wavelength of the first transition of a trapped electron as a function of the sodalite composition. Red and blue points are for the $[Na_4V_{Cl}]^{3+}$ and clusters including β-cage respectively. The black line represents the perfect agreement theory/experiment.

II.4 F-center creation from a charge transfer transition

The mechanism of photochromism (i.e. the formation and destruction of the F-center) was investigated assuming a S_2^{2-} doping. The electronic structure of the system was first computed in PBC and then refined by a cluster approach using post-Hartree-Fock SAC-CI calculations. Two sizes of clusters were tested, a small one including only the closest sodium atoms and a larger one including the first β-cage around the sodium atoms. The geometry relaxation of the excited state was obtained in PBC by a ΔSCF procedure. As presented on Figure 34, a large reorganisation of electronic states happens when the F-center is created that leads to a state inversion for the smaller cluster explaining the meta-stability of the F-center. But the for the larger cluster, the state inversion is no longer observed. This indicates that SAC-CI

calculations are tractable for such systems but also that a better description of the environment is necessary to describe this very sensitive intermolecular charge transfer transition.

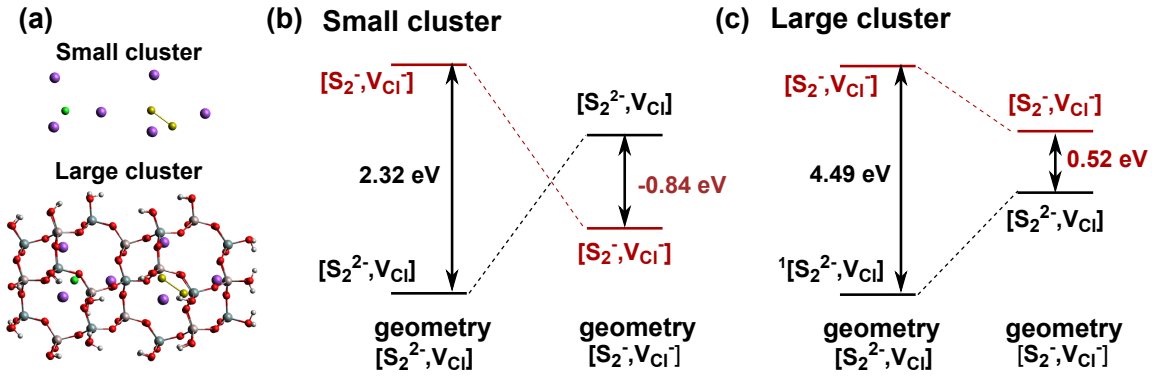

Figure 34: (a) Structure of the small and large clusters. The S_2^{2-} ion is in yellow and the Cl vacancy is in green (b) and (c) SAC-CI transition energies computed for the two clusters for two geometries.

II.5 Overall mechanism

The Figure 35 summarizes all the results obtained in this work. From this, the working principle of hackmanite photochromism can be understood as follows:

1- Under UV irradiation (around 4-5 eV, 250-310 nm), a charge transfer between S_2^{2-} and the vacancy occurs, thus creating a F-center. Due to the weak oscillator strength of this transition (10^{-3} u.a. order of magnitude), a long irradiation time is needed, as experimentally observed.

2- Once the vacancy populated, a geometrical relaxation of the system induces a large reorganisation of the electronic states. Assuming that the lifetime of the electron trapped in the vacancy is long enough (supported by the weak electronic coupling with the disulfide ion as shown by the weak oscillator strength between the two states), an intersystem crossing occurs leading to a triplet state. This state is the most stable one at the relaxed geometry explaining why the electron can be trapped inside the vacancy for days.

3- The trapped electron can absorb light around 2.3 eV (539 nm) with a high oscillator strength due to the allowed nature of the transition. This gives the colour to hackmanite. The shape of the absorption spectrum is a consequence of a strong vibronic coupling.

4- The bleaching of the material corresponds to the electron going back to the disulphide ion. Two ways can be considered from the Figure 35. First, under visible light absorption, the trapped electron goes to the $\mathbf{t_2}$ excited state. During a non-radiative de-excitation, it crosses the electronic state $^1[S_2^{2-}, V_{Cl}]$. Although the coupling between the two states is weak, it can be expected that some electrons return to the disulphide,

which explains the slowness of optical bleaching. Another way of bleaching could be a geometry modification leading to a geometry where the [S_2^{2-}, V_{Cl}] state is again the most stable state. This can be done by heating. These two ways of hackmanite bleaching are experimentally observed[12] and support the energetic diagram presented in Figure 35.

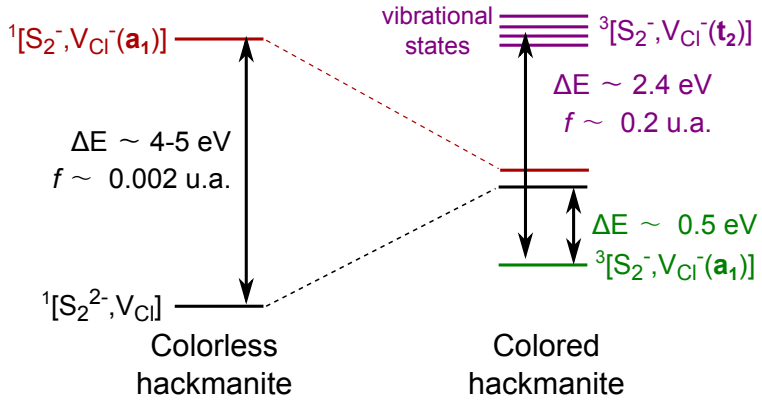

Figure 35. Summary of the computed spectroscopic properties. Adapted with permission from "Curutchet, A.; Le Bahers, T. *Inorg. Chem.* 2017, 56, 414" Copyright (2018) American Chemical Society.

Chapter V. Perspectives

After discussing about my main results obtained since my arrival at the ENS Lyon, it is now time to present my research project for the next few years. This project is based on the topics I already developed, i.e. the photo-electrocatalysis and spectroscopic properties of molecules and solids.

I. Photo-electrocatalysis

The water splitting topic will remain a main part of my research activities in the next few year. This research activity will still be done in collaboration with Pr. Kazuhiro Takanabe first because our research project KAUST-ENSL is continuing during 2 years more (up to the middle of 2020) secondly and more importantly because the collaboration with the group of Pr. Takanabe is very fruitful and we both want to keep working together beyond the administrative framework of the KAUST-ENSL project.

I.1 Co-catalyst for OER and HER

After investigating deeply bulk properties of the semiconductor and assessed several times the computational protocol developed to that purpose, it is now time to move to the co-catalyst. I will investigate it along two approaches.

Semiconductor/Metal for HER. The best HER co-catalyst are noble metals such as Pt or Rh. It exists several ways to deposit this metal on the semiconductor including thermal annealing of salts or photodeposition.[137] It is known that the final size of metallic particle is a large influence on the HER efficiency. More precisely, Pt is very efficient to evolve H_2 but Pt electrodes are known to be also very efficient for the back reaction of water splitting ($H_2 + O_2 \rightarrow H_2O$) while, if small enough (i.e. subnanometer), Pt particles are known to be efficient for H_2 evolution but doesn't do back reaction. Furthermore, surprisingly for small nanoparticles, Rh is more efficient than Pt.[137]

To understand these observations, we decided to investigate the semiconductor/metal particle interfaces. The system selected is $SrTiO_3$ (STO acronym) covered by Pt and Rh particles. The reason of this choice is based on experimental considerations: STO can be synthesized or

even bought with very well defined crystallographic surfaces and the electrochemistry of STO/Pt(Rh) is already developed by the group of Pr. Takanabe. From a calculation point of view, even for very small metal particles, the number of atoms is particularly large. Thus, we are going to use DFT calculations at GGA level with a Hubbard correction to reproduce the electronic structure of STO. The objective is first to extract the electronic structure of the interface to analyse the possibility of electron or hole transfer between the semiconductor and the metal (step 4 in Figure 9). Then, we will investigate the behaviour of the particle as a function of the chemical potential applied on the system. To do so, we will change the number of electrons in the system (simulating oxidation and reduction) and by modelling the compensate charge (i.e. the electrolyte) through Poisson-Boltzmann equations, method developed by Stephan Steinmann in the laboratory, the behaviour of the system as a function of a reference electrode will be obtained. This approach can be called "surface charging model with Poisson-Boltzmann equations". As a matter of illustration, the Figure 36 presents the optimized geometries of some Pt and Rh particles adsorbed on STO(100) surface.

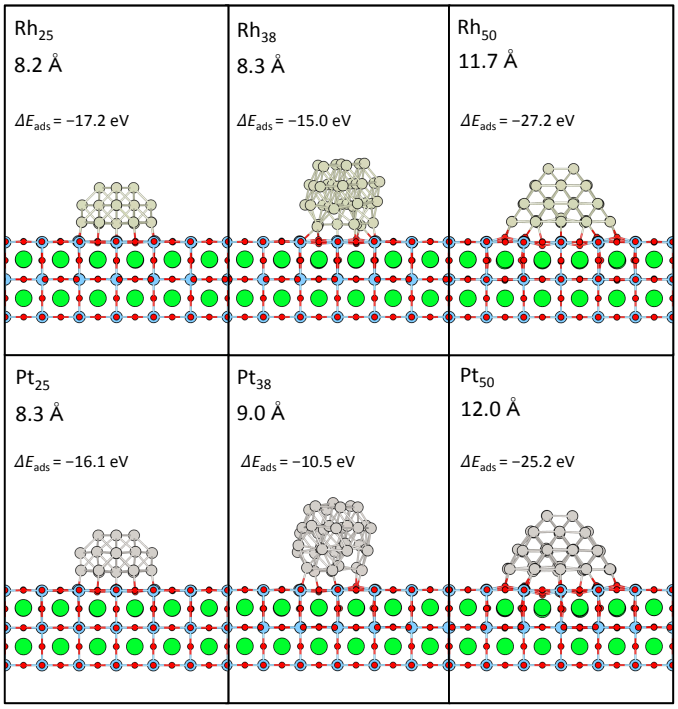

Figure 36. Optimized structure of different Pt and Rh particles adsorbed on STO(100) surface along with the adsorption energy.

OER reaction path on CoOOH. As we have seen on the work dedicated to the overpotential of OER on CoOOH, the Nørvskov approach used for the modelling is very raw, while giving results qualitatively in agreement with the experiment. The idea is now to perform a deeper and more accurate analysis of the oxygen evolution mechanism. The reaction path of the OER

on top of the CoOOH(10-14) surface is going to be performed including implicit solvent in a continuum approximation. The electrochemical potential will be simulated using the surface-charging model with Poisson-Boltzmann equations, as presented for Pt particles on STO. This study will also include the search for transition steps, at least for the non-electrochemcial reaction step (i.e. where no electrons are transferred during this step). Once all the tools developed to investigate this reaction will be operational, I want to apply them on the OER mechanism on NiOOH to understand the difference of overpotential observed experimentally between the two catalysts.

I.2 Toward a multi-scale modelling of water splitting

This idea is to use the properties computed for the bulk semiconductor to simulate the electron and hole currents inside the semiconductor particles. To do so, we will solve the semi-classical semiconductor equations that involve the knowledge of the dielectric constant, charge mobilities… that will be computed at the DFT level. From these flux of charge carriers, we can extract electrochemical potential inside the particle and estimate the electrochemical potential felt by the co-catalyst. Based on the hypothesis that we will know the OER/HER mechanisms as a function of the electrochemical potential (see the previous paragraph), we could have access to the reaction rate at the co-catalyst surface. To perform this type of modelling, we will use the COMSOL Multiphysics package.

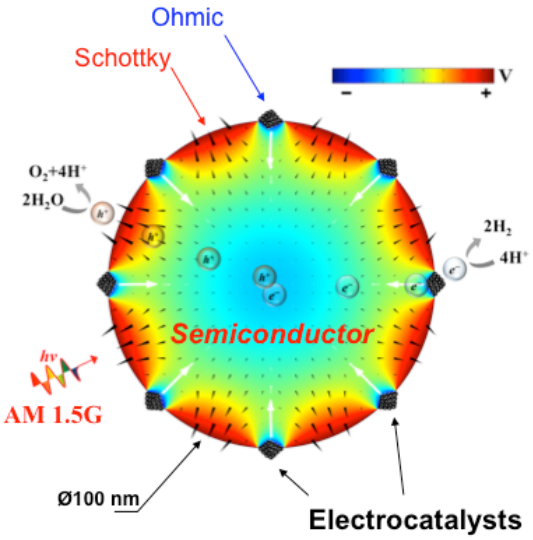

Figure 37. Illustrative representation of the hole and electron flux inside a semiconductor particle creating a potential gradient. Adapted from the work of Angel T. Garcia-Esparza from ref 138.

I.3 Biomass based photocatalysis

This project is in collaboration with Pr. Javier Giorgi and Pr. Elena Baranova (University of Ottawa, Canada).

Electro-oxidation of biomass-sourced molecules offers a sustainable way to synthesise small molecules for the chemical industry. The approach of combining anodic oxidation of glycerol without C-C-C cleavage to generate value-added chemicals with concurrent cathodic production of H_2 in an electrolytic cell has gained considerable attention in the recent years.[139–142] For that reason, the search of efficient electro-catalysts for that application is a growing topic. However, this process needs an external source of electricity meaning that it is energy consuming. The use of light, and more specifically sunlight, as a source of electrochemical potential could solve this energy consumption problematic by generating the appropriate electrical potential in the electro-catalyst upon light absorption.

The objective of the project is to use the methodology of the rational design of photocatalyst developed for water splitting to the biomass conversion with the aim of selecting the most efficient and stable semiconductor. This work will be based on the glycerol oxidation to the dihydroxyacetone. Based on the redox potential associated to this reaction, the valence and conduction positions of the semiconductors will be established and the optimum bandgap will be determined. By adding other requirements based on the dielectric constants, effective masses and exciton binding energies, a full requirements list for the semiconductor will be established offering a way to a thermodynamic based estimation of maximum photoconversion efficiency achievable and the optimum light source. The photocatalyst will be tested experimentally for oxidation of glycerol in Canada.

II. Spectroscopy of molecules and solids

II.1 ANR TeneMod

The research project of tenebrescent sodalites has been funded by the “Agence Nationale de la Recherche”, under the name TeneMod (ANR-17-CE29-0007-21) from now to 2021. This paragraph summarizes the tasks proposed for this project. Within this project, I am developing a collaboration with Pr. Mika Lastusaari (Turku University, Finland) whose group works on this mineral.

Task 1- Improve the simulation of the crystal embedding for the cluster calculations. The idea is now to combine the electrostatic embedding with point charges and the cluster including

the β-cage. The problem of point charges is that, using fixed point charges (whatever the type of charges), the Madelung potential is not converging with the cluster size.[143] One solution proposed to overcome this problem is to replace fixed point charges by parameterized point charges such as to reproduce the Madelung potential.[144,145] This approach will be tested both to simulate F-center spectroscopic properties and the S_2^{2-}—V_{Cl} charge transfer. Then, other type of dopant will be considered (S_2^- and S^{2-}) to try to find which one is the one responsible of the photochromic activity.

Task 2- The question of the mechanism of tenebrescence of scapolites ($Na_4(Si_3AlO_6)_3Cl$) and tugtupites ($Na_4Si_4AlBeO_{12}Cl$) is the subject of this task. The photochromism of these minerals have almost never been investigated and are known only from geologists as curiosity objects. They assume that the mechanism of tenebrescence is the same as sodalites but without any proof. Interestingly, tugtupites have a very similar crystal structure to sodalite but with Be atoms replacing Al and Si ones in the β-cage. Scapolites have a chemical composition similar to sodalites, but the sodium polyhedron around V_{Cl} is not a tetrahedron but a flat square. So, these two minerals will be good testing systems for the computational protocol.

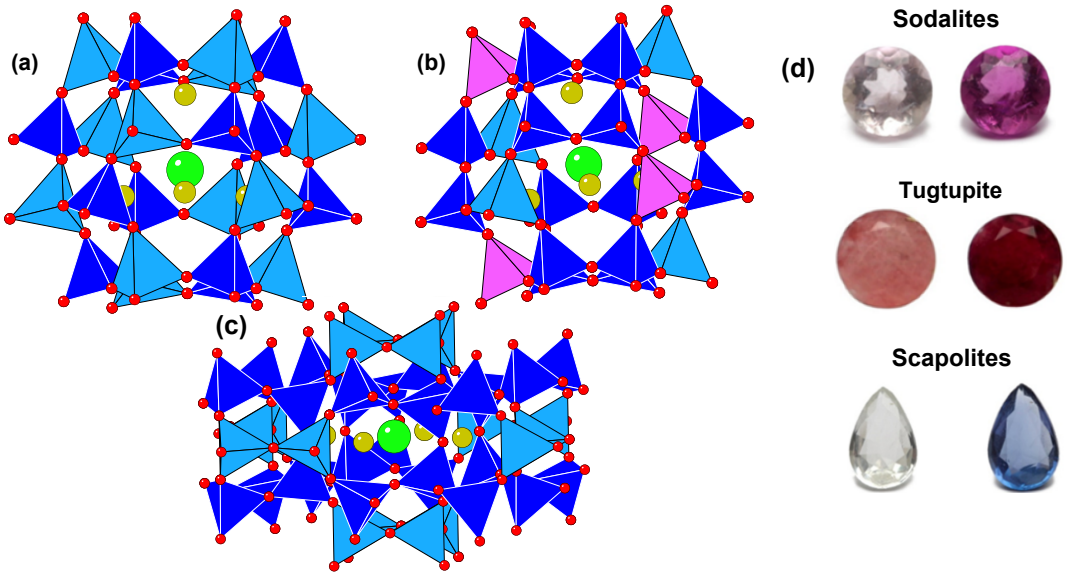

Figure 38: β-cages of sodalite (a), tugtupite (b) and scapolites (c). Na, Cl and O atoms are in yellow, green and red respectively. Si, Al and Be tetrahedrons are in blue, cyan and pink respectively. (d) photos of natural gems of hackmanites, tugtupites and scapolites in there colourless and coloured forms (From [132]).

Task 3- The protocol developed in Task 1 will be tested on other composition of sodalites having the general formula $A_4(BCO_4)_6R_2$ (A=Na,Li,K,Rb; B=Si,Ge; C=Al,Ga; R=Cl,Br,I) based on the experimental work of Williams et al. and in collaboration with Mika Lastusaari's group.[136] Beyond the assessment of the approach, this will help to understand the influence of the composition on the tenebrescence of this family of minerals.

Task 4- In this task, we will work on the accurate modelling of the colour. The objective is to predict the final aspect of the mineral including not only the absorption spectra simulated in the previous tasks but also the light scattering induced by the powder nature of the samples or by the surface texture of the natural minerals. The light scattering will be simulated using the COMSOL multiphysics software with the "Wave Optics" Module including the simulation of light scattering. In this module, the full Maxwell equations are numerically resolved on a grid.

Task 5- The final task is a perspective on the modelling of colours of other type of minerals that are cordierite and alexandrite. These minerals are known to be polychromic, a phenomenon that can be correctly simulated only by methods able to reproduce perfectly minerals absorption spectra. They will be a challenging test case for the protocol of *in silico* colour simulation developed for minerals.

II.2 Collaborations with the "Functional Materials and Photonics" axis of the laboratory

In the next years, I plan to continue my integration into the laboratory by continuing my collaborations with the "Functional Materials and Photonics" axis of the laboratory. I will continue the work on molecules developed for TPA absorption spectroscopy. To that purpose, I want to assess the implementations of the quadratic response TD-DFT that are now proposed in several codes (such as Dalton or Turbomole). I will also continue the work on the design of molecules for singlet oxygen generation by correlating molecular properties computed at the quantum chemical level and experimental singlet oxygen production efficiency.

Conclusion

Dans ce document, j'ai retracé mes activités de recherche depuis mes débuts de chercheur (que j'assimile à mon doctorat) jusqu'à aujourd'hui. J'espère avoir convaincu les lecteurs que les thématiques de recherche que je développe actuellement résultent en fait d'une évolution naturelle liée au personnes et aux équipes de recherche que j'ai rencontrées pendant ma thèse, mon post-doctorat et mes premières années en tant que maître de conférences.

Depuis mon arrivée au laboratoire de chimie de l'ENS Lyon, j'ai toujours eu à cœur de développer mes propres axes de recherches, mais toujours en lien avec les thématiques historiques de l'axe de chimie théorique. C'est pour cette raison que j'ai débuté l'étude de la photodissociation de l'eau combinant mes connaissances en matériaux semiconducteurs et en phénomènes photo-induits avec celles de l'axe de chimie théorique en catalyse. Comme le lecteur l'aura certainement deviné, ces travaux ont énormément bénéficié de la collaboration avec le Pr. Kazuhiro Takanabe via le projet de recherche KAUST-ENSL qui a permis le recrutement d'un post-doctorant depuis 2015 sur ce sujet. Mais les travaux sur la photodissociation de l'eau vont au delà de cette collaboration, comme le montrent les articles que j'ai publiés sur ce sujet avec d'autres chercheurs.
La collaboration avec les équipes d'expérimentateurs du laboratoire de chimie a toujours été pour moi une évidence. Les thématiques qu'elles développent autour de la spectroscopie que ce soit de molécules ou de matériaux entrent parfaitement dans mon domaine de compétence. C'est pour moi l'occasion de maintenir mes aptitudes en spectroscopie mais aussi de développer de nouvelles connaissances. Au delà de ces aspects techniques, je suis convaincu que la collaboration avec les groupes expérimentateurs est une pierre angulaire du laboratoire.

Mes perspectives de travaux de recherche sont une évolution des sujets de recherche actuels. Il y a tout d'abord une modélisation plus poussée de la photodissociation de l'eau en prenant en compte l'interaction semiconducteur/co-catalyseur et en déterminant le mécanisme réactionnel de l'évolution de l'oxygène. Ces travaux seront faits en collaboration avec d'autres membres de l'axe de chimie théorique (Stephan Steinmann, Carine Michel et David Loffreda) afin d'unir nos compétences individuelles pour traiter correctement ces sujets

complexes. Je souhaite aussi mettre en place une modalisation multi-échelles du photocatalyeur. Ma conviction sous-jacente est qu'il est possible de valoriser davantage les calculs de propriétés de semiconducteurs que j'ai développés jusque là. La modélisation multi-échelles, faisant intervenir ces propriétés dans les équations semi-classiques des semiconducteurs, est une réponse que j'ai imaginée pour cette valorisation. Enfin vient l'ANR sur les matériaux ténébrescents. J'ai monté ce projet de recherche en combinant mes compétences en chimie du solide et en spectroscopie avec une curiosité personnelle pour ces minéraux naturelles. Au fur et à mesure de la rédaction de ce projet, il m'est clairement apparu que ces matériaux, au delà de leur étude fondamentale passionnante, avait de réelles possibilités d'application mais encore faut-il convaincre la communauté de ces potentialités. Charge à moi de trouver les arguments qui feront entrer les matériaux ténébrescents dans les composés de haute-technologie…

Grâce à ce document, j'espère avoir convaincu les lecteurs et plus particulièrement les membres du jury, de mes aptitudes à développer des activités de recherches qui sont à la fois indépendantes et à la fois en accord avec les thématiques de recherche portées par le laboratoire de chimie de l'ENS Lyon. De par les encadrements de stagiaires, doctorants et post-doctorants que j'ai réalisés, j'espère aussi avoir convaincu de mes capacités à accompagner des étudiants ou jeunes chercheurs vers l'autonomie et les compétences que demande le métier de chercheur.

References

(1) O'Regan, B.; Grätzel, M. A Low-Cost, High-Efficiency Solar Cell Based on Dye-Sentized Colloidal TiO_2 Film. *Nature* **1991**, *353*, 737–740.

(2) Mishra, A.; Fischer, M. K. R.; Bäuerle, P. Metal-Free Organic Dyes for Dye-Sensitized Solar Cells: From Structure: Property Relationships to Design Rules. *Angew. Chem. Int. Ed.* **2009**, *48* (14), 2474–2499.

(3) Hagfeldt, A.; Boschloo, G.; Sun, L.; Kloo, L.; Pettersson, H. Dye-Sensitized Solar Cells. *Chem. Rev.* **2010**, *110*, 6595–6663.

(4) Pauporté, T.; Lincot, D. Electrodeposition of Semiconductors for Optoelectronic Devices: Results on Zinc Oxide. *Electrochim. Acta* **2000**, *45* (20), 3345–3353.

(5) Labat, F.; Adamo, C. Bi-Isonicotinic Acid on Anatase (101): Insights from Theory. *J. Phys. Chem. C* **2007**, *111* (41), 15034–15042.

(6) Ciofini, I.; Lainé, P. P.; Bedioui, F.; Adamo, C. Photoinduced Intramolecular Electron Transfer in Ruthenium and Osmium Polyads: Insights from Theory. *J. Am. Chem. Soc.* **2004**, *126* (34), 10763–10777.

(7) Fortage, J.; Peltier, C.; Nastasi, F.; Puntoriero, F.; Tuyèras, F.; Griveau, S.; Bedioui, F.; Adamo, C.; Ciofini, I.; Campagna, S.; et al. Designing Multifunctional Expanded Pyridiniums: Properties of Branched and Fused Head-to-Tail Bipyridiniums. *J. Am. Chem. Soc.* **2010**, *132* (46), 16700–16713.

(8) Goux, A.; Pauporté, T.; Yoshida, T.; Lincot, D. Mechanistic Study of the Electrodeposition of Nanoporous Self-Assembled ZnO/Eosin Y Hybrid Thin Films: Effect of Eosin Concentration. *Langmuir* **2006**, *22* (25), 10545–10553.

(9) Yoshida, T.; Zhang, J.; Komatsu, D.; Sawatani, S.; Minoura, H.; Pauporté, T.; Lincot, D.; Oekermann, T.; Schlettwein, D.; Tada, H.; et al. Electrodeposition of Inorganic/Organic Hybrid Thin Films. *Adv. Funct. Mater.* **2009**, *19* (1), 17–43.

(10) Pauporté, T.; Yoshida, T.; Cortès, R.; Froment, M.; Lincot, D. Electrochemical Growth of Epitaxial Eosin/ZnO Hybrid Films. *J. Phys. Chem. B* **2003**, *107* (37), 10077–10082.

(11) Frisch, M. J.; Trucks, G. W.; Schlegel, H. B.; Scuseria, G. E.; Robb, M. A.; Cheeseman, J. R.; G., S.; Barone, V.; Mennucci, B.; Petersson, G. A.; et al. Gaussian. Gaussian Inc.: Wallingford CT 2009, p Gaussian Inc.

(12) Adamo, C.; Barone, V. Toward Reliable Density Functional Methods without Adjustable Parameters: The PBE0 Model. *J. Chem. Phys.* **1999**, *110*, 6158–6170.

(13) Hehre, W. J.; Ditchfield, R.; Pople, J. A. Self—Consistent Molecular Orbital Methods. XII. Further Extensions of Gaussian—Type Basis Sets for Use in Molecular Orbital Studies of Organic Molecules. *J. Chem. Phys.* **1972**, *56* (5), 2257.

(14) Tomasi, J.; Persico, M. Molecular Interactions in Solution: An Overview of Methods Based on Continuous Distributions of the Solvent. *Chem. Rev.* **1994**, *94* (7), 2027–2094.

(15) Tomasi, J.; Mennucci, B.; Cammi, R. Quantum Mechanical Continuum Solvation Models. *Chem. Rev.* **2005**, *105* (8), 2999–3093.

(16) Laurent, A. D.; Jacquemin, D. TD-DFT Benchmarks: A Review. *Int. J. Quantum Chem.* **2013**, *113* (17), 2019–2039.

(17) Jacquemin, D.; Perpète, E. A.; Ciofini, I.; Adamo, C. Accurate Simulation of Optical Properties in Dyes. *Acc. Chem. Res.* **2009**, *42* (2), 326–334.

(18) Dovesi, R.; Saunders, V. R.; Roetti, C.; Orlando, R.; Pascale, F.; Civalleri, B.; Doll, K.; Harrison, N. M.; Bush, I. J.; Llunell, M.; et al. Crystal09 1.0.0. *Crystal09 user's Man.* **2009**, universita di Torino, Italy.

(19) Le Bahers, T.; Pauporté, T.; Scalmani, G.; Adamo, C.; Ciofini, I. A TD-DFT Investigation of Ground and Excited State Properties in Indoline Dyes Used for Dye-Sensitized Solar Cells. *Phys. Chem. Chem. Phys.* **2009**, *11* (47), 11276–11284.

(20) Le Bahers, T.; Labat, F.; Pauporté, T.; Ciofini, I. Effect of Solvent and Additives on the Open-Circuit Voltage of ZnO-Based Dye-Sensitized Solar Cells: A Combined Theoretical and Experimental Study. *Phys. Chem. Chem. Phys.* **2010**, *12* (44), 14710–14719.

(21) Le Bahers, T.; Pauporté, T.; Lainé, P. P.; Labat, F.; Adamo, C.; Ciofini, I. Modeling Dye-Sensitized Solar Cells : From Theory to Experiment. *J. Phys. Chem. Lett.* **2013**, *4*, 1044–1050.

(22) Le Bahers, T.; Labat, F.; Pauporté, T.; Lainé, Philippe, P.; Ciofini, I. Theoretical Procedure for Optimizing Dye-Sensitized Solar Cells : From Electronic Structure to Photovoltaic Efficiency. *J. Am. Chem. Soc.* **2011**, *133*, 8005.

(23) Le Bahers, T.; Adamo, C.; Ciofini, I. A Qualitative Index of Spatial Extent in Charge-Transfer Excitations. *J. Chem. Theory Comput.* **2011**, *7*, 2498–2506.

(24) Adamo, C.; Le Bahers, T.; Savarese, M.; Wilbraham, L.; García, G.; Fukuda, R.; Ehara, M.; Rega, N.; Ciofini, I. Exploring Excited States Using Time Dependent Density Functional Theory and Density Based Indexes. *Coord. Chem. Rev.* **2015**, *304–305*, 166–178.

(25) Peach, M. J. G.; Benfield, P.; Helgaker, T.; Tozer, D. J. Excitation Energies in Density Functional Theory: An Evaluation and a Diagnostic Test. *J. Chem. Phys.* **2008**, *128* (4), 44118.

(26) Pastore, M.; Mosconi, E.; Angelis, F. De; Grätzel, M. A Computational Investigation of Organic Dyes for Dye-Sensitized Solar Cells : Benchmark , Strategies , and Open Issues. *J. Phys. Chem. C* **2010**, *114*, 7205–7212.

(27) Blandford, R.; Watkins, M. This Month in Physics History: April 25, 1954: Bell Labs Demonstrates the First Practical Silicon Solar Cell. *APS News* **2009**, *18* (4), 2.
(28) Photovotlaic Efficiency Chart. *Natl. Renew. Energy Lab.* **2018**, https://www.nrel.gov/pv/assets/images/efficiency-c.
(29) Energie photovoltaïque en France.
(30) Panorama de l'électricité renouvelable au 30 septembre 2017.
(31) Dubal, D. P.; Ayyad, O.; Ruiz, V.; Gómez-Romero, P. Hybrid Energy Storage: The Merging of Battery and Supercapacitor Chemistries. *Chem. Soc. Rev.* **2015**, *44* (7), 1777–1790.
(32) Habisreutinger, S. N.; Schmidt-Mende, L.; Stolarczyk, J. K. Photocatalytic Reduction of CO_2 on TiO_2 and Other Semiconductors. *Angew. Chem. Int. Ed.* **2013**, *52*, 7372–7408.
(33) Morris, A. J.; Meyer, G. J.; Fujita, E. Molecular Approaches to the Photocatalytic Reduction of Carbon Dioxide for Solar Fuels. *Acc. Chem. Res.* **2009**, *42* (12), 1983–1994.
(34) Chang, X.; Wang, T.; Gong, J. CO2 Photo-Reduction: Insights into CO_2 Activation and Reaction on Surfaces of Photocatalysts. *Energy Environ. Sci.* **2016**, *9* (7), 2177–2196.
(35) Chen, X.; Shen, S.; Guo, L.; Mao, S. Semiconductor-Based Photocatalytic Hydrogen Generation. *Chem. Rev.* **2010**, *110* (11), 6503–6570.
(36) Hisatomi, T.; Kubota, J.; Domen, K. Recent Advances in Semiconductors for Photocatalytic and Photoelectrochemical Water Splitting. *Chem. Soc. Rev.* **2014**, *43* (22), 7520–7535.
(37) Pinaud, B. A.; Benck, J. D.; Seitz, L. C.; Forman, A. J.; Chen, Z.; Deutsch, T. G.; James, B. D.; Baum, K. N.; Baum, G. N.; Ardo, S.; et al. Technical and Economic Feasibility of Centralized Facilities for Solar Hydrogen Production via Photocatalysis and Photoelectrochemistry. *Energy Environ. Sci.* **2013**, *6* (7), 1983.
(38) Shaner, M. R.; Atwater, H. A.; Lewis, N. S.; McFarland, E. W. A Comparative Technoeconomic Analysis of Renewable Hydrogen Production Using Solar Energy. *Energy Environ. Sci.* **2016**, *9* (7), 2354–2371.
(39) Seitz, L. C.; Chen, Z.; Forman, A. J.; Pinaud, B. A.; Benck, J. D.; Jaramillo, T. F. Modeling Practical Performance Limits of Photoelectrochemical Water Splitting Based on the Current State of Materials Research. *ChemSusChem* **2014**, *7* (5), 1372–1385.
(40) Fabian, D. M.; Hu, S.; Singh, N.; Houle, F. A.; Hisatomi, T.; Domen, K.; Osterloh, F. E.; Ardo, S. Particle Suspension Reactors and Materials for Solar-Driven Water Splitting. *Energy Environ. Sci.* **2015**, *8* (10), 2825–2850.
(41) Sivula, K.; van de Krol, R. Semiconducting Materials for Photoelectrochemical Energy Conversion. *Nat. Rev. Mater.* **2016**, *1*, 15010.
(42) Perdew, J. P.; Yang, W.; Burke, K.; Yang, Z.; Gross, E. K. U.; Scheffler, M.; Scuseria, G. E.; Henderson, T. M.; Zhang, I. Y.; Ruzsinszky, A.; et al. Understanding Band Gaps of Solids in Generalized Kohn–Sham Theory. *Proc. Natl. Acad. Sci. USA PNAS* **2017**, *114* (11), 2801–2806.
(43) Onida, G.; Reining, L.; Rubio, A. Electronic Excitations : Density-Functional versus Many-Body Green ' S-Function Approaches. *Rev. Mod. Phys.* **2002**, *74*, 601–659.
(44) Blase, X.; Duchemin, I.; Jacquemin, D. The Bethe–Salpeter Equation in Chemistry: Relations with TD-DFT, Applications and Challenges. *Chem. Soc. Rev.* **2018**.
(45) Madsen, G. K. H.; Singh, D. J. BoltzTraP. A Code for Calculating Band-Structure Dependent Quantities. *Comput. Phys. Commun.* **2006**, *175* (1), 67–71.
(46) Dovesi, R.; Orlando, R.; Erba, A.; Zicovich-Wilson, C. M.; Civalleri, B.; Casassa, S.; Maschio, L.; Ferrabone, M.; De La Pierre, M.; D'Arco, P.; et al. CRYSTAL14 : A Program for the Ab Initio Investigation of Crystalline Solids. *Int. J. Quantum Chem.* **2014**, *114*, 1287–1317.
(47) Kresse, G.; Hafner, J. Ab Initio Molecular Dynamics for Liquid Metals. *Phys. Rev. B* **1993**, *47*, 558–561.
(48) Kresse, G.; Furthmüller, J. Efficiency of Ab-Initio Total Energy Calculations for Metals and Semiconductors Using a Plane-Wave Basis Set. *Comput. Mater. Sci.* **1996**, *6*, 15–50.
(49) Kresse, G.; Joubert, D. From Ultrasoft Pseudopotentials to the Projector Augmented-Wave Method. *Phys. Rev. B* **1999**, *59*, 11–19.
(50) Heyd, J.; Peralta, J. E.; Scuseria, G. E.; Martin, R. L. Energy Band Gaps and Lattice Parameters Evaluated with the Heyd-Scuseria-Ernzerhof Screened Hybrid Functional. *J. Chem. Phys.* **2005**, *123* (17).
(51) Paier, J.; Marsman, M.; Hummer, K.; Kresse, G.; Gerber, I. C.; Angyán, J. G. Screened Hybrid Density Functionals Applied to Solids. *J. Chem. Phys.* **2006**, *124*, 154709.
(52) Xiao, H.; Tahir-Kheli, J.; Goddard, W. A. Accurate Band Gaps for Semiconductors from Density Functional Theory. *J. Phys. Chem. Lett.* **2011**, *2* (3), 212–217.
(53) Perdew, J. P.; Ernzerhof, M.; Burke, K. Rationale for Mixing Exact Exchange with Density Functional Approximations. *J. Chem. Phys.* **1996**, *105* (22), 9982–9984.
(54) Heyd, J.; Scuseria, G. E.; Ernzerhof, M. Hybrid Functionals Based on a Screened Coulomb Potential. *J. Chem. Phys.* **2003**, *118* (18), 8207–8215.
(55) Heyd, J.; Scuseria, G. E.; Ernzerhof, M. Erratum: "Hybrid Functionals Based on a Screened Coulomb Potential" [J. Chem. Phys. 118, 8207 (2003)]. *J. Chem. Phys.* **2006**, *124* (21), 219906.
(56) Le Bahers, T.; Rérat, M.; Sautet, P. Semiconductors Used in Photovoltaic and Photocatalytic Devices : Assessing Fundamental Properties from DFT. *J. Phys. Chem. C* **2014**, *118*, 5997–6008.
(57) Madelung, O. *Semiconductors: Data Handbook*, Third edit.; Springer, 2004.
(58) Kissling, G. P.; Fermín, D. J. Electrochemical Hole Injection into the Valence Band of Thiol Stabilised CdTe Quantum Dots. *Phys. Chem. Chem. Phys.* **2009**, *11*, 10080–10086.
(59) Yanai, T.; Tew, D. P.; Handy, N. C. A New Hybrid Exchange–correlation Functional Using the Coulomb-Attenuating Method (CAM-B3LYP). *Chem. Phys. Lett.* **2008**, *393* (2004), 51–57.
(60) Brawand, N. P.; Vörös, M.; Govoni, M.; Galli, G. Generalization of Dielectric-Dependent Hybrid Functionals to Finite Systems. *Phys. Rev. X* **2016**, *6* (4), 41002.

(61) Marques, M. A. L.; Vidal, J.; Oliveira, M. J. T.; Reining, L.; Botti, S. Density-Based Mixing Parameter for Hybrid Functionals. *Phys. Rev. B* **2011**, *83* (3), 35119.
(62) Conesa, J. C. Band Structures and Nitrogen Doping Effects in Zinc Titanate Photocatalysts. *Catal. Today* **2013**, *208*, 11–18.
(63) Verma, P.; Truhlar, D. G. HLE17: An Improved Local Exchange-Correlation Functional for Computing Semiconductor Band Gaps and Molecular Excitation Energies. *J. Phys. Chem. C* **2017**, *121* (13), 7144–7154.
(64) Skone, J. H.; Govoni, M.; Galli, G. Nonempirical Range-Separated Hybrid Functionals for Solids and Molecules. *Phys. Rev. B* **2016**, *93* (23), 1–12.
(65) Le Bahers, T.; Haller, S.; Le Mercier, T.; Barboux, P. Assessing the Use of BiCuOS for Photovoltaic Application: From DFT to Macroscopic Simulation. *J. Phys. Chem. C* **2015**, *119* (31), 17585–17595.
(66) Kusainova, A. M.; Berdonosov, P. S.; Akselrud, L. G.; Kholodkovskaya, L. N.; Dolgikh, V. A.; Popovkin, B. A. New Layered Compounds Wit the General Composition (MO)(CuSe), Where M=Bi, Nd, Gd, Dy and BiCuOS: Syntheses and Crystal Structure. *J. Solid State Chem.* **1994**, *112*, 189–191.
(67) Sheets, W. C.; Stampler, E. S.; Kabbour, H.; Bertoni, M. I.; Cario, L.; Mason, T. O.; Marks, T. J.; Poeppelmeier, K. R. Facile Synthesis of BiCuOS by Hydrothermal Methods. *Inorg. Chem.* **2007**, *46* (25), 10741–10748.
(68) Richard, A. P.; Russell, J.; Zakutayev, A.; Zakharov, L. N.; Keszler, D. A.; Tate, J. Synthesis, Structure, and Optical Properties of BiCuOCh (Ch=S, Se, and Te). *J. Solid State Chem.* **2012**, *187*, 15–19.
(69) Tate, J.; Newhouse, P. F.; Kykyneshi, R.; Hersh, P. A.; Kinney, J.; McIntyre, D. H.; Keszler, D. A. Chalcogen-Based Transparent Conductors. *Thin Solid Films* **2008**, *516* (17), 5795–5799.
(70) Zou, D.; Xie, S.; Liu, Y.; Lin, J.; Li, J. Electronic Structures and Thermoelectric Properties of Layered BiCuOCh Oxychalcogenides (Ch = S, Se and Te): First-Principles Calculations. *J. Mater. Chem.* **2013**, *1* (31), 8888--8896.
(71) Berthebaud, D.; Guilmeau, E.; Lebedev, O. I.; Maignan, A.; Gamon, J.; Barboux, P. The $BiCu_{1-x}OS$ Oxysulfide: Copper Deficiency and Electronic Properties. *J. Solid State Chem.* **2016**, *237*, 292–299.
(72) Labégorre, J.-B.; Al Rahal Al Orabi, R.; Virfeu, A.; Gamon, J.; Barboux, P.; Pautrot-d'Alençon, L.; Le Mercier, T.; Berthebaud, D.; Maignan, A.; Guilmeau, E. Electronic Band Structure Engineering and Enhanced Thermoelectric Transport Properties in Pb-Doped BiCuOS Oxysulfide. *Chem. Mater.* **2018**, acs.chemmater.7b04989.
(73) Karna, S. K.; Wang, C.-W.; Wu, C.-M.; Hsu, C.-K.; Hsu, D.; Wang, C.-J.; Li, W.-H.; Sankar, R.; Chou, F.-C. Spin, Charge and Lattice Couplings in Cu-Deficient Oxysulphide $BiCu_{0.94}OS$. *J. Phys. Condens. Matter* **2012**, *24*, 266004.
(74) Verschraegen, J.; Burgelman, M. Numerical Modeling of Intra-Band Tunneling for Heterojunction Solar Cells in Scaps. *Thin Solid Films* **2007**, *515* (15), 6276–6279.
(75) Ueda, K.; Takafuji, K.; Hiramatsu, H.; Ohta, H.; Kamiya, T.; Hirano, M. Electrical and Optical Properties and Electronic Structures of LnCuOS (Ln=La, Nd). *Chem. Mater.* **2003**, *15*, 3692–3695.
(76) Chan, G. H.; Deng, B.; Bertoni, M.; Ireland, J. R.; Hersam, M. C.; Mason, T. O.; Duyne, R. P. Van; Ibers, J. A. Syntheses , Structures , Physical Properties , and Theoretical Studies of CeM_xOS (M=Cu, Ag, x=0.8) and CeAgOS. *Inorg. Chem.* **2006**, *45* (20), 8–15.
(77) Wang, H.; Li, S.; Liu, Y.; Ding, J.; Lin, Y.-H.; Xu, H.; Xu, B.; Nan, C.-W. $Bi_{1-x}La_xCuSeO$ as New Tunable Full Solar Light Active Photocatalysts. *Sci. Rep.* **2016**, *6* (April), 24620.
(78) Liu, Y.; Ding, J.; Xu, B.; Lan, J.; Zheng, Y.; Zhan, B.; Zhang, B.; Lin, Y. Enhanced Thermoelectric Performance of La-Doped BiCuSeO by Tuning Band Structure Enhanced Thermoelectric Performance of La-Doped BiCuSeO by Tuning Band Structure. *Appl. Phys. Lett.* **2015**, *106*, 233903.
(79) Lebedev, O. I.; Rahal, R. Al; Orabi, A.; Caen, F.-. Substituting Copper with Silver in the BiMOCh Layered Compounds (M = Cu or Ag; Ch = S, Se, or Te): Crystal, Electronic Structure, and Optoelectronic Properties. *Chem. Mater.* **2017**.
(80) Thomas, A.; Fischer, A.; Goettmann, F.; Antonietti, M.; Müller, J.-O.; Schlögl, R.; Carlsson, J. M. Graphitic Carbon Nitride Materials: Variation of Structure and Morphology and Their Use as Metal-Free Catalysts. *J. Mater. Chem.* **2008**, *18* (41), 4893.
(81) Zhu, J.; Xiao, P.; Li, H.; Carabineiro, S. A. C. Graphitic Carbon Nitride: Synthesis, Properties, and Applications in Catalysis. *ACS Appl. Mater. Inter.* **2014**, *6* (19), 16449–16465.
(82) Gong, Y.; Li, M.; Li, H.; Wang, Y. Graphitic Carbon Nitride Polymers: Promising Catalysts or Catalyst Supports for Heterogeneous Oxidation and Hydrogenation. *Green Chem.* **2015**, *17* (2), 715–736.
(83) Zhang, L.; Ou, M.; Yao, H.; Li, Z.; Qu, D.; Liu, F.; Wang, J.; Wang, J.; Li, Z. Enhanced Supercapacitive Performance of Graphite-like C3N4assembled with NiAl-Layered Double Hydroxide. *Electrochim. Acta* **2015**, *186*, 292–301.
(84) Chen, Q.; Zhao, Y.; Huang, X.; Chen, N.; Qu, L. Three-Dimensional Graphitic Carbon Nitride Functionalized Graphene-Based High-Performance Supercapacitors. *J. Mater. Chem. A* **2015**, *3* (13), 6761–6766.
(85) Chen, Y.; Tan, C.; Zhang, H.; Wang, L. Two-Dimensional Graphene Analogues for Biomedical Applications. *Chem. Soc. Rev.* **2015**, *44* (9), 2681–2701.
(86) Zheng, Y.; Liu, J.; Liang, J.; Jaroniec, M.; Qiao, S. Z. Graphitic Carbon Nitride Materials: Controllable Synthesis and Applications in Fuel Cells and Photocatalysis. *Energy Environ. Sci.* **2012**, *5* (5), 6717.
(87) Zhang, J.; Sun, J.; Maeda, K.; Domen, K.; Liu, P.; Antonietti, M.; Fu, X.; Wang, X. Sulfur-Mediated Synthesis of Carbon Nitride: Band-Gap Engineering and Improved Functions for Photocatalysis. *Energy Environ. Sci.* **2011**, *4* (3), 675–678.
(88) Wang, X.; Maeda, K.; Thomas, A.; Takanabe, K.; Xin, G.; Carlsson, J. M.; Domen, K.; Antonietti, M. A Metal-Free Polymeric Photocatalyst for Hydrogen Production from Water under Visible Light. *Nat. Mat.* **2009**, *8* (1), 76–80.
(89) Grimme, S. Accurate Description of van Der Waals Complexes by Density Functional Theory Including Empirical Corrections. *J. Comput. Chem.* **2004**, *25* (12), 1463–1473.
(90) Melissen, S.; Steinmann, S. N.; Le Bahers, T.; Sautet, P. DFT Perspective on the Thermochemistry of Carbon

Nitride Synthesis. *J. Phys. Chem. C* **2016**, *120*, 24542–24550.
(91) Clarke, T. M.; Durrant, J. R. Charge Photogeneration in Organic Solar Cells. *Chem. Rev.* **2010**, *110*, 6736–6767.
(92) Ziani, A.; Le Paven, C.; Le Gendre, L.; Marlec, F.; Benzerga, R.; Tessier, F.; Cheviré, F.; Hedhili, M. N.; Garcia-Esparza, A. T.; Melissen, S.; et al. Photophysical Properties of $SrTaO_2N$ Thin Films and Influence of Anion Ordering: A Joint Theoretical and Experimental Investigation. *Chem. Mater.* **2017**, *29* (9), 3989–3998.
(93) Petit, S.; Melissen, S. T. A. G.; Duclaux, L.; Sougrati, M. T.; Le Bahers, T.; Sautet, P.; Dambournet, D.; Borkiewicz, O. J.; Laberty-Robert, C.; Durupthy, O. How Should Iron and Titanium Be Combined in Oxides to Improve Photoelectrochemical Properties? *J. Phys. Chem. C* **2016**, acs.jpcc.6b05794.
(94) Melissen, S. T. A. G.; Labat, F.; Sautet, P.; Le Bahers, T. Electronic Properties of $PbX_3CH_3NH_3$ (X = Cl, Br, I) Compounds for Photovoltaic and Photocatalytic Applications. *Phys. Chem. Chem. Phys.* **2015**, *17*, 2199–2209.
(95) McCrory, C. C. L.; Jung, S. H.; Peters, J. C.; Jaramillo, T. F. Benchmarking Heterogeneous Electrocatalysts for the Oxygen Evolution Reaction. *J. Am. Chem. Soc.* **2013**, *135* (45), 16977–16987.
(96) Nurlaela, E.; Wang, H.; Shinagawa, T.; Flanagan, S.; Ould-Chikh, S.; Qureshi, M.; Mics, Z.; Sautet, P.; Le Bahers, T.; Cánovas, E.; et al. Enhanced Kinetics of Hole Transfer and Electrocatalysis during Photocatalytic Oxygen Evolution by Cocatalyst Tuning. *ACS Catal.* **2016**, *6* (7), 4117–4126.
(97) Townsend, T. K.; Browning, N. D.; Osterloh, F. E. Overall Photocatalytic Water Splitting with NiO_x–$SrTiO_3$ – a Revised Mechanism. *Energ. Environ. Sci.* **2012**, *5* (11), 9543.
(98) Bajdich, M.; García-Mota, M.; Vojvodic, A.; Nørskov, J. K.; Bell, A. T. Theoretical Investigation of the Activity of Cobalt Oxides for the Electrochemical Oxidation of Water. *J. Am. Chem. Soc.* **2013**, *135* (36), 13521–13530.
(99) Chen, J.; Wu, X.; Selloni, A. Electronic Structure and Bonding Properties of Cobalt Oxide in the Spinel Structure. *Phys. Rev. B* **2011**, *83* (24), 245204.
(100) García-Mota, M.; Bajdich, M.; Viswanathan, V.; Vojvodic, A.; Bell, A. T.; Nørskov, J. K. Importance of Correlation in Determining Electrocatalytic Oxygen Evolution Activity on Cobalt Oxides. *J. Phys. Chem. C* **2012**, *116* (39), 21077–21082.
(101) Friebel, D.; Louie, M. W.; Bajdich, M.; Sanwald, K. E.; Cai, Y.; Wise, A. M.; Cheng, M. J.; Sokaras, D.; Weng, T. C.; Alonso-Mori, R.; et al. Identification of Highly Active Fe Sites in (Ni,Fe)OOH for Electrocatalytic Water Splitting. *J. Am. Chem. Soc.* **2015**, *137* (3), 1305–1313.
(102) Neufeld, O.; Yatom, N.; Caspary Toroker, M. A First-Principles Study on the Role of an Al_2O_3 Overlayer on Fe_2O_3 for Water Splitting. *ACS Catal.* **2015**, *5* (12), 7237–7243.
(103) Tsien, R. Y. Constructing and Exploiting the Fluorescent Protein Paintbox (Nobel Lecture). *Integr. Biol.* **2010**, *2*, 77–93.
(104) Levene, M. J.; Dombeck, D. A.; Kasischke, K. A.; Molloy, R. P.; Webb, W. W. In Vivo Multiphoton Microscopy of Deep Brain Tissue. *J. Neurophysiol* **2009**, *91* (December 2003), 1908–1912.
(105) Chapman, S.; Oparka, K. J.; Roberts, A. G. New Tools for in Vivo Fluorescence Tagging. *Curr. Opin. Plant Biol.* **2005**, *8* (6), 565–573.
(106) Leblond, F.; Davis, S. C.; Valdés, P. A.; Pogue, B. W. Pre-Clinical Whole-Body Fluorescence Imaging: Review of Instruments, Methods and Applications. *J. Photochem. Photobiol. B* **2010**, *98* (1), 77–94.
(107) Denk, W.; Strickler, J. H.; Webb, W. W. Two-Photon Laser Scanning Fluorescence Microscopy. *Science.* **1990**, *248* (4951), 73–76.
(108) Helmchen, F.; Denk, W. Deep Tissue Two-Photon Microscopy. *Nat. Methods* **2005**, *2* (12), 932–940.
(109) Kunz, H.; Müllen, K. Natural Product and Material Chemistries - Separated Forever? *J. Am. Chem. Soc.* **2013**, *135* (24), 8764–8769.
(110) Hilderbrand, S. A.; Weissleder, R. Near-Infrared Fluorescence: Application to in Vivo Molecular Imaging. *Curr. Opin. Chem. Biol.* **2010**, *14* (1), 71–79.
(111) Aidas, K.; Angeli, C.; Bak, K. L.; Bakken, V.; Bast, R.; Boman, L.; Christiansen, O.; Cimiraglia, R.; Coriani, S.; Dahle, P.; et al. The Dalton Quantum Chemistry Program System. *WIREs Comput. Mol. Sci.* **2014**, *4* (3), 269–284.
(112) Santoro, F.; Improta, R.; Lami, A.; Bloino, J.; Barone, V. Effective Method to Compute Franck-Condon Integrals for Optical Spectra of Large Molecules in Solution. *J. Chem. Phys.* **2007**, *126*, 84509.
(113) Hay, P. J.; Wadt, W. R. Ab Initio Effective Core Potentials for Molecular Calculations. Potentials for the Transition Metal Atoms Sc to Hg. *J. Chem. Phys.* **1985**, *82* (1), 270.
(114) Brymora, K.; Ducasse, L.; Delaure, A.; Hirsch, L.; Jarrosson, T.; Niebel, C.; Serein-Spirau, F.; Peresutti, R.; Dautel, O.; Castet, F. Computational Design of Quadrupolar Donor-Acceptor-Donor Molecules with near-Infrared Light-Harvesting Capabilities. *Dye. Pigment.* **2018**, *149* (October 2017), 882–892.
(115) Jacquemin, D. Excited-State Dipole and Quadrupole Moments: TD-DFT versus CC2. *J. Chem. Theory Comput.* **2016**, *12* (8), 3993–4003.
(116) Le Bahers, T.; Brémond, E.; Ciofini, I.; Adamo, C. The Nature of Vertical Excited States of Dyes Containing Metals for DSSC Applications: Insights from TD-DFT and Density Based Indexes. *Phys. Chem. Chem. Phys.* **2014**, *16*, 14435–14444.
(117) Pawlicki, M.; Collins, H. A.; Denning, R. G.; Anderson, H. L. Two-Photon Absorption and the Design of Two-Photon Dyes. *Angew. Chem. Int. Ed.* **2009**, *48* (18), 3244–3266.
(118) Botchway, S. W.; Charnley, M.; Haycock, J. W.; Parker, A. W.; Rochester, D. L.; Weinstein, J. A.; Williams, J. A. G. Time-Resolved and Two-Photon Emission Imaging Microscopy of Live Cells with Inert Platinum Complexes. *Proc. Natl. Acad. Sci. USA PNAS* **2008**, *105* (42), 16071–16076.
(119) Liu, J.; Liu, Y.; Liu, Q.; Li, C.; Sun, L.; Li, F. Iridium(III) Complex-Coated Nanosystem for Ratiometric Upconversion Luminescence Bioimaging of Cyanide Anions. *J. Am. Chem. Soc.* **2011**, *133* (39), 15276–15279.
(120) Fernández-Moreira, V.; Thorp-Greenwood, F. L.; Coogan, M. P. Application of d6 Transition Metal Complexes in Fluorescence Cell Imaging. *Chem. Commun.* **2010**, *46* (2), 186–202.

(121) Foote, C. S. Photosensitized Oxygenations and the Role of Singlet Oxygen. *Acc. Chem. Res.* **1968**, *1* (4), 104–110.
(122) Dumont, E.; Grüber, R.; Bignon, E.; Morell, C.; Moreau, Y.; Monari, A.; Ravanat, J. L. Probing the Reactivity of Singlet Oxygen with Purines. *Nucleic Acid Res.* **2016**, *44* (1), 56–62.
(123) Bhawalkar, J. D.; Kumar, N. D.; Zhao, C.-F.; Prasad, P. N. Two-Photon Photodynamic Therapy. *J. Clin. Laser Med. Sur.* **2009**, *15*, 201–204.
(124) Lanoë, P.-H.; Gallavardin, T.; Dupin, A.; Maury, O.; Baldeck, P. L.; Lindgren, M.; Monnereau, C.; Andraud, C. Influence of Bromine Substitution Pattern on the Singlet Oxygen Generation Efficiency of Two-Photon Absorbing Chromophores. *Org. Biol. Chem.* **2012**, *10* (31), 6275.
(125) Marian, C. M. Spin-Orbit Coupling and Intersystem Crossing in Molecules. *WIREs Comput. Mol. Sci.* **2012**, *2* (2), 187–203.
(126) Gao, X.; Bai, S.; Fazzi, D.; Niehaus, T.; Barbatti, M.; Thiel, W. Evaluation of Spin-Orbit Couplings with Linear-Response Time-Dependent Density Functional Methods. *J. Chem. Theory Comput.* **2017**, *13*, 515–524.
(127) McClure, D. S. Selection Rules for Singlet-Triplet Perturbations in Polyatomic Molecules. *J. Chem. Phys.* **1949**, *17* (7), 665–666.
(128) Zheng, H.; Ou, J. Z.; Strano, M. S.; Kaner, R. B.; Mitchell, A.; Kalantar-Zadeh, K. Nanostructured Tungsten Oxide - Properties, Synthesis, and Applications. *Adv. Funct. Mater.* **2011**, *21* (12), 2175–2196.
(129) He, T.; Yao, J. Photochromism of Molybdenum Oxide. *J. Photochem. Photobiol. C* **2003**, *4* (2), 125–143.
(130) Songara, S.; Patra, M. K.; Manoth, M.; Saini, L.; Gupta, V.; Gowd, G. S.; Vadera, S. R.; Kumar, N. Synthesis and Studies on Photochromic Properties of Vanadium Doped TiO_2 Nanoparticles. *J. Photochem. Photobiol. A* **2010**, *209*, 68–73.
(131) Armstrong, J. a; Weller, M. T. Structural Observation of Photochromism. *Chem. Comm.* **2006**, *4*, 1094–1096.
(132) Milisenda, C. C.; Koch, S.; Müller, S.; Stephan, T.; Wild, M. Gemstones with Photochromism. *Proceedings, IGC 2015, Vilnius* **2009**, 107–109.
(133) Curutchet, A.; Le Bahers, T. Modeling the Photochromism of S-Doped Sodalites Using DFT, TD-DFT, and SAC-CI Methods. *Inorg. Chem.* **2017**, *56* (1), 414–423.
(134) Fukuda, R.; Ehara, M. Efficiency of Perturbation-Selection and Its Orbital Dependence in the SAC-CI Calculations for Valence Excitations of Medium-Size Molecules. *J. Comput. Chem.* **2014**, *35*, 2163–2176.
(135) Ehara, M.; Ishida, M.; Toyota, K.; NakatsujiH. SAC-CI General-R Method: Theory and Applications to the Modern Multi-Electron Processes. In *Rev. Quantum Chem.*; Sen, K. D., Ed.; World Wide Scientific Co. Pte. Ltd., 2002; p 293.
(136) Williams, E. R.; Simmonds, A.; Armstrong, J. A.; Weller, M. T. Compositional and Structural Control of Tenebrescence. *J. Mater. Chem.* **2010**, *20*, 10883–10887.
(137) Maeda, K.; Sakamoto, N.; Ikeda, T.; Ohtsuka, H.; Xiong, A.; Lu, D.; Kanehara, M.; Teranishi, T.; Domen, K. Preparation of Core-Shell-Structured Nanoparticles (with a Noble-Metal or Metal Oxide Core and a Chromia Shell) and Their Application in Water Splitting by Means of Visible Light. *Chem.-Eur. J.* **2010**, *16* (26), 7750–7759.
(138) Garcia-Esparza, A. T.; Takanabe, K. A Simplified Theoretical Guideline for Overall Water Splitting Using Photocatalyst Particles. *J. Mater. Chem. A* **2016**, *4* (8), 2894–2908.
(139) Zhang, Y.; Zhang, N.; Tang, Z.-R.; Xu, Y.-J. Identification of Bi2WO6 as a Highly Selective Visible-Light Photocatalyst toward Oxidation of Glycerol to Dihydroxyacetone in Water. *Chem. Sci.* **2013**, *4* (4), 1820–1824.
(140) Simões, M.; Baranton, S.; Coutanceau, C. Electro-Oxidation of Glycerol at Pd Based Nano-Catalysts for an Application in Alkaline Fuel Cells for Chemicals and Energy Cogeneration. *Appl. Catal. B-Environ* **2010**, *93* (3–4), 354–362.
(141) Simões, M.; Baranton, S.; Coutanceau, C. Electrochemical Valorisation of Glycerol. *ChemSusChem* **2012**, *5* (11), 2106–2124.
(142) Verlato, E.; Cattarin, S.; Comisso, N.; Gambirasi, A.; Musiani, M.; Vázquez-Gómez, L. Preparation of Pd-Modified Ni Foam Electrodes and Their Use as Anodes for the Oxidation of Alcohols in Basic Media. *Electrocatal.* **2012**, *3* (1), 48–58.
(143) Borwein, D.; Borwein, J. M.; Taylor, K. F. Convergence of Lattice Sums and Madelung's Constant. *J. Math. Phys.* **1985**, *26* (11), 2999–3009.
(144) Derenzo, S. E.; Klintenberg, M. K.; Weber, M. J. Determining Point Charge Arrays That Produce Accurate Ionic Crystal Fields for Atomic Cluster Calculations. *J. Chem. Phys.* **2000**, *112* (5), 2074–2081.
(145) Klintenberg, M.; Derenzo, S. E.; Weber, M. J. Accurate Crystal Fields for Embedded Cluster Calculations. *Comput. Phys. Commun.* **2000**, *131* (1), 120–128.